

Large Scale Fire Dynamics in Spacecraft in Reduced Gravity

Final Report

Start Date: 10/01/2003, End Date: 09/30/2007

Grant/Contract Number: NNC04IA17I

PI: Gregory Linteris

Fire Research Division
Building and Fire Research Laboratory
National Institute of Standards and Technology

1. Abstract

Numerical fire codes are being widely used for understanding normal gravity ($1 g_n$) fires. The goal of the present project was to modify one such code, the National Institute of Standards and Technology (NIST) Fire Dynamics Simulator (FDS), so that it can be used to accurately describe fires in the variable-gravity environments of space vehicles and habitats. We have used the code to understand limitations to oxygen transport for large fires in a typical module on the International Space Station, and to investigate the characteristics of the combustion products likely released during the Mir oxygen generator fire. We have shown that while zero-gravity environments ($0 g_n$) environments can produce severe oxygen transport limitations for large fires, the levels of gravity typical of moon or Mars bases create buoyant mixing environments which allow oxygen transport much closer to conditions at $1 g_n$. We have contributed to flammability maps for $0 g_n$ flames through experiments and modeling of co-flow diffusion flame extinction in $1 g_n$ and $0 g_n$.

In the course of the project it became clear that the ability of any fire model to describe fire growth depends upon its ability to describe the fuel generation rate from burning material. Unfortunately, the validation of the numerical fire codes for such applications was severely limited, and early work indicated that improvements were necessary. Hence, we sought to investigate and validate the performance of the code for predicting materials mass loss, and understand which material parameters have the largest influence on the predicted burning rate, so that efforts in the future could focus on those parameters.

Finally, in order to ultimately validate numerical burning rate predictions for flame experiments at $0 g_n$, a method was devised to correlate the measured heat release rate with the flame area (which can be readily obtained in space-based experiments, unlike the load-cell based mass loss measurements which are not possible in $0 g_n$).

2. Scientific context, hypothesis, research objectives

With longer-duration human exploration missions to Mars, the moon, or on the International Space Station, the chances for an accidental fire increase. Despite much excellent and useful research to understand the behavior of laboratory flames in microgravity, virtually no work has been conducted to understand large fires in microgravity (μg). This undoubtedly results from the danger and difficulty of conducting such experiments. The goal here is to use detailed numerical modeling to understand large fires in the reduced gravity conditions ($0 g_n$, $1/6 g_n$, and $1/3 g_n$) of a range of extraterrestrial missions. Recently, computational fluid dynamics (CFD) numerical simulation codes based on Large Eddy Simulation (LES) have emerged as excellent tools for understanding large fires in $1 g_n$. One such program, the NIST Fire Dynamics Simulator (FDS), has increased in use world-wide by researchers, fire protection engineers, and others. The range of applications and the sophistication of its underlying engineering models are increasing at a rapid pace. Hence, it seemed like an excellent time to start to adapt the code for understanding large fires in reduced gravity, and use this valuable tool to provide the first insights into the fundamental behavior of such fires. This project brings together researchers in developing $1 g_n$ fire models with those in microgravity combustion research to examine and modify the sub-grid scale models in FDS for apply it to understanding large fires in reduced gravity. The modified code will then be used to determine the important parameters in spacecraft large-fire growth and spread, suppression, and detection, and can also be used for fire-fighting training and fire recreation.

3. Accomplishments as outlined in original proposal

3.1. Oxygen Limitations to Fire Growth in Reduced Gravity Environments

This work investigated two aspects of the problem of predicting fires in variable gravity: 1.) validation of the sub-grid models of turbulence in FDS for conditions similar to those expected to be encountered in spacecraft; and 2.) exploration of the global effects of gravity and ventilation on the potential heat release from a fire. The results are outlined in ref. [1].

The goal of the first part of the work was to validate the capability of FDS to predict the movement of the turbulent air streams in micro- and variable-gravity environments. Unfortunately, experimental data on ventilation flows in variable gravity are not yet available. Nonetheless, there are $1 g_n$ experimental data in the heating and ventilation literature for isothermal, low speed air flow in simple geometries; these are relatively close to the conditions expected for low-gravity vehicles and habitation modules. Using an available dataset on ventilation in a rectangular room (3m x 3 m x 9 m) with variable inlet and exit locations and air flows, FDS was used to predict the velocities for comparison with the data. For a range of vertical and axial locations in the room, with air flows of -0.2 m/s to 0.4 m/s, FDS predictions of the average gas velocities were in

reasonable agreement with the measurements. The significance of the agreement goes beyond gas velocities since the turbulent motion which affects the development of the velocity profile is the same physical phenomena which affects mixing, which is crucial for fire growth and spread.

The goal of the second part of this work was to understand how the supply of fresh, unburned air to the fire location is affected by variable gravity and ventilation flow in a module. The calculations examined one question: Under what conditions will a large fire in low gravity be non-viable due to limitations on the transport of oxygen to the flame? The calculations indicate that for uniform, co-flowing, laminar inlet flow, and fuel sources of representative size ($r = 5$ cm to $r = 15$ cm) the heat release rate can be limited by the supply of air. For higher air flow and smaller flames, the flames reach near-peak values after about 20 s, whereas for larger flames with lower airflow, the heat release can be oxygen limited. Nonetheless, with any level of gravity above $1/6 g$, there is sufficient buoyancy driven flow to make the heat release rate comparable to $1 g_n$ results. A most important conclusion, however, is that putting the same burner into a $0 g_n$ module with representative turbulent flow provides sufficient air so that the flames behave much more like flames in $1 g_n$ than laminar co-flow flames in $0 g_n$.

3.2. Overall Large Fire Behavior in Space Habitation Modules: Mir Fire Analysis

Work in this area focused on predicting the Mir fire and understanding any fire risk from it, and starting to understand how fires in an ISS module (as a representative case) might differ from a normal gravity room fire. First we used ground-based tests of a similar oxygen generator to estimate that the heat output for the Mir fire was about 5 kW, in a volume of about 0.2 m^3 . We tried valiantly to get the numerical code to simulate a 5 kW fire burning in $0 g_n$, but various limitations in version 4.0 of FDS did not allow us to achieve that (and still have the radiation transport part of the calculation working). Hence, we must wait for FDS version 5.0 to be released to continue the investigations. In lieu of simulating a fire itself, we performed equilibrium calculations to estimate the product gas temperatures downstream of the oxygen generator to start to get a sense of the fire threat from the burning stainless steel of the oxygen generator. The final product temperature for stoichiometric combustion of iron with oxygen is about 3032 K; however, the ventilation fan on the oxygen generator diluted these products with 1333 K/min of cabin air. Hence, the final effluent temperature from the burning oxygen generating system is estimated to be around 500 K. We then attempted to simulate the radiation from the Fe_2O_3 particles, but this was beyond the current capabilities of FDS 4.0. Our conclusion at this point was that if the mixing fan were operating, the fire threat from the hot product gases would be low; however, if hot glowing particles were present, they could be an ignition source.

A major finding of the early part of the work was that while FDS 4 represented the state-of-the-art in fire modeling, for many of the desired simulations for the large $0 g_n$ fires,

many of the phenomena occurring could not be modeled due to numerical instabilities, and other problems.

3.3 Extinction in co-flow diffusion flames.

Gas-phase reaction in FDS is treated either with a mixture fraction model (infinite rate chemistry) or a two-step finite rate description. With the mixture fraction model, there exists a simple flammability map based on oxygen volume fraction and the initial mixture temperature. The basis for this is an approximately constant adiabatic flame temperature (around 1600 K) at extinction. In reduced gravity, however, the flammability map will likely need to be revised. We have been collaborating with F. Takahashi at NASA-GRC in work to understand stabilization and extinguishment of co-flow diffusion flames (formed over cup-burners) in normal and reduced gravity. The hope is that some unified extinction criterion in zero (and reduced) gravity can be deduced from which a sub-grid criterion can be inserted into FDS. This work is outlined in ref. [2 – 5].

So far, we have made good progress in the numerical modeling of the influence of inert and chemical inhibitors, flame oscillations, and fuel type on flame extinguishment, and how these change with gravity levels. In particular, we have shown that:

1. Absolute extinction temperatures (temperature below which exothermic reactions cease) in 0 g_n are lower, 1300 K vs 1700 K in 1 g_n [2].
2. A constant adiabatic flame temperature at extinction (a model typically used in 1 g_n) may not be appropriate in reduced gravity since the flames are not adiabatic. For example, radiation from the flame zone reduces the temperature compared to the adiabatic flame temperature, leading to tip extinguishment. The effect is more important in 0 g_n not because of higher radiation, but because of lower heat release rates due to the lower oxygen transport to the flame, making radiation comparatively more important[3].
3. Back-diffusion of radicals from the downstream diffusion flame supports stabilization region. This makes flames in 0 g_n more susceptible to extinction from heat losses from the downstream region than comparable flames in 1 g_n [4].
4. Buoyancy-induced flame flicker disrupts the flame base, promoting flame blow-off in 1 g_n ; whereas in reduced gravity, flicker does not exist, which allows flame to persist to higher inhibitor volume fractions (i.e., to lower oxygen concentrations) [5].

Ultimately, all of these effects may need to be incorporated into flame extinction algorithms in reduced gravity, in future work.

4. New Research Directions

In supplementing FDS for describing large fires in variable gravity, we had intended to move directly to examining the various sub-grid models which were most likely to need modifications. In the process, however, we first started to validate the model's predictive capability for cone samples in 1 g_n . As a result of those simulations and experiments we found that much more work was necessary to predict burning rates—even in the cone calorimeter. For example, more work was found to be necessary to properly determine the relevant input parameters for the description of mass loss from solid samples. The progress of that new direction is outlined in section 4.1 below.

Beyond the validation experiments and calculations described above for 1 g_n , however, it would ultimately be required to validate the mass loss (and heat release) predictions from experiments in 0 g_n . In order to examine a possible method to do this, we studied the use of the flame size as a surrogate for heat release rate. Such a technique would also be useful to microgravity combustion experiments on ISS, in which the heat release rate is desired, but the experimental apparatus is already built, and does not include measurements of those parameters. Hence, we devoted some effort in the present project to helping identify the utility of a method which uses flame size as a surrogate for heat release, as described in section 4.2 below.

4.1. Tests of FDS for burning of condensed-phase materials in 1 g_n

The above work on oxygen limitations to fire growth in low gravity used a fire of prescribed fuel addition rate. A real fire, however, typically depends upon the feedback of the heat from the fire to decompose the solid fuel into gaseous compounds which then burn in the flame. Hence, to predict fire growth and spread (in 1 g_n or low- g_n), FDS must be able to properly account for the decomposition and burning of solid-phase materials.

FDS was originally developed to describe the movement of smoke and hot gases produced from a fire of specified size. Recently, it has been extended to the much more difficult task of predicting the growth and spread of fires in buildings. In building fires, the difficulty is also worse in that many of the “fuels” are both poorly specified and oriented in unknown configurations. Since the grid resolution in a numerical simulation for something the size of a building will be inherently coarse due to limitations on computational resources, simplifications are necessary to describe the phenomena which occur at sub-grid scale resolution. The situation in a typical ISS module will be somewhat more tractable in that the materials present will be better known, and the size is smaller. Hence, experimental data for samples of the scale of the cone calorimeter seemed appropriate. They are a much more realistic scale than the very small flames necessary for the fundamental microgravity combustion experiments of past ground and flight investigations, and experimental data are available (or can be obtained). The ability for FDS to predict the burning rate of cone samples (in 0 g or 1 g_n) is a necessary prerequisite for its ability to describe low-gravity fires generally.

Hence, as a first step, 1 g_n burning rate data were generated for intermediate-scale samples using the NIST cone calorimeter (a device for irradiating a 10 cm x 10 cm x 2.5 cm polymer sample and measuring the heat release and mass loss rates) and FDS was used to predict the burning rate. This approach provides some measure of the model's capacity for predicting fire growth, since an ability to predict the burning of such a simple configuration is a clear prerequisite for modeling large fires (which ultimately will also involve burning on the scale of cone samples and larger). The first goal of this work was to assess the relative importance of various numerical, physical, and experimental parameters on the predicted burning of the sample, so that later accurate simulations could be made for model validation. This work is described in ref. [6]. In that work, the low-strain inverted cone experiments of Olson were also simulated with FDS, as a first step in predicting material burning in 0 g_n.

As expected, it was found that to accurately predict the heat release rate of the burning polymer, it was important to properly specify the domain size and select a fine enough grid resolution; those parameters were quantified. The material properties: heat of vaporization, ignition temperature, and the activation energy for decomposition all needed to be carefully specified, and some experimental configuration factors (e.g., lip on sample holder and presence of the cone heater) also needed to be accurately described. To get correct values for cases with low imposed radiant heat flux, the flame heat transfer to the sample needed careful attention. Of minor importance were the use of direct numerical simulation rather than large-eddy simulation, and use of 3-D instead of 2-D coordinates in the calculation method. Presence of either exhaust flow or backside insulation had little effect on the calculations. A major finding was that the empirically determined effective heat of gasification was the most important parameter necessary for accurate prediction of the burning rate, and that values of the heat of gasification extracted from the cone measurements did not yield a predicted heat release rate in agreement with those measured in the cone. Another major finding was that when the heat flux to the material occurs locally from the attached flame, the local geometry of the material has a large effect on the mass loss rate; unlike conditions for which the heat flux occurs from thermal radiation further from the material.

At the start of the present project, FDS version 4 was the most recent version. In it, the treatment of solid-phase burning is relatively straightforward, especially for polymers. Heat input to the sample occurs in one-dimension by conduction and radiation. There is an energy balance at the surface in which heat input minus losses (due to conduction into the sample, re-radiation and convective losses) goes to sample phase change. The energy required for phase change is characterized by an effective heat of gasification, which essentially acts as a heat of vaporization (charring surfaces are treated differently). Other necessary parameters, such as the polymer's conductivity, specific heat, density, stoichiometry and combustion of the monomer and its heat of combustion are more straightforward to determine. The complicated process of thermal degradation, vaporization, and internal transport of the evolved (single) gas-phase fuel species is essentially described by this single parameter. Such an approach can work acceptably well for a room fire, where many materials typically burn at once, and an average value for each can be sufficient. To model microgravity flames over cone-sized samples then

first requires accurate determination of the effective heat of vaporization L_g . It was found that there were significant limitations in the version of FDS; however, the next version, FDS5 had significant improvements. Consequently, FDS5 was used for subsequent simulations, as described in ref. [7].

In ref. [7], both FDS 5 and a recently-developed code from FAA (ThermaKin) were used to assess the influence of various material properties on the burning rate of a polymer. The two numerical codes were generally in very good agreement for their predictions of the MLR versus time curves, except when in-depth absorption of radiation was important. The influence of various material properties (thickness, thermal conductivity, specific heat, absorption of infrared radiation, heat of reaction) on mass loss history was assessed, via their effect on the ignition time, average mass loss rate, peak mass loss rate, and time to peak. The two codes predict the influence of material parameters on the MLR in the order of decreasing importance: heat of reaction, thickness, specific heat, absorption coefficient, thermal conductivity, and activation energy of the polymer decomposition. Changes in the material properties also influence the MLR curves by switching the sample from thermally thick to thermally thin.

The end result of this (and other) work with FDS5 in predicting cone calorimeter mass loss experiments is that FDS5 appears to predict mass loss rates reasonably well, assuming that the proper material input parameters can be determined. This latter step can be challenging.

4.2. Flame size as a method to determine the heat release rate from a flame.

A few experiments slated to fly on the International Space Station concern solid sample combustion. The hardware has already been built, but the researchers now feel that getting the value of the heat release of the burning sample would be of use. In order to allow the researchers to extract heat release rate data from their experiments, we developed an experimental technique for simultaneously obtaining the flame size, heat release and smoke point for flames over condensed-phase materials [12,13]. From these, a correlation can be determined so that the heat release rate can be obtained solely from the optically measured flame area. The data show that recorded images of the luminous flame (from soot emission) and that from CH emission (approximating the stoichiometric contour) diverge above the smoke point fuel addition rate so that the smoke point is readily determined. The flame area based on the stoichiometric contour is superior to the flame height from the luminous flame for correlating heat release rate. In addition, there exist several important considerations with regard to the actual implementation of the technique in a screening apparatus. For the small flames used, account must be made of the unsteady and the multi-dimensional heat loss terms in the energy balance equation, since these can greatly reduce the effective heat input to the sample from the radiant source.

5. Significance of Research Results

Eventually, a numerical fire code such as FDS can be used to accurately predict fires in variable gravity (for which experimental data are difficult to obtain). In the course of our work, however, we found that a major requirement in the prediction of fire growth is determination of the mass loss rate of the solid combustible material (which supplies the fuel). Good progress has been made in understanding the accuracy with which the material properties must be obtained, and their influence on the burning rate under a range of conditions.

We have devised and characterized the accuracy of a new method to obtain the heat release rate of a burning polymer based on optical measurements of the flame area. Such a method can be used for space-based materials flammability studies in which the mass loss rate or heat release rate are otherwise difficult to obtain, but the flame area is not.

We have developed a new method to obtain the smoke point of flames over polymers. The smoke point has practical application in that flame radiation heat losses, incompleteness of combustion, and smoke formation are all correlated with the smoke point.

We have used numerical simulations with FDS to understand limitations to oxygen transport for large fires in a typical module on the International Space Station. We have shown that while zero-gravity environments ($0 g_n$) environments can produce severe oxygen transport limitations for large fires, the levels of gravity typical of moon or Mars bases create buoyant mixing environments which allow oxygen transport much closer to conditions at $1 g_n$.

Finally, we have contributed to an understanding of the flame extinction mechanisms of co-flow diffusion flames in $1 g_n$ and variable g_n . This will allow more accurate flammability maps to be used for flames in variable g_n in the presence of inert or chemically-acting suppressants.

6. Publications

Peer-Reviewed Journal Articles:

1. Linteris, GT, Gewuerz, L, McGrattan, KB, Forney, GP, "Modeling Solid Sample Burning," in *Fire Safety Science: Proceedings of the Eighth International Symposium*, International Association for Fire Safety Science (IAFSS). Sept. 18-23, 2005, Beijing, China, Intl. Assoc. for Fire Safety Science, Boston, MA, Gottuk, D. T.; Lattimer, B. Y., Editor(s), 625-636 pp, 2005.
2. Linteris, G.T., "Numerical Simulations of Thermoplastic Pyrolysis Rate: Effect of Property Variations," accepted for publication in *Fire and Materials*, Sept. 2010.

3. Takahashi, F, Linteris, GT, Katta, VR, "Extinguishment Mechanisms of Co-flow Diffusion Flames in a Cup-Burner Apparatus," *Proceedings of the Combustion Institute*, **31**: 2721-2729, 2007.
4. Takahashi, F, Linteris, GT, Katta, VR, "Vortex-Coupled Oscillations of Edge Diffusion Flames in Co-flowing Air with Dilution," *Proceedings of the Combustion Institute*, **31**:1575-1582, 2007.
5. Linteris, GT, Takahashi, F, and Katta, VR, "Cup Burner Flame Extinguishment by CF₃Br and Br₂," *Combustion and Flame*, **149**:91-103, 2007.
6. Linteris, GT, Rumminger, MD, Babushok, V.I. "Catalytic Inhibition of Laminar Flames by Metal Compounds," accepted for publication in *Progress in Energy and Combustion Science*, July 2007.
7. Linteris, G.T. and Rafferty, I.P., "Flame Size, Heat Release, and Smoke Points in Materials Flammability," *Fire Safety Journal*, **43**: 442 – 450, 2008.
8. Linteris G.T., Rafferty I.P. "Scale Model Flames for Determining the Heat Release Rate from Burning Polymers." in *Progress in Scale Modeling*, Ed. K. Saito. Tokyo, 2008, pp. 235-245.

Conferences, Internal Reports:

1. Linteris, GT, McGrattan, KB and Rafferty, I.P., "Towards Modeling Large Fires in Variable Gravity" *Proceedings of the Central States Section of the Combustion Institute*, Cleveland, OH, May 21-23, 2006.
2. Linteris, GT, Takahashi, F, and Katta, VR, "Fuel Effects in Cup-Burner Flame Extinguishment," *Proceedings of the Fifth Joint Meeting of the U.S. Sections of The Combustion Institute*, San Diego, CA, March 26-28, 2007.
3. Linteris, G.T., "Modeling Solid Sample Burning with FDS," National Institute of Standards and Technology, **NISTIR 7178**, Gaithersburg MD, Oct., 2004, 36 p.

7. References

1. Linteris, G. T., McGrattan, K., and Rafferty, I. P., "Towards Modeling Large Fires in Variable Gravity," Proceedings of the Central States Section of the Combustion Institute, Cleveland, OH, Combustion Institute, Pittsburgh, PA, 2006.
2. Takahashi, F., Linteris, G.T. , Katta, V.R., "Diffusion Flame Extinguishment in Microgravity," 56th International Astronautical Congress, Fukuoka, Japan, Fukuoka, Japan, 2005.
3. V.R. Katta, F. Takahashi, G.T. Linteris, *Combustion and Flame* 137 (4) (2004) 506-522.
4. Takahashi, F., Linteris, G.T. , Katta, V.R , "Extinguishment Mechanisms of Cup-Burner Flames," 44th Aerospace Sciences Meeting and Exhibit, Reno, NV, AIAA, 2006, pp. AIAA Paper No. 2006-0745.
5. Takahashi, F., Linteris, G.T. , Katta, V.R., "Suppression characteristics of cup-burner flames in low gravity," 42nd Aerospace Sciences Meeting and Exhibit, Reno, NV, AIAA, 2004, pp. AIAA Paper No. 2004-0957.
6. Linteris, GT, Gewuerz, L, McGrattan, KB, Forney, GP, "Modeling Solid Sample Burning," in *Fire Safety Science: Proceedings of the Eighth International Symposium*, International Association for Fire Safety Science (IAFSS). Sept. 18-23, 2005, Beijing, China, Intl. Assoc. for Fire Safety Science, Boston, MA, Gottuk, D. T.; Lattimer, B. Y., Editor(s), 625-636 pp, 2005.
7. Linteris, G.T., "Numerical Simulations of Thermoplastic Pyrolysis Rate: Effect of Property Variations," accepted for publication in *Fire and Materials*, Sept. 2010.
8. Linteris, G.T. and Rafferty, I.P., "Flame Size, Heat Release, and Smoke Points in Materials Flammability," *Fire Safety Journal*, **43**: 442 – 450, 2008.
9. Linteris G.T., Rafferty I.P. "Scale Model Flames for Determining the Heat Release Rate from Burning Polymers." in *Progress in Scale Modeling*, Ed. K. Saito. Tokyo, 2008, pp. 235-245.

APPENDIX I – Major Publications Describing the Work Performed

Towards Modeling Large Fires in Variable Gravity*

G.T. Linteris, K. McGrattan, and Ian Rafferty
Fire Research Division
National Institute of Standards and Technology
Gaithersburg, MD 20899-8665

Abstract

Fires with prescribed fuel release rates are modeled in 1 g_n and reduced-gravity environments. The burner diameter, gravity level, and ventilation flow rate are varied to assess the limitations of oxygen transport to the flame in controlling the maximum heat release rate. The simulations indicate that in 0 g_n , for burners of radius $r=5$ cm to $r=15$ cm, and airflows of 0 cm/s to 10 cm/s, laminar flames are often limited by oxygen transport. Nonetheless, with gravitational accelerations above 1/6 g , or with the gas burner installed in a typical lab module (which has turbulent ventilation flows), oxygen transport to the flame is not a limiting factor for heat release.

Introduction

No large, on-orbit fires have occurred in U.S. space craft to date. Yet with the advent of operations on the International Space Station (ISS), possible long-duration missions to the moon and Mars, and more varied crews and missions of the U.S. Space Shuttle, one must expect the eventual occurrence of a serious accidental fire. One large, uncontrolled fire in space has already occurred on the Russian Mir space station in 1997 [1] which fortunately was extinguished before loss of life or extensive damage to the vehicle occurred. It is useful to develop methods for describing the conditions under which a large-scale fire could occur on a spacecraft, so that those conditions can be avoided. Further, knowledge of large-scale fire behavior in space will aid in developing techniques to limit the fire's progression in the vehicle and suppress it.

The basic hypothesis of the present work is that given the wide use and utility of fire models for describing fires in normal gravity, the time is appropriate for modifying them to describe large-scale fires in microgravity, and using them to learn about the dynamics of large fires in spacecraft.

Specific Objectives

The objective of the present work is to extend the capabilities of a computational fluid dynamics (CFD) fire model so that it can accurately describe large fires in reduced gravity modules used for transport and habitation in space exploration. It will then be used to understand the behavior of and risks from large fires so that the safest practices can be used, maximizing crew and vehicle survivability. The present work investigates the roles of buoyancy- and ventilation system-controlled air flow on the oxygen transport to

the flame with regard to the maximum overall heat release rate.

Approach

An obvious change to describe large microgravity fires would simply involve turning off the gravity body force term in the momentum equation. This might work acceptably well for non-reacting flow; however, for flow with combustion, there are several phenomena which are currently approximated in fire codes via simplified empirical models—based on 1-g large-scale fire tests. These include radiation from soot, flame spread and burning rates of condensed-phase materials, and extinction maps for the gas-phase flames. Hence, applying a model to spacecraft fires in variable gravity will require modification of these algorithms, or development of new approaches to treat the relevant phenomena. This paper presents the first exploratory work towards these goals.

Numerical Model

The variable-gravity fires were described with the National Institute of Standards and Technology (NIST) Fire Dynamics Simulator (FDS) version 4 [2], and the results interpreted with the companion visualization program Smokeview [3]. The low-Mach number formulation of the Navier-Stokes equations is used to predict the gas movement. With fuel present, the model predicts the flame location based on the mixture fraction, in which the fuel and oxygen consumption, as well as the heat release, occur in the grid cells for which the fuel and oxygen are present in stoichiometric proportions. Radiation heat transfer from hot surfaces is calculated assuming unity emissivity; for the gases, gray body radiation is calculated (with a prescribed

* Appeared as: Linteris, G.T., McGrattan, K.B. and Rafferty, I.P., "Towards Modeling Large Fires in Variable Gravity" *Proceedings of the Central States Section of the Combustion Institute*, Cleveland, OH, May 21-23, 2006.

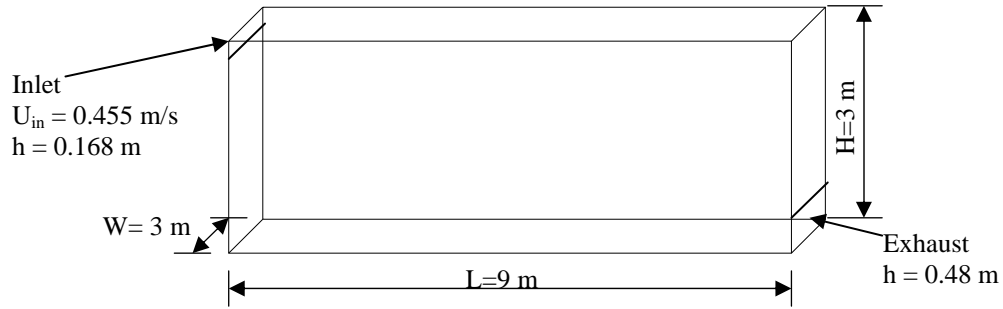


Fig. 1. Geometry for the forced convection case.

soot volume fraction, based on over-ventilated, 1 g_n results).

Results and Discussion

This paper provides preliminary investigation of two aspects of the problem of predicting fires in variable gravity: 1.) validation of the sub-grid models of turbulence in FDS for conditions similar to those expected to be encountered in spacecraft; and 2.) exploration of the global effects of gravity and ventilation on the potential heat release from a fire.

Validation of Forced Ventilation Simulation

Experimental data on ventilation flows in variable gravity are not yet available. Nonetheless, there are experimental data in the heating and ventilation literature for isothermal, low speed air flow in simple geometries; these are relatively close to the conditions expected for low-gravity vehicles and habitation modules. A particularly useful dataset is that of forced convection in a single compartment, as shown in Fig. 1. Experimental measurements for this configuration were done by Restivo [4], and have been used in validation of many CFD codes [5,6], including FDS [7]. The inlet air enters the room from a vent in the top edge of one wall, along the ceiling, with a uniform velocity of 0.455 m/s. A passive exhaust is located near the floor on the opposite wall, with conditions specified such that there is no buildup of pressure in the enclosure. For the FDS simulation, the initial conditions included no air motion.

To illustrate the effect of grid refinement on both the simulation results and computing time, several grids were investigated. Details can be found in ref [8]. The volume near the inlet needs a fairly fine grid to capture the mixing of air at the shear layer. For the results shown here, the height of the inlet was spanned with 6 grid cells, roughly 3 cm in the vertical dimension, 6 cm in the other two. Finer grids were used in ref. [8], but with no appreciable change in results.

Fig. 2, Fig. 3, Fig. 4, and Fig. 5 show simulation

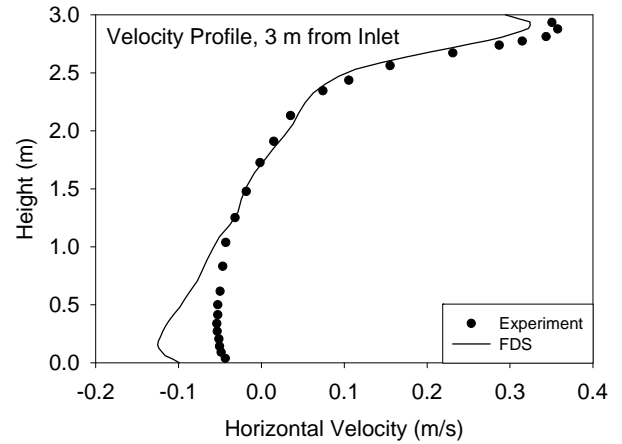


Fig. 2. u-component of velocity as a function of height at a distance 3 m downstream from the inlet.

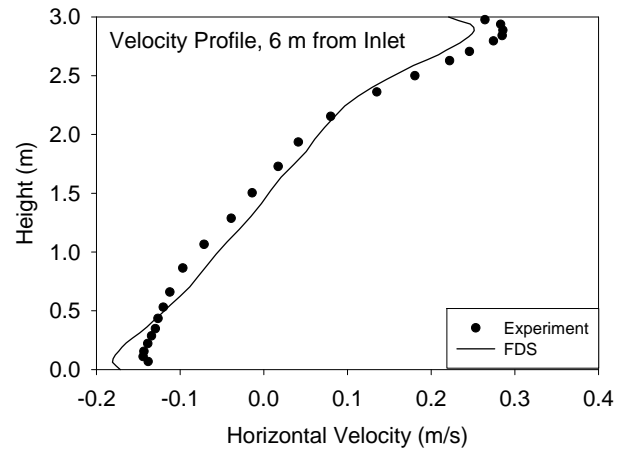


Fig. 3. u-component of velocity as a function of height at a distance 6 m downstream from the inlet.

results plotted with the measured experimental data. The u-component of velocity was measured in four arrays: two vertical arrays located at 3 m and 6.0 m from the inlet along the centerline of the room, and two horizontal arrays located near the floor ($h=0.084$ m) and ceiling ($h=2.916$ m). These measurements were taken

using hot-wire anemometers. As the figures show, the numerical calculation is able to predict the velocities reasonable well, providing some validation to the sub-grid turbulence model used in FDS for the present conditions. Of course it is possible to refine the various aspects of the CFD model, including the large eddy simulation (LES) formulation, wall treatment, etc., but the present overall accuracy is sufficient for the intended use.

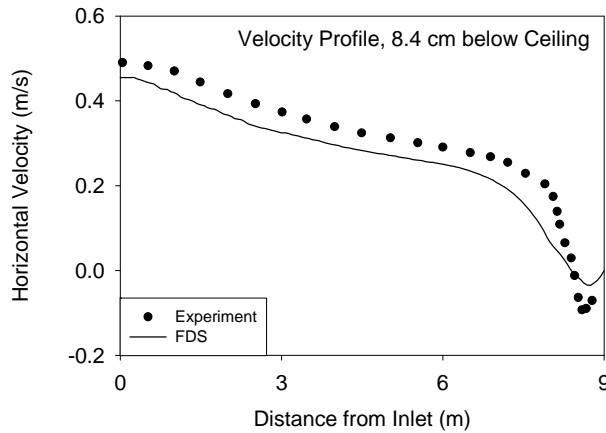


Fig. 4. u-component of velocity as a function of distance downstream from the inlet, 8.4 cm below ceiling.

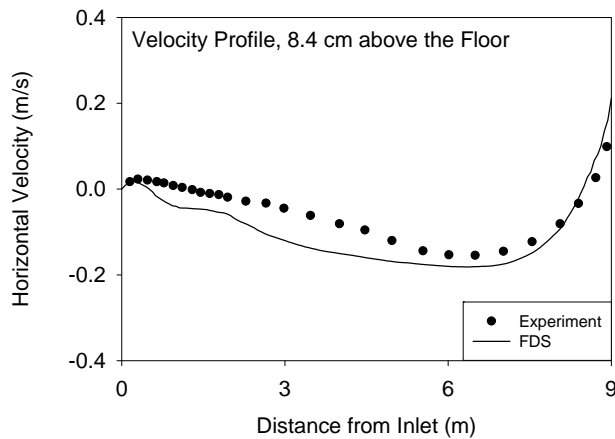


Fig. 5. u-component of velocity as a function of distance downstream from the inlet, 8.4 cm above the floor.

Effects of Ventilation and Buoyancy-Induced Flow

In order to examine the global effects of ventilation and buoyancy on the burning behavior, we simulated a laminar burner ejecting propane at a fixed mass flow rate, with a co-flow of air. The flow rate of propane was selected to match approximately the heat release rate of a poly methyl methacrylate (PMMA) slab in 1-g burning with heat feedback from the flame only. Fig. 6

shows the heat release rate in the gas phase for $r = 15$ cm in $0 g_n$ with increasing air flow rate, from 0 cm/s to 10 cm/s. As indicated, for

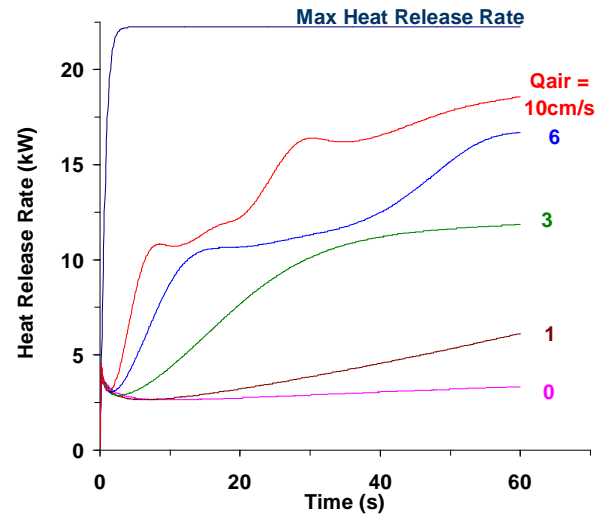


Fig. 6. Total heat release in the gas phase from a simulated diffusion flame of $r=15$ cm, in $0 g_n$, with an air flow rate of 0 cm/s to 10 cm/s.

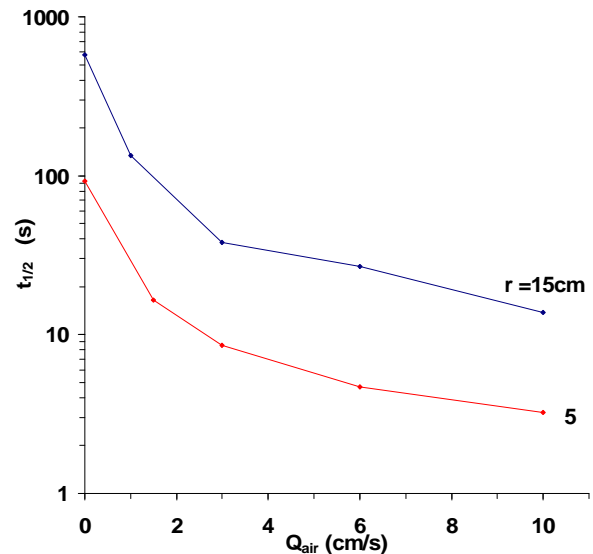


Fig. 7. Time required for a laminar co-flow diffusion flame in $0 g_n$, with burner radius $r=5$ cm and $r=15$ cm, to reach one-half of the maximum possible heat release, as a function of co-flow air velocity.

flames of this scale, in $0 g_n$, with air flows typical of the ventilation rates in spacecraft (6 cm/s to 20 cm/s), oxidizer availability could limit the heat release rate.

Simulations were also performed for burners with radius $r = 5$ cm to 15 cm, and air velocities of 0 cm/s to

10 cm/s. Fig. 7 shows the time it took for the flame to reach one half the maximum possible for burners with $r = 5$ cm and $r = 15$ cm. (Note the log scale on the ordinate, and that the time at $Q_{\text{air}} = 0$ cm/s is probably a minimum, since a large extrapolation was necessary for this estimate.) As the figure shows, in $0 g_n$, small increases above 0 cm/s in the air velocity have a large effect on the oxygen availability for the fire, greatly accelerating the fire growth rate.

The importance of ventilation flow on the flame spread rate of paper samples in $0 g_n$ has been described previously [9], for much smaller flames. The present results extend those findings to larger size flames.

The results shown in Fig. 6 and Fig. 7 were calculated for $0 g_n$. It is of interest to determine the changes for this simple geometry for reduced (but not zero) gravity conditions. As Fig. 8 ($r=5$ cm) and Fig. 9 ($r=15$ cm) show again, the $0 g_n$ results produce very low heat release rates (due to oxygen limitations); however, with any gravity level above $1/6 g$, the predicted heat release rates are comparable to those obtained for $1 g_n$. (Note that the oscillations are due to buoyancy-induced flame puffing, and that all data in Fig. 8 and Fig. 9 are time averaged over a period of about 0.1 s.)

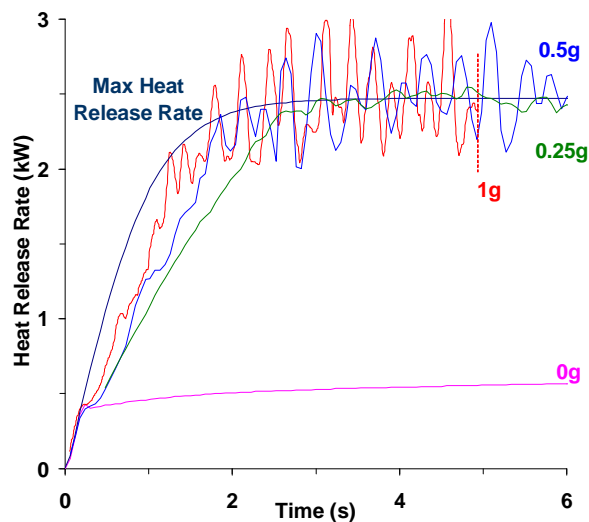


Fig. 8. Heat release rate of flames with $r=5$ cm, 0 cm/s air flow, in $(0, 0.25, 0.5,$ and $1) g_n$.

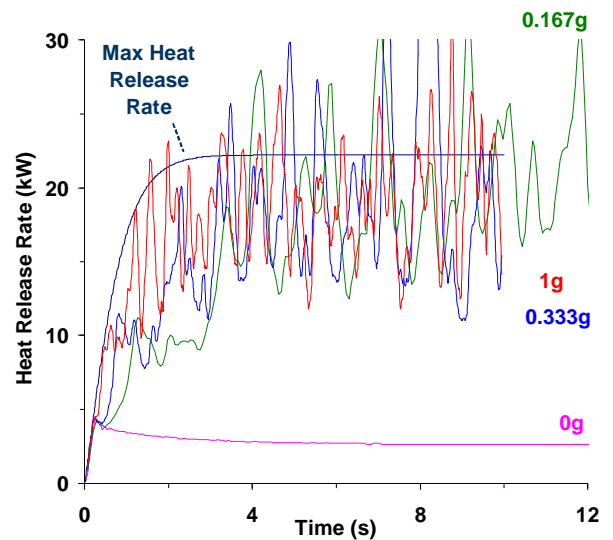


Fig. 9. Heat release rate of flames with $r=15$ cm, 0 cm/s air flow, in $(0, 0.167g, 0.33g,$ and $1) g_n$.

In addition to adding a mild co-flow at the base of the simple burner, one can also put the burner into a realistic module flow. Using ventilation flow design information from a US lab module [10], we put a propane burner with a mass flow corresponding to a maximum heat release rate of $(5, 10, 25,$ and $50)$ kW at a central location in a representative US lab module of the International Space Station (ISS). Fig. 10 shows the calculated heat release from a 30 cm by 30 cm burner with propane released to provide the desired maximum heat release in kW (kW/m^2 in parentheses). All curves are for $0 g_n$, except the one additional case for 25 kW, marked “ $1 g_n$ ” (solid orange curve). As indicated, for all cases the heat release quickly rises to that near the maximum based on the fuel flow rate, and there is significant oscillation (near 1 Hz), which increases in magnitude as the fire size increases. As shown, the heat release rate quickly rises to the maximum possible, and then is constant. The $0 g_n, 25$ kW heat release case, while it has the same average value, oscillates somewhat, and (as do all the $0 g_n$ cases) requires some time for the initial fuel and air mixing.

To investigate the above assumption that ventilation flows are appropriate for studying fires in low g , we looked at calculated flow field in the module with the 25 kW fire. Analyses showed that the peak velocities were not changed much in $0 g_n$ with the fire; however, for a module in $1 g_n$, the velocities were much higher than those due to the ventilation flow (as expected).

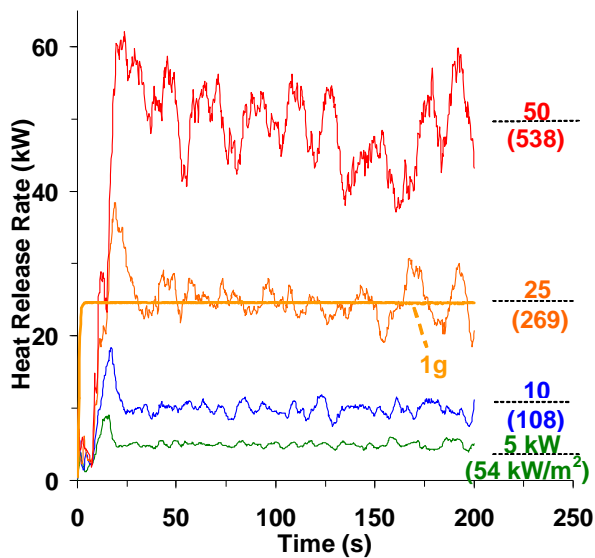


Fig. 10. Calculated heat release rate from a propane burner with specified mass flow (corresponding to: top label, kW; bottom label, kW/m²); all in ISS lab module, 0 g_n, except curve marked 1 g_n.

Conclusions

The present calculations examined one question: Under what conditions will a fire in low gravity be non-viable due to limitations on the transport of oxygen to the flame? The calculations presented here indicate that for uniform, co-flowing, laminar inlet flow, and fuel sources of representative size ($r=5$ cm to $r=15$ cm) the heat release rate can be limited by the supply of air. For higher air flow and smaller flames, the flames reach near peak values after about 20 s, whereas for larger flames with lower airflow, the heat release can be oxygen limited. Nonetheless, with any level of gravity above $1/6$ g, there is sufficient buoyancy driven flow to make the heat release rate comparable to 1 g_n results.

A most important conclusion, however, is that putting the same burner into a 0 g_n module with representative turbulent flow provides sufficient air so that the flames behave much more like flames in 1 g_n than laminar co-flow flames in 0 g_n.

Of course, other factors are crucial for assessing fire risk (such as flame spread, gas-phase extinction due to heat losses, etc.). Further work will aim to determine the influence of these factors on large microgravity fires.

Acknowledgements

This research was supported by the Office of Biological and Physical Research, National Aeronautics and Space Administration, Washington, DC.

References

1. Friedman, R. and Ross, H.D., in *Microgravity Combustion: Fire in Freefall* (Ross, H. D., Ed.), Academic Press, New York, 2001, pp. 525-562.
2. McGrattan, K. B., *Fire Dynamics Simulator (Version 4) Technical Reference Guide*, NISTSP 1018, 2004.
3. Forney, G. P. and McGrattan, K. B., *User's Guide for Smokeview Version 4 - A Tool for Visualizing Fire Dynamics Simulation Data*, NISTSP 1017, 2004.
4. Restivo, A., *Turbulent flow in ventilated rooms*, University of London, Mechanical Engineering Department, 1979.
5. Davidson, L. and Nielsen, P., Large eddy simulation of the flow in a three-dimensional ventilated room, presented at *Roomvent '96, Vol. 2*, 1996, pp.
6. Zhang, W. and Chen, Q., Large eddy simulation of natural convection flow in a room with a filtered dynamic subgrid scale model, presented at *International Symposium on Computational Technologies for Fluid/Thermal/Structural/Chemical Systems with Industrial Applications. PVP-Vol. 297-1*, 1999, pp. 263-268.
7. Emmerich, S. and McGrattan, K., *ASHRAE Transactions* 104(1B):1128 (1998).
8. Musser, A., McGrattan, K. B., and Palmer, M. E., *Evaluation of a fast, simplified computational fluid dynamics model for solving room airflow problems*, NISTIR 6760, 2001.
9. Friedman, R. and Urban, D.L., *AIAA paper 93-1152*, (1993).
10. Son, C. H. and Lin, C. H., *Computational Fluid Dynamics (CFD) Ventilation Analysis Report For The International Space Station Flight 5A*, Boeing 5-5352-ECLS-CHS-00-046, 2000.

Modeling Solid Sample Burning with FDS¹

G.T. Linteris, L. Gewuerz, K. McGrattan, and G. Forney
Building and Fire Research Laboratory
National Institute of Standards and Technology

October 18, 2004

Abstract

Black PMMA was burned in the cone calorimeter in two orientations (horizontal and vertical), at imposed radiant heat fluxes of (0, 5, 10, 25, 50, and 75) kW/m², and the visual appearance, flame size, heat release rate, and mass loss rate were recorded. Various other experimental parameters were varied. The topography of the burned samples was also recorded, and the heat flux to the sample was inferred from the variation of the mass loss over the surface of the sample. The burning was subsequently modeled using the NIST Fire Dynamics Simulator, and various experimental, numerical, and physical parameters were varied in the simulations. The results provide an indication of the ability of FDS to predict the burning of a simple solid sample, and also provide guidance concerning the importance of various experimental and numerical parameters for accurate simulation.

Introduction

The NIST Fire Dynamics Simulator (FDS) [1,2], and the companion visualization program Smokeview[3], is a widely used computational fluid dynamics package which was originally written for predicting the movement of smoke and hot gases in building fires[2]. Recently, its capabilities have been systematically extended to include fire growth and spread. Predicting these phenomena is challenging, and experimental data are required to validate the code's accuracy. Clearly, intermediate and large-scale tests are required; however they are expensive and time consuming. It is also necessary to validate the sub-grid scale models with small-scale tests. The ultimate goal of the present work is to improve the treatment of the solid phase in FDS. As a first step, small scale experiments were conducted in the NIST cone calorimeter and FDS was used to predict the burning rate. This provides some measure of FDS capacity for predicting fire growth,

¹ Appeared as:

Linteris, G.T., "Modeling Solid Sample Burning with FDS," National Institute of Standards and Technology, **NISTIR 7178**, Gaithersburg MD, Oct., 2004, 36 p, and

Linteris, G.T., Gewuerz, L., McGrattan, K.B., and Forney, G.P., "Modeling Solid Sample Burning," in *Fire Safety Science: Proceedings of the Eighth International Symposium*, International Association for Fire Safety Science (IAFSS). Sept. 18-23, 2005, Beijing, China, Intl. Assoc. for Fire Safety Science, Boston, MA, Gottuk, D.T.; Lattimer, B.Y., Editor(s), 625-636 pp, 2005.

since an ability to predict the burning of such a simple configuration is a clear prerequisite for modeling large fires which ultimately will also involve burning on the scale of cone samples. Hence, the short term goal of this project is to assess the relative importance of various numerical, physical, and experimental parameters on the predicted burning of the sample. In addition to providing a validation of FDS's abilities at this scale, the tests and modeling also serve as a benchmark so that eventual changes to the treatment of the solid phase can be compared with a baseline case.

In order to avoid the complex phenomena which occur during the burning of some polymers (for example, bubbling, dripping, char formation, micro-explosions, complex time-dependent decomposition, etc.) [4], PMMA (a simple, well characterized and well behaved, non-charring, non-dripping polymer) was selected. Although it is desired to study these other parameters as well, their investigation will be conducted in future work, since their treatment is clearly beyond current modeling capabilities for burning samples.

In the experiments, the parameters varied include sample orientation (horizontal, inverted, and vertical), radiant flux (0 to 75) kW/m², cone presence (for the 0 flux case), and the sample edge and backing condition. In the numerical modeling, these parameters were varied, as well as those pertaining to the sample physical properties, and those relevant to the numerical solution (domain size, resolution, etc.).

Experiment

Black PMMA samples, 10 cm x 10 cm x 2.54 cm, were burned in the NIST cone calorimeter (Figure 1). The samples were insulated on the back side with 6 cm of Kaowool² insulation, and had 0.77 mm thick cardboard around the perimeter. The heat release rate of the burning sample as a function of time was determined with oxygen consumption calorimetry (assuming a heat release of 13,125 kJ/kg-O₂); the visual flame size and mass loss rate were also recorded. The cone apparatus was modified from its normal operating configuration so that the surface of the cone heater closest to the sample was maintained at 2.54 cm from the burning PMMA sample (i.e., the cone was translated as the sample surface regressed). During the tests it was observed that the sample surface regression rate was non-uniform over the sample, and hence the sample final height as a function of position over the sample surface could be used to provide the varying heat flux (or regression rate) for comparison with the numerical calculations. To measure the surface height as a function of position on the sample, a custom-built system was used. Stepper motors positioned the sample under a contact-switch surface probe, which determined the local sample height. Repeating the process on a 20 x 20 grid allowed characterization of the burned sample topography.

² Certain commercial equipment, instruments, or materials are identified in this paper to adequately specify the procedure. Such identification does not imply recommendation or endorsement by NIST, nor does it imply that the materials or equipment are necessarily the best available for the intended use.

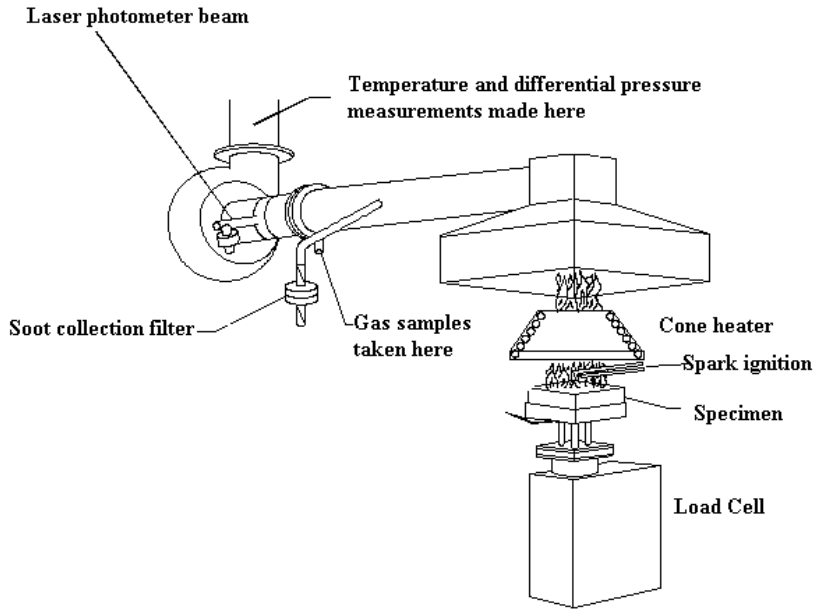
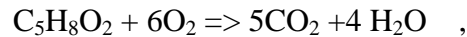


Figure 1 – NIST cone calorimeter [5].

Numerical Calculations

The burning of the cone samples was predicted with FDS version 4. The low-Mach number formulation of the Navier-Stokes equations is solved to predict the gas movement. For PMMA combustion, the MMA monomer ($C_5H_8O_2$) is assumed to be liberated from the sample surface when the surface reaches the ignition temperature. The rate of mass loss is determined from an energy balance at the surface, with all net incident energy being used to decompose and vaporize the PMMA (accounted for with a “heat of vaporization”). The code predicts the flame location based on a mixture fraction formulation, in which the fuel and oxygen consumption, as well as the heat release, occur in the grid cells for which the fuel and oxygen are present in stoichiometric proportions. Complete combustion at the flame sheet is assumed via the reaction:



(although slight modifications to the stoichiometric coefficients are made to account for empirically determined yields of soot and CO). Radiation heat transfer from hot surfaces (i.e., the cone and the hot surface of the PMMA) is calculated assuming unity emissivity; for the gases, gray body radiation is calculated (with a prescribed soot volume fraction and otherwise transparent gases).

In order to make the run times reasonable, the code was run primarily in the 2-D mode (planar for the vertical and inverted cases, and axisymmetric for the horizontal case). Calculations were performed for samples in the horizontal, inverted, and vertical

orientation. Some 3-D calculations were also run for comparison, and to obtain the surface regression rate variation over the surface of the sample.

The experimental configuration for the horizontal and vertical cases was that of the NIST cone calorimeter as illustrated in Figure 2 and Figure 3. For the inverted case, data were taken from Olson et al. [6], and the configuration is illustrated in Figure 4. For samples with an imposed flux, the cone was located 2.54 cm from the top of the PMMA surface; for those with no imposed flux, the cone was typically not present in the calculation domain. All boundaries of the calculation domain (except the sample) were open (ambient pressure), except for the inverted cone case, for which there was an imposed flow up through the middle of the cone calorimeter.

Experimental Results

The data available from the experiments were flame visual images, the gas-phase heat release rate, and the sample mass loss rate, all as a function of time. In addition, the sample final mass and the topography of the burned samples were recorded. Images of the flames from burning PMMA in the horizontal configuration are shown in Figure 5 for imposed heat fluxes from the cone of: (0, 5, 10, 25, and 75) kW/m². The thick black horizontal stripe across the flame image (for all except the 0 flux case) is the cone heater, which occludes the flame. The corresponding images (at 0, 5, 10, 25, and 75) kW/m² for the vertical configuration are shown in Figure 6. In these images, the cone heater is just to the left of the flame (note that unfortunately, the camera view was different for the images in Figure 6, so some flame images are clipped). The heat release rate as a function of time for the burning horizontal samples is shown in Figure 7. As the figure shows, higher imposed heat fluxes lead to higher heat release rates and shorter ignition times; once ignited, the heat release increases rapidly; and the vertical and horizontal cases yield very similar heat release rates. The data also show that minor changes to the sample configuration can significantly influence the heat release rate. For example, for the 0 flux, horizontal case (labeled 0H), scraping the carbon left from the burned cardboard edge at the sample perimeter, or flipping the cold cone up or down, can each have about a 20 % effect on the burning rate. These effects are discussed below.

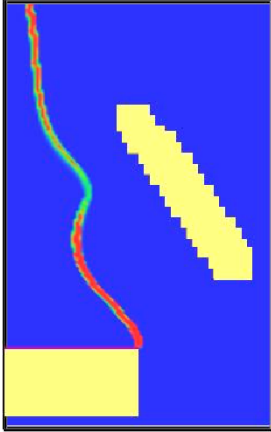


Figure 2 – Calculation domain for PMMA burning in the horizontal orientation. The calculation is 2-D axisymmetric, and the axis of symmetry is on the left side of this figure.

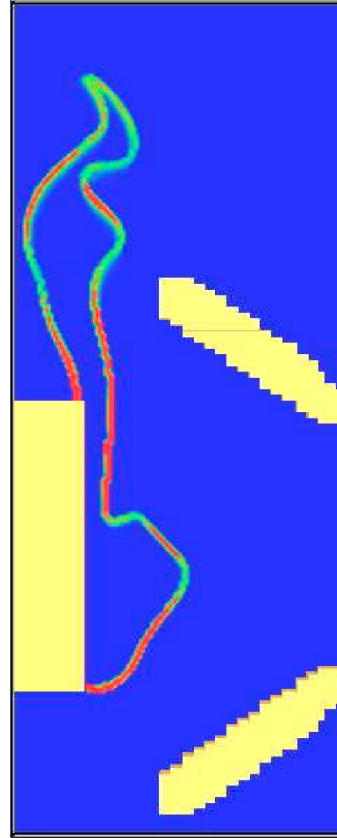


Figure 3 - Calculation domain for PMMA burning in the vertical orientation. The calculation is 2-D planar (hence the cone is also 2-D planer instead of axisymmetric).

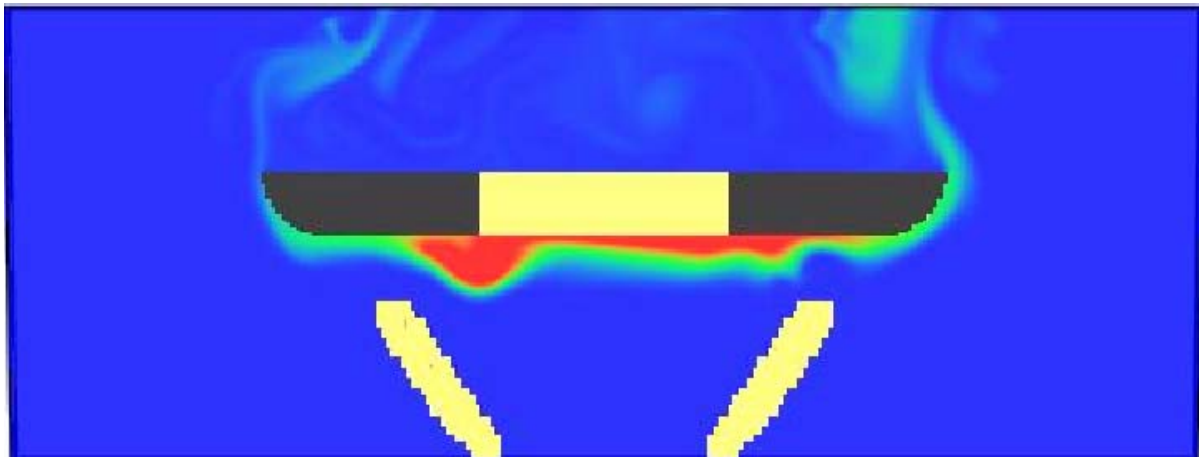


Figure 4 - Calculation domain for PMMA burning in the inverted orientation (calculation is 2-D planar).

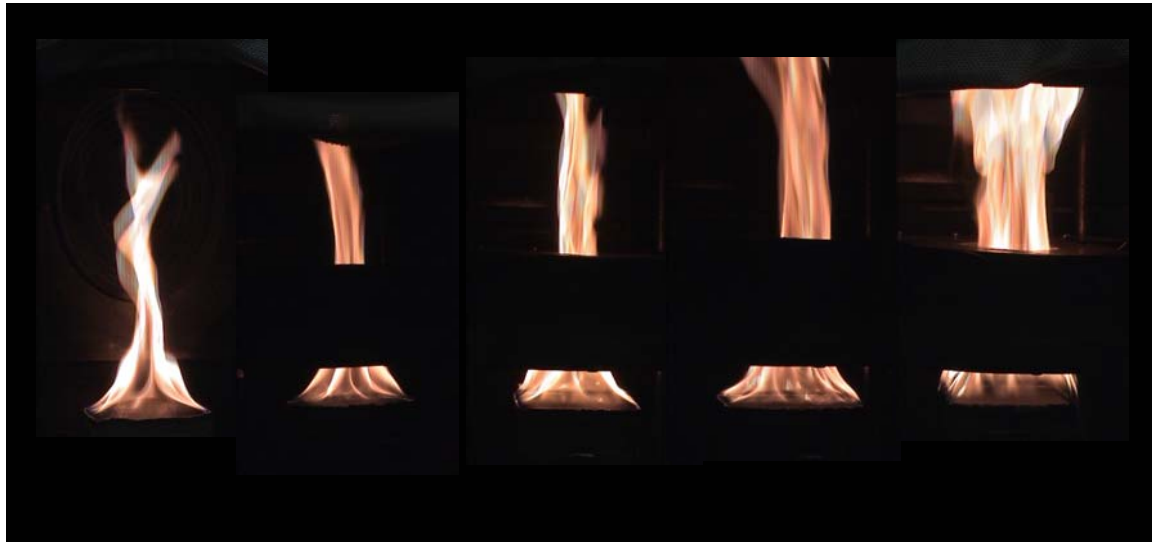


Figure 5 – Experimental flame images of PMMA samples burning in the horizontal configuration for (0, 5, 10, 25, and 75) kW/m².



Figure 6 - Experimental flame images of PMMA samples burning in the vertical configuration for (0, 5, 10, 25, 50, and 75) kW/m².

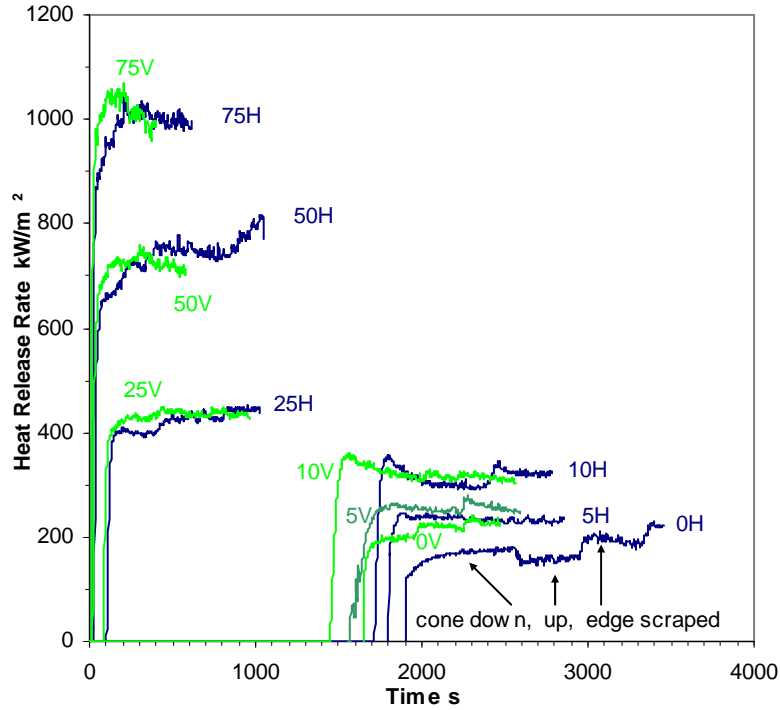


Figure 7 – Experimental heat release rate of horizontal H and vertical V samples of PMMA in the cone calorimeter for imposed heat fluxes of (0 to 75) kW/m². (Note: the time to the start of the heat release represents the ignition time at that heat flux; however, for (0 and 5) kW/m², ignition would not occur, so the curves are shown on the plot transposed 200 s and 100 s, respectively, from the ignition time for the 10 kW/m² case, respectively.

The samples did not burn uniformly over their exposed surface, and the effect was more pronounced at the lower flux levels. For example, the final condition of the horizontal sample at 0 kW/m² is shown in Figure 8. From such samples, the burning rate variation over the surface of the sample can be determined.

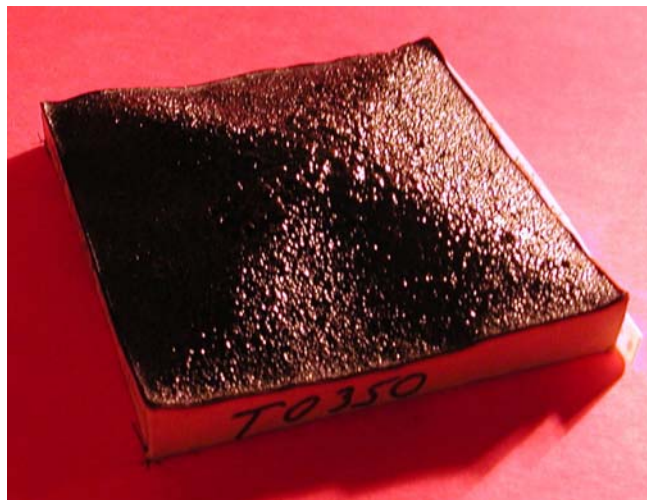


Figure 8 – Black PMMA sample, horizontally exposed to 0 kW/m² in the cone, after burning for 26 min.

Numerical Results

The calculations were performed at the Linux cluster at BFRL of NIST, on 1.7 GHz to 3.2 GHz. Pentium 4 machines. The default domains used were 16 cm x 16 cm for horizontal and 27 cm x 6 cm for vertical orientations. The Smokeview visualization program allows seamless investigation of the problem set up, the calculation progress, and the thermal and fluid dynamic results of the simulation, facilitating comparisons with experiments. Two-dimensional calculations in the horizontal or vertical orientation typically took 0.5 h or 1 h for 1 s of simulation, and 3-D calculations took 72 h per 1 s of simulation.

The input parameters for the reaction and surface properties of PMMA are listed in Table 1; these conditions represent the baseline case. The physical properties of the PMMA sample were taken from the literature [7]. In Table 1, RADIATIVE_FRACTION is set to zero so that radiation from the flame gases is calculated by FDS (the alternative is to set some fraction of the flame heat release, say 30 %, to be lost by radiation, rather than to solve the radiative transport equations directly). Since the computation grid is relatively fine for this calculation, the radiative transport equation should give good results and the empirically based value is not necessary.

Table 1 – FDS input file reactant and surface parameters for PMMA.

```
&REAC ID='MMA',  
  FYI='MMA monomer, C_5 H_8 O_2',  
  EPUMO2=13125.0,  
  MW_FUEL=100.0,  
  NU_O2=6.0,  NU_H2O=4.0,  NU_CO2=5.0,  
  RADIATIVE_FRACTION=0.0,  
  SOOT_YIELD=0.022 /
```

```
&SURF ID='PMMA',  
  RGB = 0.81,0.04,0.84,  
  HEAT_OF_VAPORIZATION=1578.0,  
  HEAT_OF_COMBUSTION=25200.0,  
  DELTA=0.025,  
  KS=0.25,  
  ALPHA=1.1E-7,  
  TMPWAL0=330.0,  
  MASS_FLUX_CRITICAL=0.004,  
  A = 8.6E5,  TMPIGN=330.0 /
```

The pyrolysis behavior of the material is approximated via the last three parameters in the table. The mass loss rate of the PMMA is given by an Arrhenius rate expression, $\dot{m}'' = A\rho e^{-E_A/RT}$, in which A and E_A are the pre-exponential and activation energy for the overall pyrolysis reaction, R is the universal gas constant and T is the surface temperature. The three parameters A,

TMPIGN, and MASS_FLUX_CRITICAL are only relevant with regard to this rate expression. That is, TMPIGN is the temperature (°C) at which the mass loss (i.e., burning) occurs. In the default condition, A is prescribed ($A=8.6E5$), and the code then selects E_A such that the specified MASS_FLUX_CRITICAL is achieved at TMPIGN. Usually, a burning temperature for a material is known, but the actual Arrhenius rate parameters are not. Hence, the goal in the code is to have each material burn at the correct temperature. The Arrhenius expression is used primarily to accomplish that, while providing a smooth function that is better numerically than a step function. Of course, if the actual global Arrhenius parameters are available, they can be used directly.

The parameters varied in the calculations include those having to do with the numerical solution, the physical properties of the sample, and the experimental configuration which is modeled. The numerical parameters varied include the domain size, grid spacing, DNS or LES calculation mode, and 2-D or 3-D calculation. The physical parameters varied were the heat of vaporization, the activation energy of the thermal decomposition step, and the ignition temperature. The fidelity of the experimental description in the calculation was varied by including or excluding such effects as the presence of the exhaust flow, the lip on the sample edge, presence of the cone above the sample (in the no-flux case), and the sample backing insulation. Finally, the major experimental parameters were varied by changing the cone temperature (i.e., the imposed heat flux), and the sample orientation (horizontal, vertical, or inverted). The effects of each of these parameters on the predicted heat release rate are described below.

Numerical Parameter Variation

Domain Size

The size of the physical domain for the horizontal case was 16 cm x 16 cm. A plot of the calculated heat release rate (HRR) in the system as a function of time is shown in Figure 9a as the small red open symbols. (Since the heat is released in the gas phase, this HRR will be referred to as the gas-phase HRR. Conversely, one can calculate the HRR from the solid-phase mass loss rate times the heat of combustion; this will be referred to as the solid-phase HRR. Note that in the calculations, no actual energy is released within the solid phase; this naming convention merely refers to how the HRR is estimated.) The solid-phase HRR is shown by the red dashes. There is large scatter in the gas-phase HRR, as well as significant discrepancy between the gas-phase and solid-phase results, with the solid-phase HRR showing about 40 % higher HRR than the average of the gas-phase HRR. As illustrated in Figure 10a, the limited physical domain leads to loss of reactants outside the domain before they are consumed, leading to a lower HRR than indicated by the burning rate (which counts all vaporized fuel as burned). For the calculation shown by the large blue circles and blue dashes, the physical domain was increased by a factor of 4 in the direction perpendicular to the horizontal sample (i.e., up) as in Figure 10b,c. With the larger domain, there is less scatter in the gas-phase HRR, the average of the gas-phase and solid-phase HRR agree better with each other, and the solid-phase HRR is about 10 % lower than that calculated for the original domain.

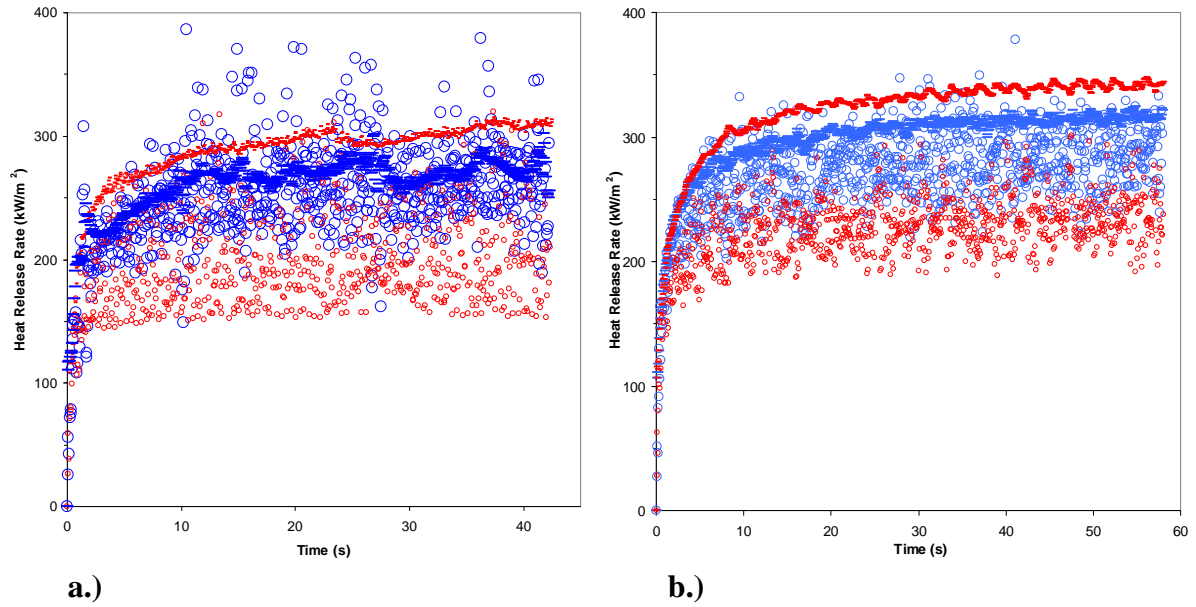


Figure 9 - Simulated heat release rate from burning PMMA a.) horizontal sample, b.) vertical sample; 2-D calculation, 1 mm grid spacing, 0 kW/m² imposed flux. Open symbols: calculated heat release rate from the gas phase; dashes: solid phase mass loss rate times the heat of combustion; red points are the original domain, blue points are the expanded domain: 4x in the z-direction for the horizontal case, 2x in the x and z direction for the vertical case.

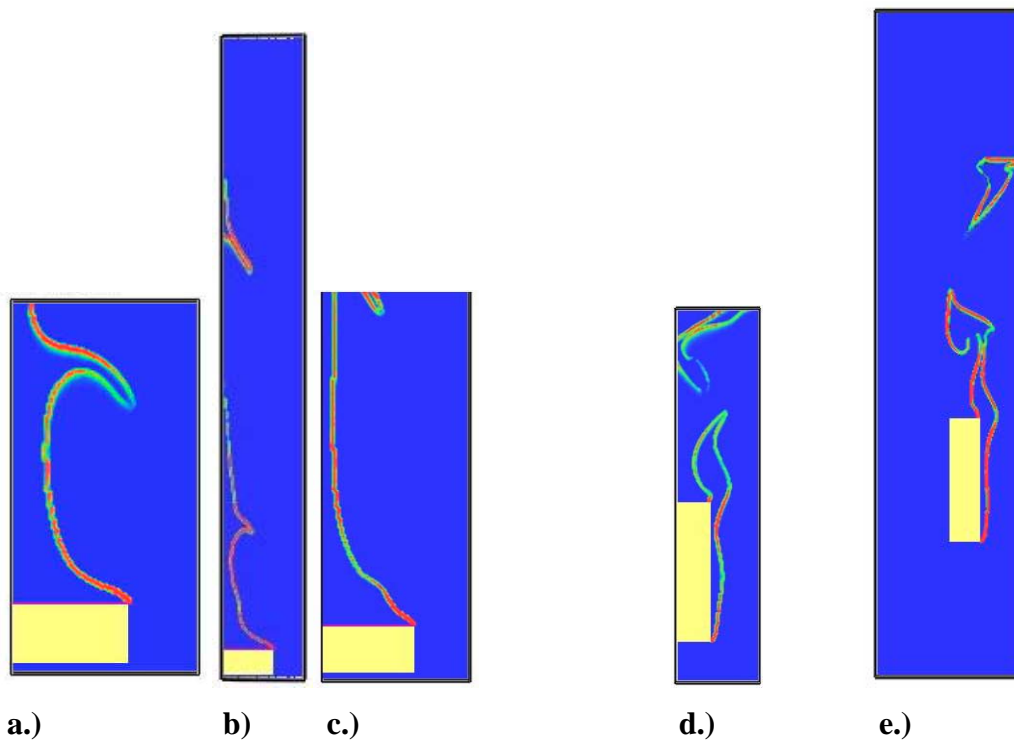


Figure 10 – Flame location from simulation; horizontal case: a.) original domain, b.) expanded by 4x in the z, c.) magnified view of b.); and vertical case: d.) original domain, e.) expanded domain.

For vertical samples, the results were similar (see Figure 9b): a larger domain leads to better agreement between the HRR predicted from the gas phase and the solid phase, and leads to a slightly lower heat release predicted by the solid-phase mass loss. For the vertical case, however, even with the larger domain, there is still a 10 % discrepancy between the average HRR predicted from the gas phase as compared to the solid phase, indicating that a still larger domain may be necessary. The flames escaping from the original calculation domain for the vertical case are shown in Figure 10d, and case of the expanded domain in Figure 10e. Note that the some of this discrepancy between the mass loss-based HRR and that calculated to occur in the gas phase may also be numerically induced.

Grid Spacing

For the vertically-oriented PMMA sample, calculations were performed using grid spacings of either 1 mm or 2 mm (in both the x and z directions), as shown in Figure 11. The results of these calculations, as illustrated in Figure 12, show a significant drop in heat release rate (about a factor of two) for the coarser grid. Furthermore, with a lower resolution, the gas-based and solid-based HRR tend to converge and the gas-based rate shows less variation. (These effects may be numerically induced.)

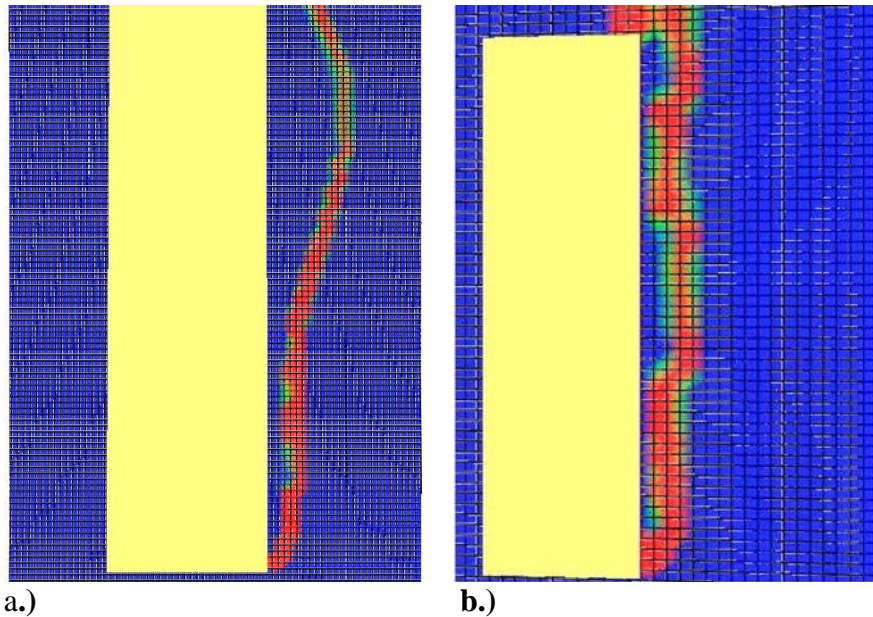


Figure 11 – Smokeview images of the simulated flame near the burning vertical PMMA surface for grid spacing of a.) 1 mm, and b.) 2 mm.

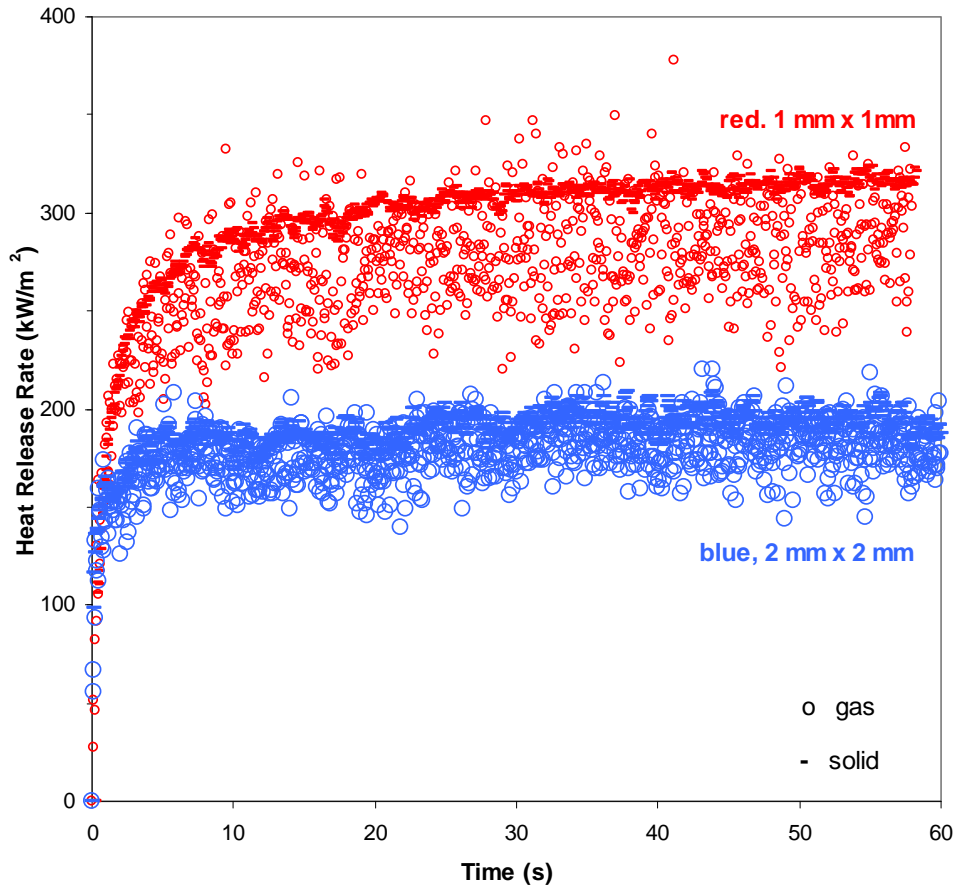


Figure 12 – Heat release rate from the gas phase (open circles) or from the solid phase (mass loss rate x heat of combustion, bars) from calculations done with 1 mm (red) or 2 mm (blue) grid spacing.

Calculation Method – DNS/LES

Two types of calculations can be performed in FDS: Large Eddy Simulation (LES) and Direct Numerical Simulation (DNS), differing in their treatment of the sub-grid-scale dynamic viscosity term of the momentum equation. Although the grid resolution is fine enough for the present calculations that there may not be much difference between the two, we ran calculations in both modes. Also, in the LES calculations, the baroclinic vorticity term in the momentum equation is typically ignored (a reasonable simplification for larger-scale calculations). For the present small-scale application, however, inclusion of baroclinic vorticity term does affect the results, and hence we performed LES calculations with and without this term. The calculated HRR (based on the mass loss rate) is shown in Figure 13 (horizontal) and Figure 14 (vertical) for calculations in DNS mode, LES mode, and LES with the baroclinic vorticity term retained. The LES case without baroclinic vorticity predicted the HRR to be a few percent higher than the DNS case, while surprisingly, the LES case with baroclinic vorticity predicted HRR 7 % and 16 % higher than DNS case for the horizontal and vertical orientations, respectively.

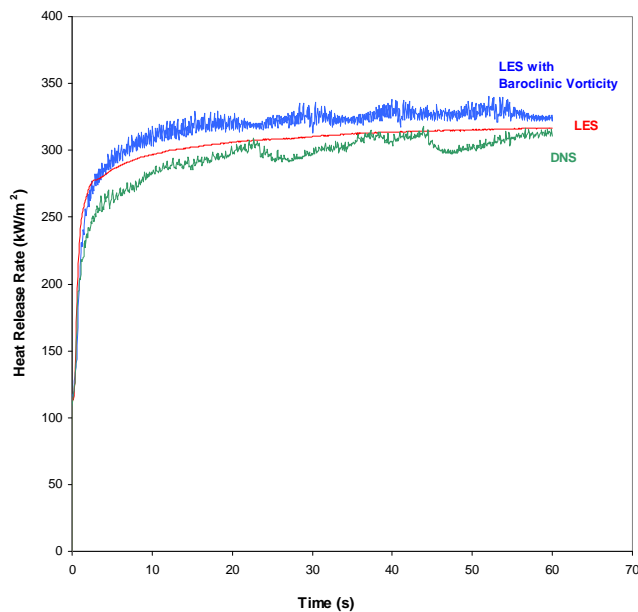


Figure 13 – Heat release rate (based on solid sample mass loss rate) for horizontal PMMA, 0 kW/m² incident flux, calculated via DNS, LES, or LES (with baroclinic vorticity).

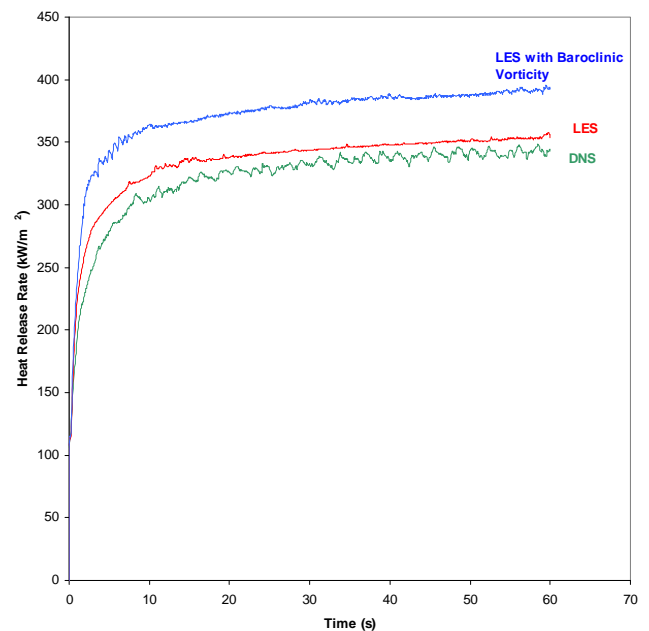


Figure 14 - Heat release rate (based on solid sample mass loss rate) for vertical PMMA, 0 kW/m² incident flux, calculated via DNS, LES, or LES (with baroclinic vorticity).

Three-dimensional Analysis

All of the previous simulations were performed using a two-dimensional analysis. FDS is also capable of performing calculations in three dimensions (with run times increased by a factor of about 100). One case for each of the horizontal and vertical sample scenarios (each

burning with zero imposed flux from the cone) was calculated in three-dimensional mode. For the horizontal sample, there is not much variation in the heat release rate as the simulation mode is changed. Therefore, the faster, two-dimensional mode appears to be sufficiently accurate. More of a difference is evident for the vertical orientation, with the two-dimensional mode predicting a 7 % lower heat release rate. This lower HRR in the 2-D mode for the vertical samples may be due to edge effects: the actual samples (as well as the 3-D calculation) show significant burning at the lateral edges of the samples which is not captured in the 2-D planar (i.e., infinite length, no edges) calculation. Since the horizontal 2-D calculation is done in the axisymmetric mode, it has a complete edge and would not experience this inaccuracy.

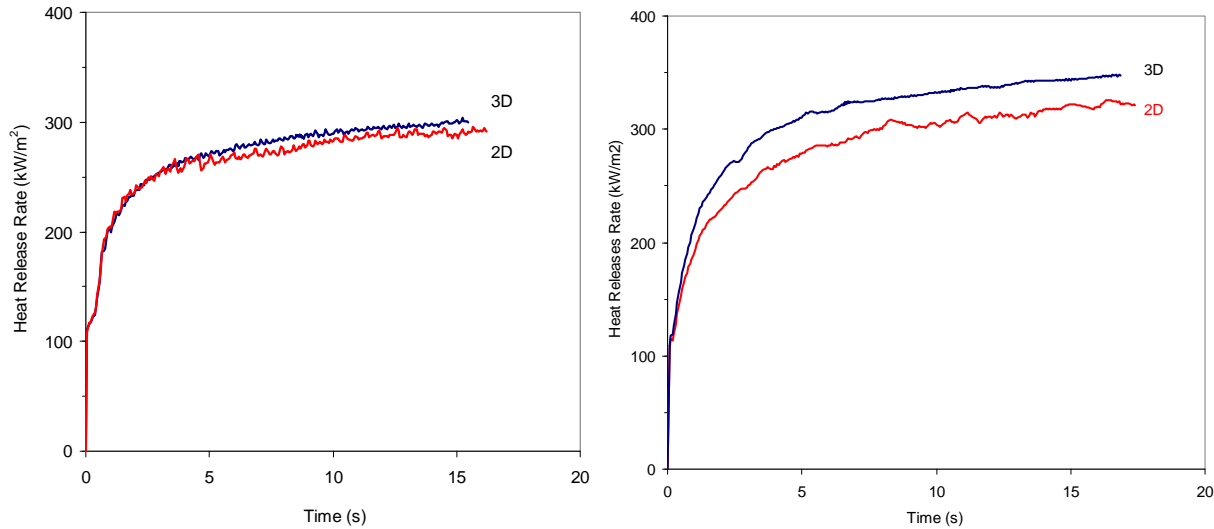


Figure 15 – Heat release rate (solid-based) from 2-D and 3-D FDS calculations, 1 mm grid spacing, original domain, horizontal (left) and vertical (right) PMMA samples, 0 kW/m² flux.

Physical Parameter Variation

The physical parameters necessary for predicting the burning rate are the specific heat, thermal conductivity, density, heat of combustion, heat of vaporization (i.e., decomposition), and kinetic parameters describing the mass loss rate as a function of temperature. In the numerical tests, we varied the heat of vaporization, the overall activation energy of the decomposition process, and the ignition temperature (i.e., the characteristic temperature at which mass loss occurs).

Heat of Vaporization

To determine the effect of the heat of vaporization in the FDS input file, calculations for a horizontal sample were run using values of 1578 kJ/kg (baseline case) and 1420 kJ/kg (10 % reduced) for this parameter. Both of these cases were run with an imposed heat flux of 0 kW/m² and 75 kW/m², as illustrated in Figure 16. A lower heat of vaporization produced a higher heat release rate. This is expected since the mass loss rate \dot{m}'' is equal to the ratio of the net heat flux

to the heat of vaporization, $\frac{\dot{q}_{net}''}{L_v}$, and the HRR is the product of the mass loss rate and the heat of combustion of PMMA. The difference between the baseline case and the 10 % lower heat of vaporization was slightly more significant in the high flux case (approximately 8%) than in the no flux case (approximately 5%). To first order, since all of the heat released goes into vaporizing the PMMA, a 10 % decrease in L_v is expected to give a 10 % increase in burning rate; however, some of the heat feedback to the sample surface also goes into conductive losses and these are a larger fraction of the total heat flux to the sample for the 0 imposed flux case. This may explain the lesser effect for the no flux case.

As shown far below in Figure 28, for horizontal PMMA, decreasing the heat of vaporization improved agreement with the experiment, especially for the higher fluxes. For the vertical cases, however, lowering the heat of vaporization 10 % may not improve the FDS prediction, since the calculated heat release rate is fairly close to the measured value at 75 kW/m², and lowering the heat of vaporization would increase the heat release rate at that flux.

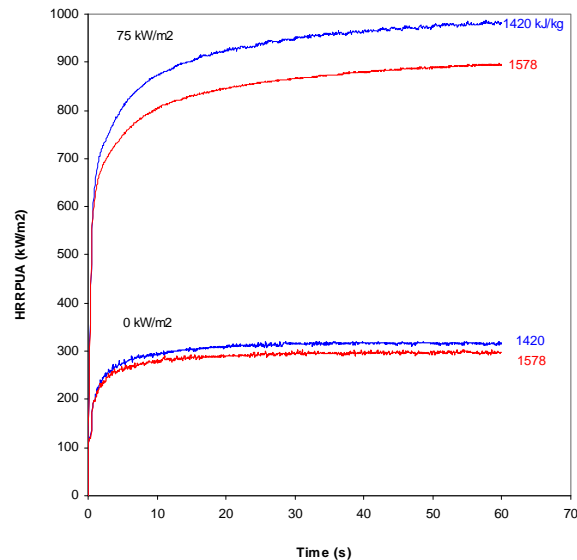


Figure 16 – Calculated heat release rate as a function of time for horizontal PMMA with imposed heat fluxes of 0 kW/m² and 75 kW/m², using the base value of the heat of vaporization (1578 kJ/kg), and a value 10 % lower (1420 kJ/kg).

Ignition Temperature

In the FDS user’s manual syntax, the “ignition temperature” basically specifies the temperature at which the sample vaporizes (like a boiling point for a liquid fuel). A higher ignition temperature decreases the heat transfer rate to the sample by convection, and increases the heat loss rate by radiation. We varied the ignition temperature of PMMA by ± 50 °C around the literature value of 330 °C, for horizontal PMMA burning with an imposed flux of (0 and 75) kW/m². For these calculations, the pre-exponential factor was set to 8.65×10^5 , at a mass flux of 0.004 kg/m²/s, and the code determined the necessary activation energy to match that

mass flux at that ignition temperature. As shown in Figure 17, a 100 °C increase in the ignition temperature gives a 10 % drop in the mass loss rate for the high-flux case, and a 15 % drop for the low flux case. The heat loss by radiation $\dot{q}_{r,loss}''$ can be estimated from the radiation heat transfer equation

$$\dot{q}_{r,loss}'' = \varepsilon\sigma(T_s^4 - T_{amb}^4)$$

which can then be compared with the net heat flux into the sample \dot{q}_{net}'' . The net heat flux \dot{q}_{net}'' can be estimated from the heat release rate \dot{q}_{rel}'' since

$$\dot{q}_{rel}'' = \dot{m}'' \Delta H_C \quad \text{and} \quad \dot{q}_{net}'' = \dot{m}'' \cdot L_v$$

in which ΔH_C is the heat of combustion and L_v is the heat of vaporization. From Figure 16, the FDS-predicted heat release rate for incident radiant fluxes of 0 kW/m² and 75 kW/m² is about 310 kW/m² and 890 kW/m², respectively, which implies a net heat input going to pyrolysis of 19 kW/m² and 56 kW/m². For surface temperatures of 280 °C and 380 °C, the predicted radiant heat loss is 5.3 kW/m² and 10.3 kW/m², or a difference of about 5 kW/m² between 280 °C and 380 °C. Hence, the 5 kW/m² higher heat losses is about the right magnitude for the high-flux case (about 10 % of the total energy going into pyrolysis), but too high (by a factor of two) for the low-flux case. That is, the lower burning rate of the low-flux case caused by a higher ignition temperature is not as low as one would expect based just on the higher radiative losses at the higher temperature. (Note that in the calculation, the outer edge of the PMMA is specified as non-burning, and is set to the same temperature as the ignition temperature, so lateral conductive losses are not the reason for the lower burning rate at the higher ignition temperature.)

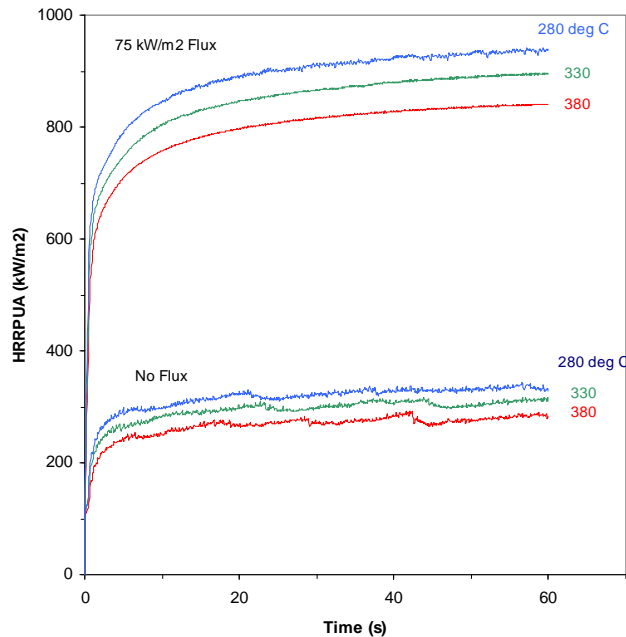


Figure 17 – Calculated variation of heat release rate with changes to the ignition temperature for horizontal PMMA at 0 kW/m² and 75 kW/m² imposed flux.

Activation Energy (E)

In order to test the sensitivity of the burning rate to the Arrhenius parameters, we specified E_A as between (20 and 50) kcal/mol, while selecting A to give the selected mass flux ($0.004 \text{ kg m}^{-2} \text{ s}^{-1}$) at the experimental value of the surface temperature ($330 \text{ }^\circ\text{C}$). The results of the calculations are shown in Figure 18, in which the heat release rate as a function of time for horizontal PMMA is shown for the two values of E_A , for the low and high imposed flux cases. Raising the activation energy from (20 to 50) kcal/mol (83 kJ/mol to 209 kJ/mol) raises the heat release rate by about 11 % for the low and high imposed flux cases. This is due mostly to changes in the surface temperature as the activation energy changes. As shown in Figure 19, raising E_A from 83 kJ/mol to 209 kJ/mol lowers the surface temperature from $380 \text{ }^\circ\text{C}$ to $350 \text{ }^\circ\text{C}$. This drop in temperature lowers the radiant heat losses from the surface by about 2 kW/m^2 , which is just about 10 % of the heat going into pyrolysis for the low-flux case, in agreement with the increase in burning rate for the higher E_A in this case. It should be noted, however, that this counter-intuitive behavior of the surface temperature (decreasing with increasing E_A) is a manifestation of the particular value used for the mass loss rate ($0.004 \text{ kg m}^{-2} \text{ s}^{-1}$) at the given surface temperature ($330 \text{ }^\circ\text{C}$). If the mass loss rates were matched at a higher value, the slope in Figure 19 would be positive and the change of heat release per unit area the opposite of that shown. The present exercise is still useful, however, for examining the magnitude of the sensitivity of the burning rate with respect to the activation energy.

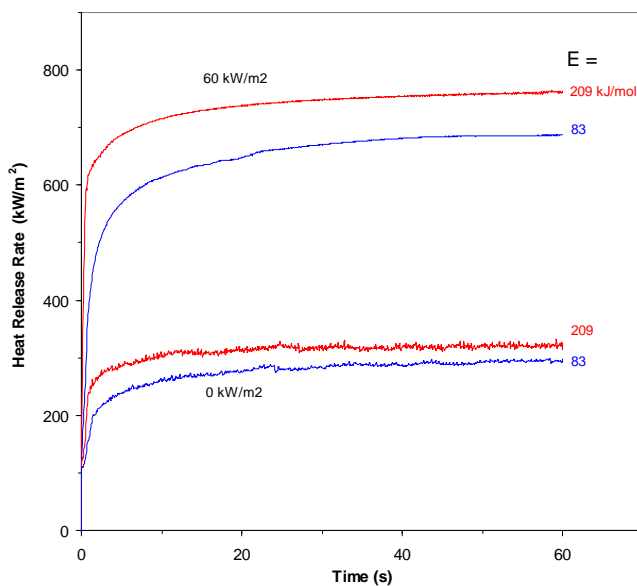


Figure 18 – Calculated heat release rate of horizontal PMMA for 0 kW/m^2 and 75 kW/m^2 imposed fluxes for values of E_A of 20 kcal/mol and 50 kcal/mol.

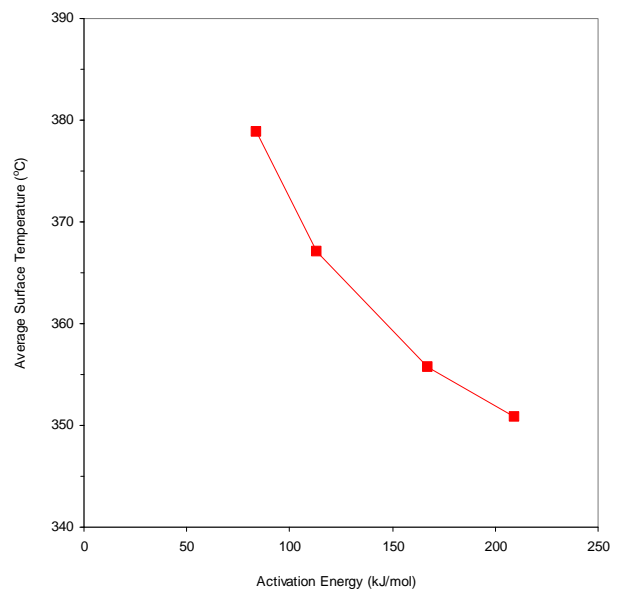


Figure 19 – Calculated variation in surface temperature resulting from different values of the activation energy.

Experimental Parameter Variation

Cone Heater Geometric Effects

FDS calculations were performed with and without the presence of a cone heater. For these calculations, the cone had no heat capacity, so the effects are only due to changes to the flow-field, and to the radiant heat feedback from the unpowered cone (as compared to radiation from the ambient). In the experiment, when the cone was positioned above the burning horizontal sample, the flame gases heated it to about 102 °C. In the simulation, its temperature was set to either 20 °C for checking the effect on the flow-field, or to 110 °C to assess changes to the radiant feedback. Figure 20 shows the heat release rate with and without a cold (20 °C) and warm (110 °C) cone present in the calculation domain. There is very little difference between the warm and cold cone, and only a 3 % difference between them and the case with the cone absent. The lack of effect of the warm vs. cold cone is consistent with the small magnitude of the radiation from the cone at these temperatures (the cone flux at 110 °C is about 5 % of the heat flux from the flame to the PMMA surface). The results for cone vs. no cone are in contrast to the experiment, for which removing the cone decreased the HRR 18 % rather than the few percent increase predicted by the calculations. For the vertical case (Figure 21), the calculations predict an 8 % increase in the burning rate with the cone removed.

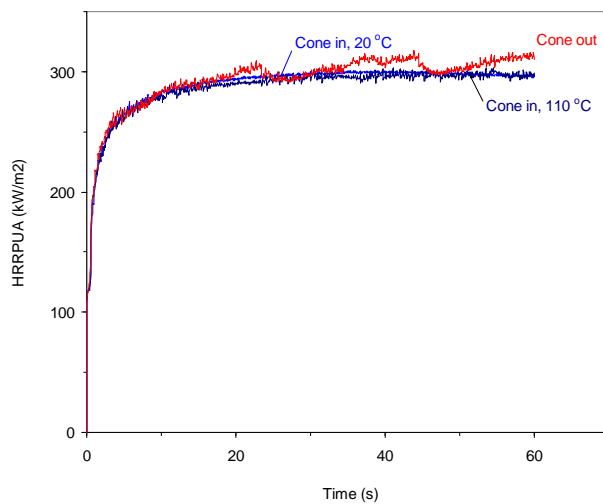


Figure 20 – Calculated heat release rate from horizontal PMMA with and without the cone heater present in the flowfield ($T_{\text{cone}}=20$ °C or 110 °C).

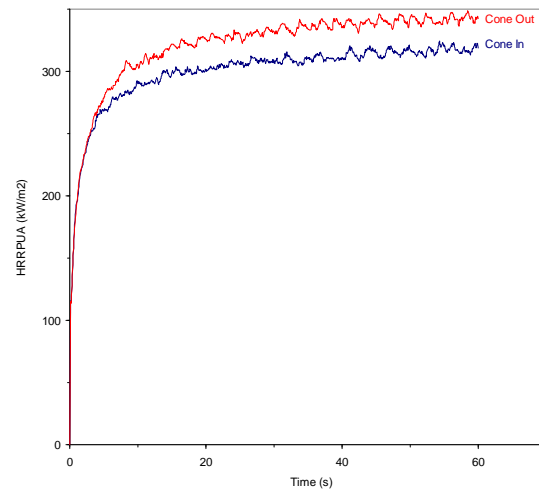


Figure 21 – Calculated heat release rate from vertical PMMA with and without the cone heater present in the flowfield ($T_{\text{cone}}=20$ °C).

Sample Backing

The code was run with and without an insulating backing on the PMMA sample. Figure 22 shows the predicted heat release of horizontal PMMA, 0 kW/m^2 imposed flux, with and without insulation. There is little difference in the calculated results (although the case with the insulation is somewhat smoother). Experiments were run for a vertical sample at 10 kW/m^2 imposed flux, with and without the insulating backing, and no measurable difference was found. The reason for the small difference between the two cases (in both the experiments and calculations) is that, due to run-time limitations, the calculation was only run for 60 s and not much of the heat would have penetrated to the backside in this time (the thermal time constant for heat conduction through the sample is between 1 h and 2 h).

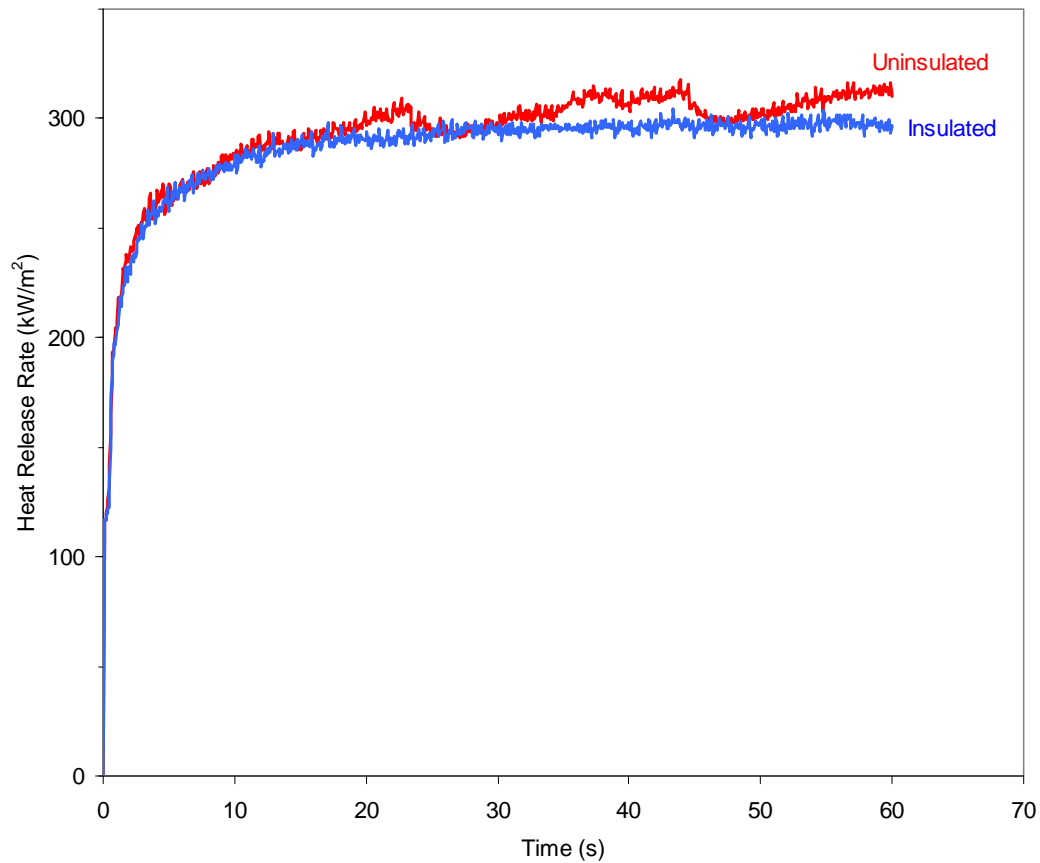


Figure 22 – Calculated heat release rate of horizontal PMMA, 0 kW/m^2 imposed flux, with and without an insulating backing on the cone sample.

Sample Edge Conditions

Edge effects in the cone sample are known to affect the burning rate [8]. In the actual cone calorimeter experiments, the PMMA sample is surrounded by a cardboard strip. As the sample burns, a “lip” of char from the cardboard builds up around the edges and is either left in place or scraped away. This scraping has a significant effect on the heat release rate of the sample, as shown in Figure 7, which indicates a 20 % higher burning rate when the lip is scrapped away. In FDS (2-dimensional mode), this was simulated by creating a thin inert lip at two and four millimeters above the sample surface and giving it a constant temperature equal to the ignition temperature of the PMMA (330 °C). The results (Figure 23) show that 2 mm and 4 mm lips reduce the burning rate by 25 % and 40 %. This is consistent with the size of the lip formed during the experiment, and the magnitude of the increase in burning rate after removing the lip (as shown in Figure 7).

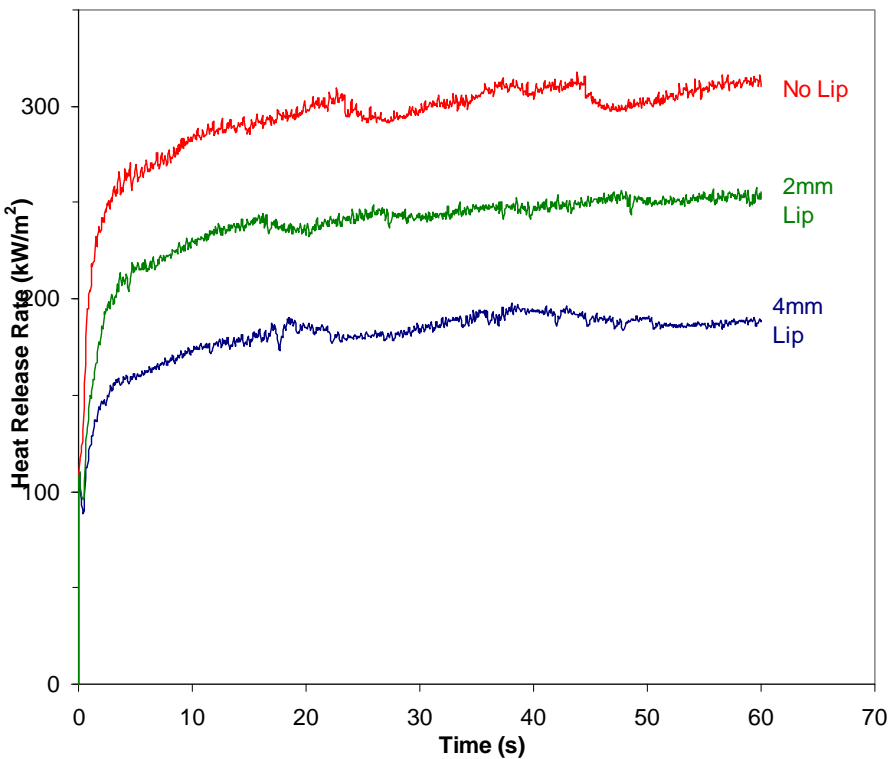


Figure 23 – Heat release rate of horizontal PMMA, 0 kW/m² imposed flux, with varying lip size at the top edge of the sample perimeter.

Exhaust Fan

In the actual cone calorimeter experiments, a vent in the hood above the cone apparatus produces an exhaust velocity. The airflow through this vent is approximately 24 L/s [5], which results in a velocity at the hood entrance of 15 cm/s. For the purposes of this simulation, a vent with this velocity was created along the entire upper physical domain boundary. As seen in Figure 24, the effect of this vent on the heat release rate was small.

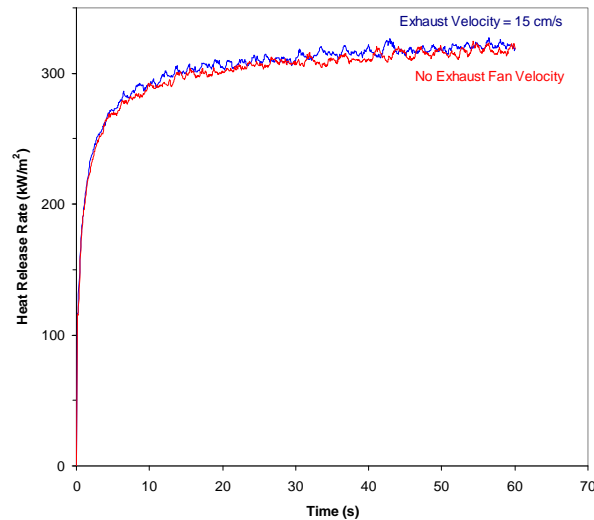


Figure 24 – Heat release rate of horizontal PMMA, 0 kW/m² imposed flux, with and without a 15 cm/s imposed exit velocity on the top boundary of the calculation.

External Heat Flux

The major parameter varied in both the experiments and the calculations was the imposed radiant flux on the PMMA sample. In the experiments, this was achieved by adjusting the cone temperature until a calibrated Schmidt-Boelter heat flux gage indicated the desired heat flux (tests were run at 0, 5, 10, 25, 50, and 75 kW/m²). Similarly, in the calculations, the specified cone temperature was selected such that it provided the desired flux on the sample. The heat flux resulting from the cone temperature for the calculated vertical and horizontal cases, as well as the experimental horizontal case, is shown in Figure 25. The difference between the vertical and horizontal cases in FDS is probably due to the different view factors for the 2-D planar and 2-D axi-symmetric configurations of the calculations. Similarly, the ~100 K difference between the required cone temperature in the experiment and in the calculation (for the horizontal case) may be due to differences in the geometry.

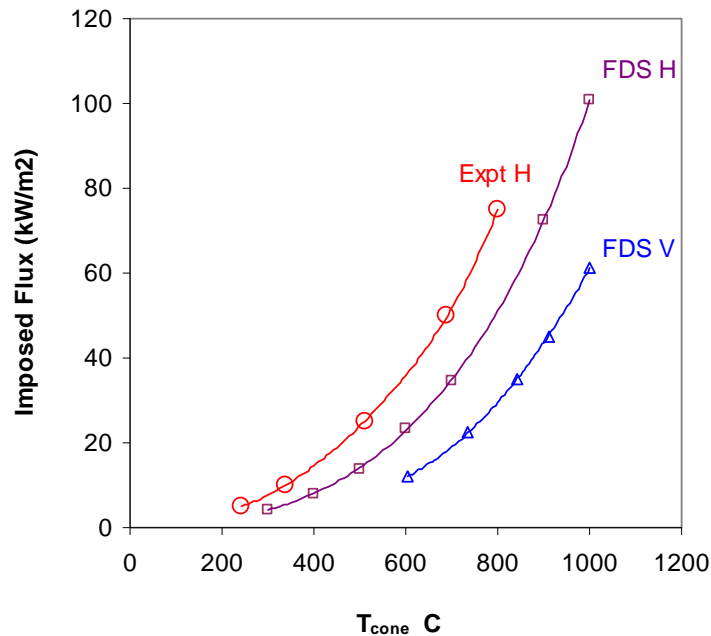


Figure 25 – Heater temperature required to produce a given incident flux on the PMMA sample in the FDS calculations for vertical V and horizontal H samples, and for the experiment with a horizontal sample.

Figure 26 shows the heat release rate from horizontal PMMA in the cone as a function of imposed heat flux from the cone; the experimental data are shown by the points, and the FDS predicted HRR is shown by the solid line. Similar results for the vertical PMMA are shown in Figure 27. A somewhat surprising result is that the horizontal and vertical cases provide essentially the same burning rate for the vertical and horizontal cases (c.f. the red points in Figure 26 and Figure 27), even down to 0 kW/m² imposed flux. FDS is able to predict the burning rate reasonably for both cases, although the increase in HRR with imposed flux (i.e., the slope of the line in the figures) is less in the calculations than in the experiment. The slope of this line can be modified by changing the heat of vaporization for PMMA in the FDS input file, as shown in Figure 28; however, this would make the agreement for the vertical case worse. For both orientations, the poorest agreement occurs for case of 0 kW/m² imposed flux. Reasons for this are described later in this manuscript.

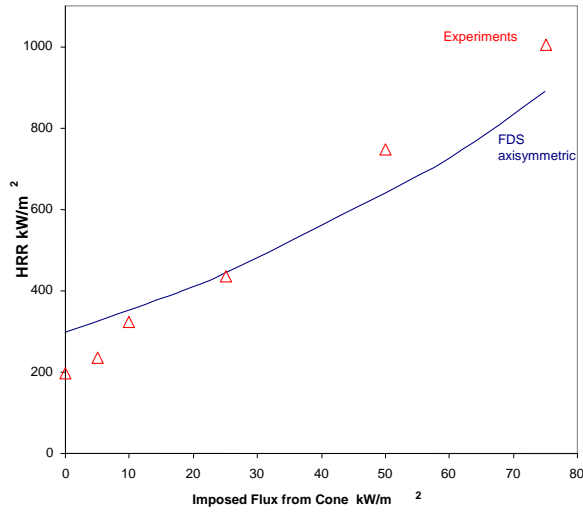


Figure 26 – Heat release rate as a function of imposed heat flux from the cone; horizontal PMMA sample.

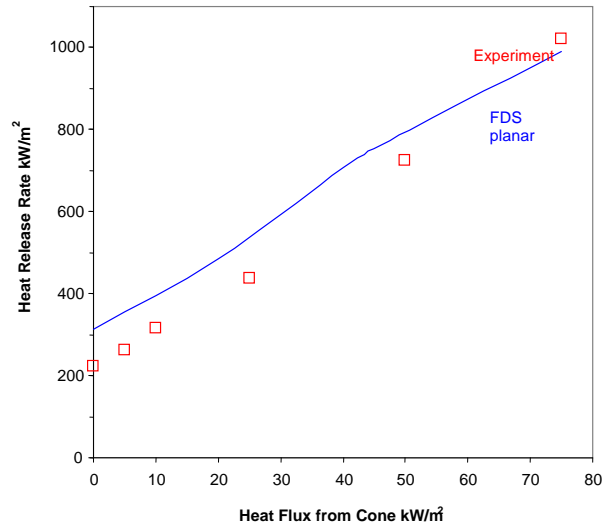


Figure 27 - Heat release rate as a function of imposed heat flux from the cone; vertical PMMA sample.

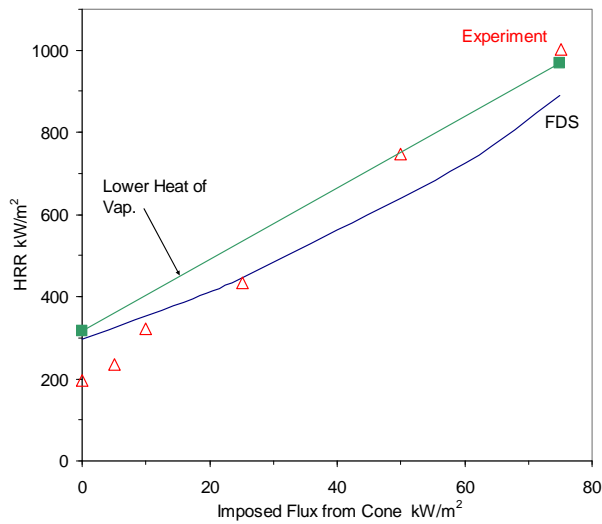


Figure 28 – Heat release rate of horizontal PMMA as a function of imposed heat flux with a 10 % lower value for heat of vaporization of PMMA, plotted with the original results for heat release rate (horizontal PMMA, Figure 26).

Inverted Geometry Case

Olson et al. [6] have recently described a system for producing low-strain flames over solid samples exposed to radiant fluxes that may be useful for predicting the behavior of flames in microgravity. The system basically uses an inverted cone calorimeter, and hence, their data provide us with an additional configuration (inverted) for testing FDS predictions of burning of PMMA in the cone. We ran simulations of their configuration corresponding to imposed radiant fluxes of (0, 10, and 25) kW/m², for imposed vertical velocities of (10, 69, and 200) cm/s, which correspond to strain rates of (4.2, 10, and 27) s⁻¹.

Figure 29, Figure 30, and Figure 31 present images of the FDS simulation of the cone and flame in the inverted configuration. The input files of our calculations were modified to include the flow-directing skirt around the sample and to provide an imposed flow up the center of the cone. In addition, the calculations were performed in the 2-D planar mode to avoid numerical instabilities that can occur near the r=0 axis for calculations in axial symmetry.

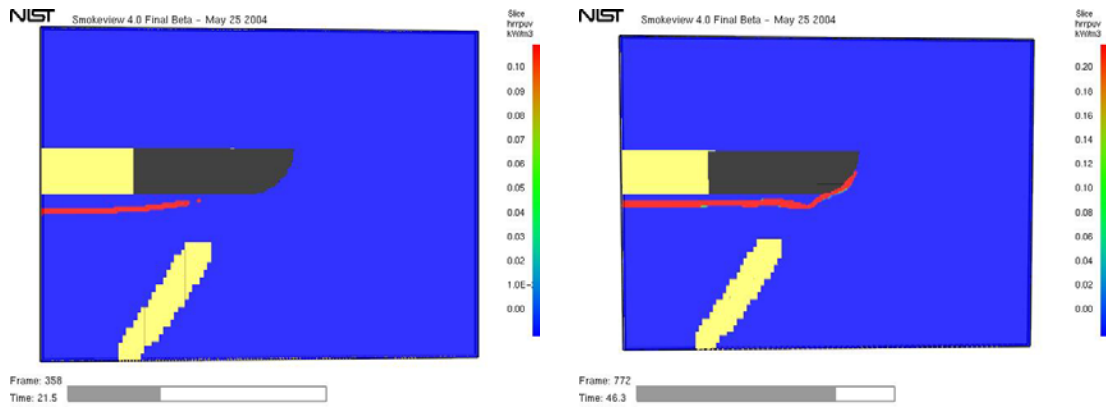


Figure 29 - Smokeview images of the PMMA sample, flame, and cone, 0 kW/m² imposed Flux (left, 10 cm/s; right, 69 cm/s inlet velocity).

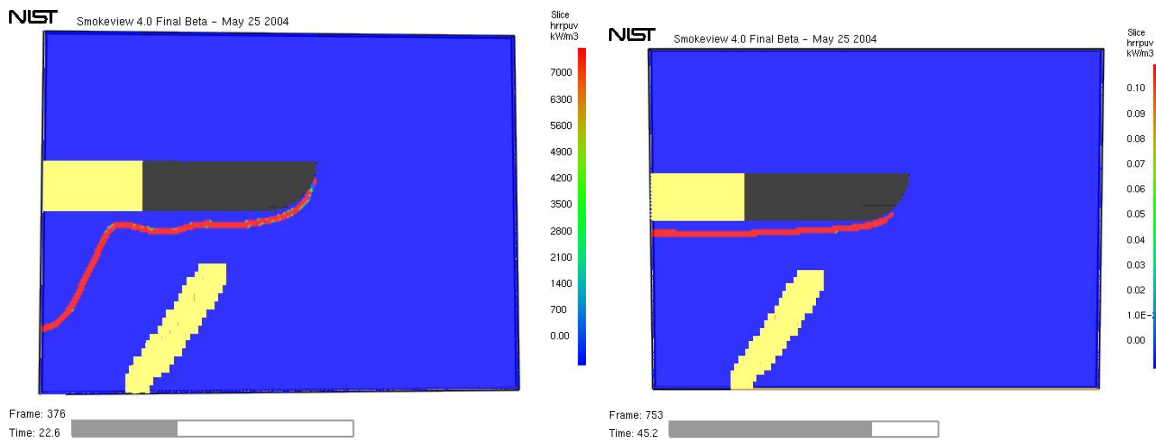


Figure 30 - Smokeview images of the PMMA sample, flame, and cone, 10 kW/m² imposed Flux (left, 10 cm/s; right, 69 cm/s inlet velocity).

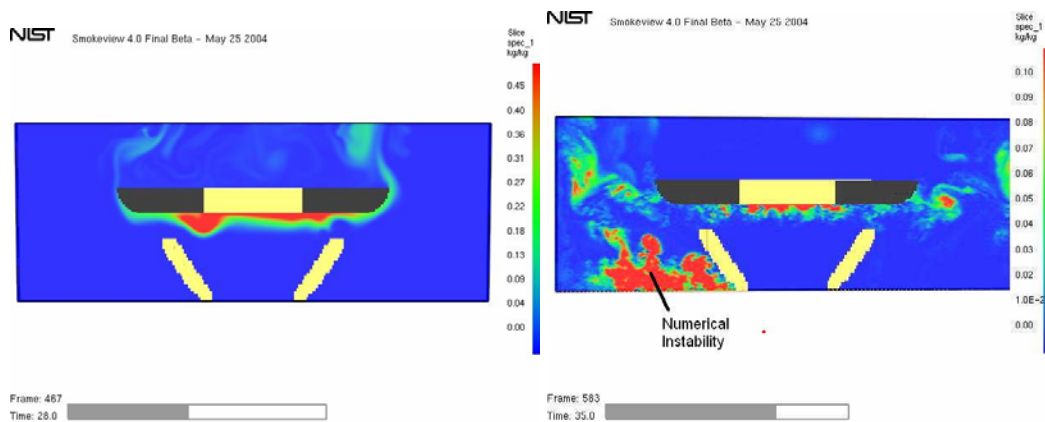


Figure 31 - Smokeview images of the PMMA sample, flame, and cone, 25 kW/m² imposed Flux (left, 10 cm/s; right, 200 cm/s inlet velocity).

Figure 32 shows the data of Olsen et al. together with FDS predictions. Unfortunately, most of the data are problematic. Except for the lowest strain 4.2 s^{-1} , all of the calculations had numerical instabilities. Of the three low-strain calculations, those at (0 and 10) kW/m^2 imposed flux did not have numerical instabilities, but burned only for a few seconds and then extinguished, and hence were not in good agreement with the experiment. The other low-strain case (strain of 4.2 s^{-1} and an imposed flux of 25 kW/m^2) had good agreement with the experimental data. We are continuing the investigations to try to eliminate the numerical instabilities (which may be due to the large imposed axial flow velocities, 69 cm/s and 200 cm/s , of those conditions).

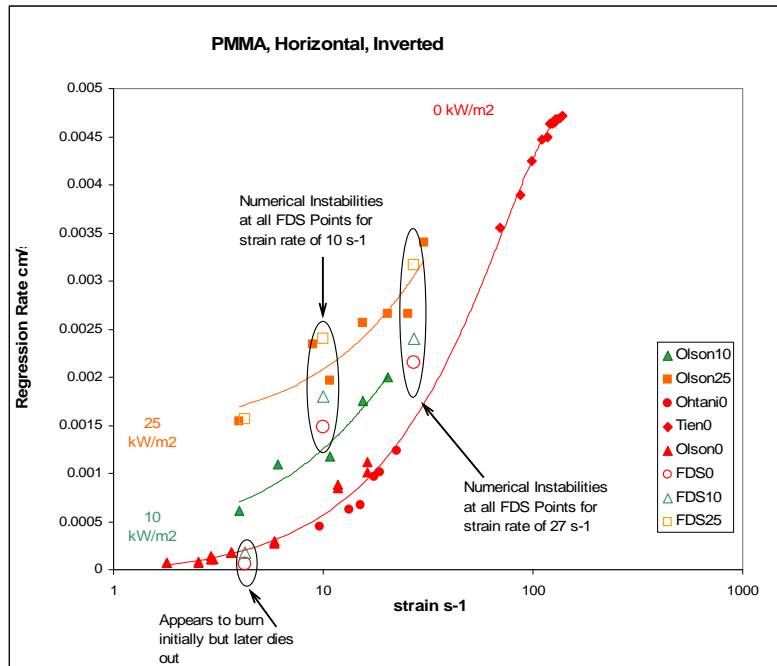
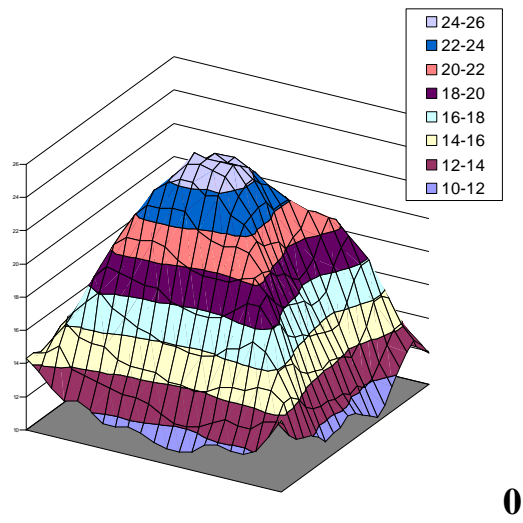


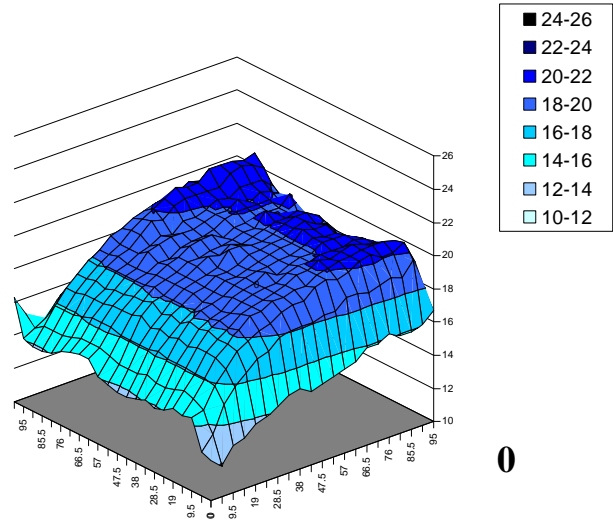
Figure 32 – Experimental data reported in [6] for clear PMMA burning at varying strains (4 s^{-1} to 27 s^{-1}) and with imposed radiant fluxes of (0, 10, and 25) kW/m^2 . Also shown are the results of FDS predictions.

Surface Mass Loss Variation

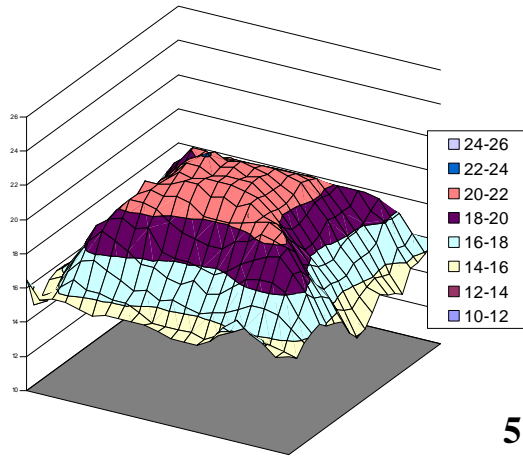
As described above, the non-uniform PMMA samples obtained at the conclusion of each burn provide the opportunity to estimate the burning rate variations over the surface of the samples. The surface topography of the PMMA samples was determined with an automated system, and select results are presented in Figure 33. As shown, the higher fluxes lead to greater fuel



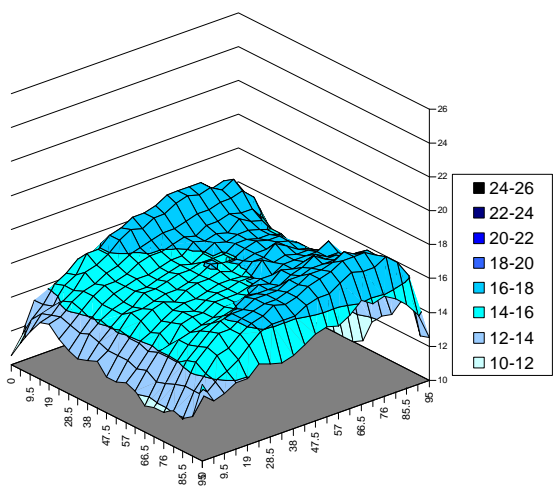
0



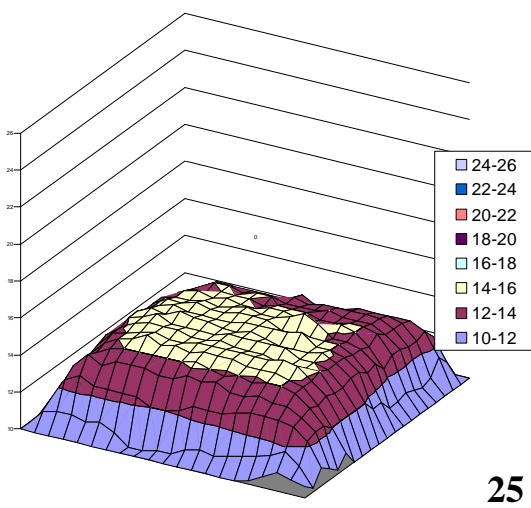
0



5



10



25

Figure 33 – Topography of remaining PMMA sample for horizontal (left) samples exposed to (0, 5, and 25) kW/m² for (1560, 1053, and 924) s; and vertical samples at (0 and 10) kW/m² exposed for (825 and 813) s (note: the vertical axis goes from 10 to 25 mm).

consumption and a more uniform burning over the surface of the sample (the heat transfer at higher imposed flux is dominated by the thermal radiation from the cone, which is close to uniform). The vertical samples also burned more uniformly.

The FDS prediction and the experimental result for the surface topography (0 kW/m^2 imposed flux) are shown for the horizontal and vertical orientations in Figure 34 and Figure 35. Since the numerical simulations for the 3-D calculations only ran for about 30 s or less, it was necessary to extrapolate these results for longer burn times to produce a sample topography similar to the experimental results (which had burn times of hundreds of seconds). To do this, we first determined the average burning rate over the surface of the sample for the last second of the calculation (15 s to 16 s for these cases, see Figure 15). Then, the burning time for the simulation was selected to give the same final mass of the experiments. With this integration time, the mass loss at each location on the surface was calculated based on the surface variation of the mass loss rate predicted by the 3-D calculation. This approach was used since: 1.) the calculation time for the 3-D simulation was very long, and we could not achieve the actual burning times in the time available for the calculations, and 2.) the FDS results for the average steady-state burning rate at 0 kW/m^2 flux was about 80 % too high (see Figure 26 and Figure 27 at 0 kW/m^2), so using actual burning times would not give the proper total mass loss. While not quantitative, the approach used (selecting the burn time in the calculations to match the experimental mass loss) allows us to assess the overall ability of FDS to predict the distribution of surface erosion. As shown, the trends are correct, although for the calculation, the burning of the middle of the horizontal sample is too large and the gradient at the edges is too steep. For the vertical sample, the gradient of the mass loss rate at the edges is again much more gradual in the experiment as compared to the model. Nonetheless, there is a limit to the agreement between calculation and experiment in these cases since FDS does not allow changes to the sample geometry during burning. Hence, local changes to the heat transfer coefficient caused by changes to the shape of the sample, which would occur in the experiment but not in the calculation, may be responsible for the discrepancies observed here.

An alternative way to view these data is to make contour maps, for example, of the burning rate variation over the sample surface. The numerical and experimental results for the 0 kW/m^2 imposed flux for the horizontal and vertical orientations are shown in Figure 36 and Figure 37. It is interesting to note that for the horizontal case, there is very little burning in the center of the horizontal sample (in either the calculation or the experiment), as opposed to the vertical sample, for which burning occurs everywhere. In both orientations, the burning is much greater at the edges (although the calculations over-predict this effect).

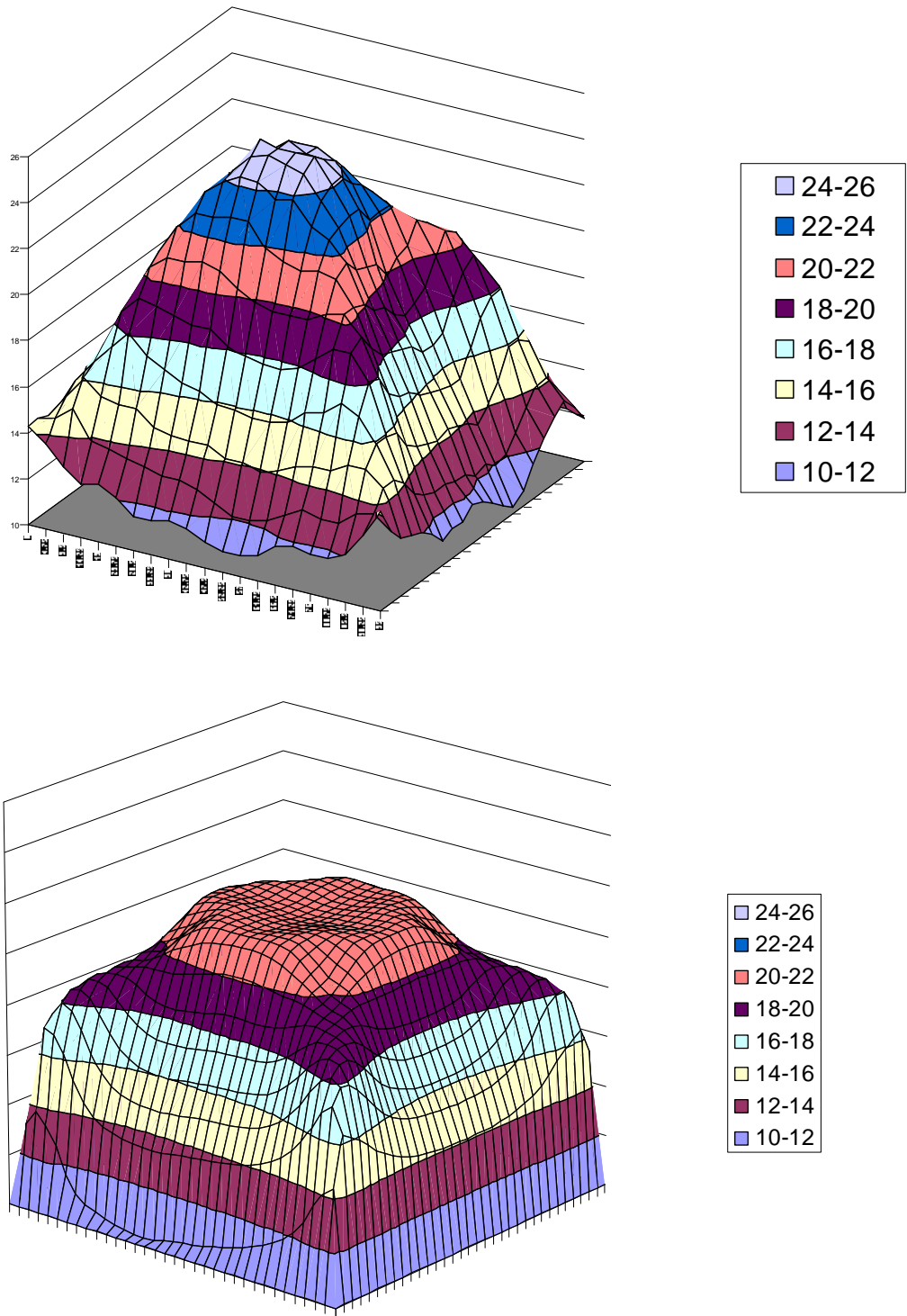


Figure 34 – Experimental (top) and 3-D FDS predicted surface topography of horizontal PMMA at 0 kW/m² imposed flux. The experiment ran for 1560 s, and the simulation, 819 s.

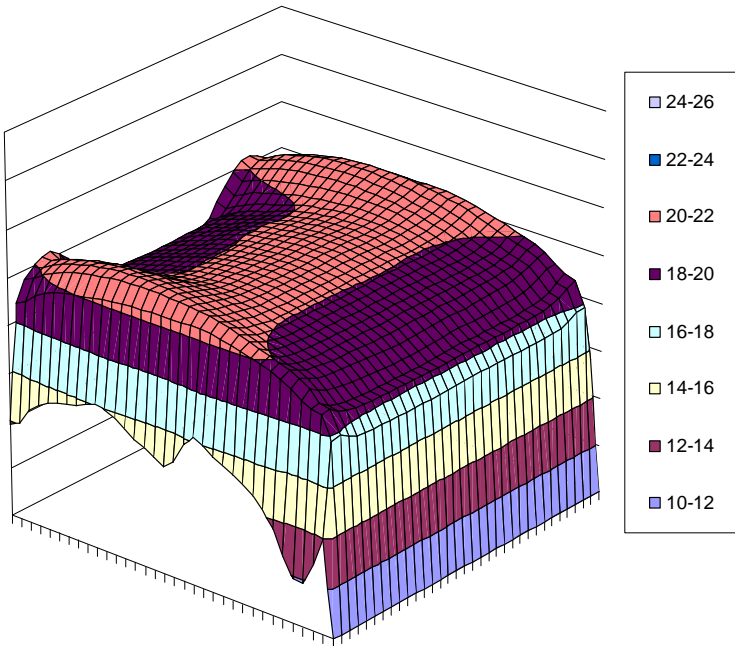
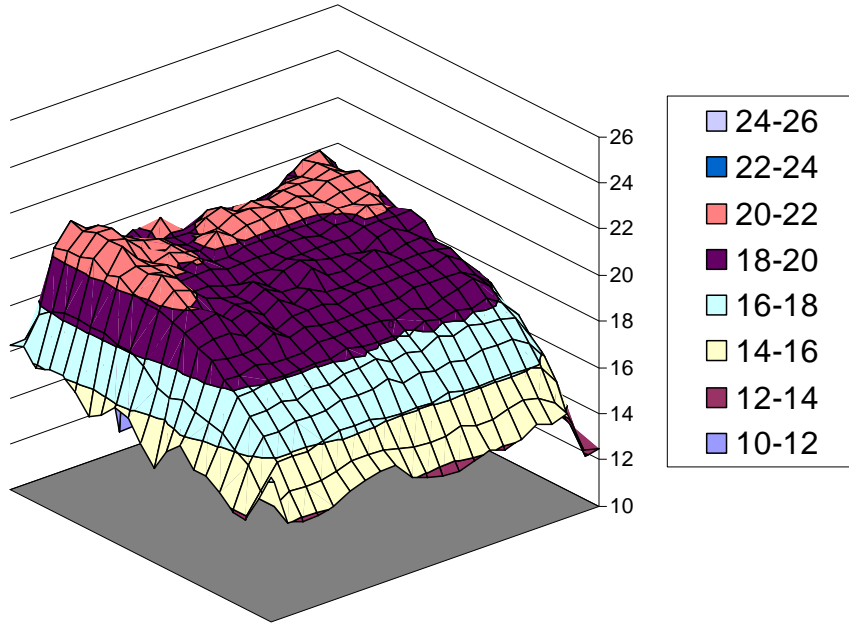


Figure 35 - Experimental (top) and 3-D FDS predicted surface topography of vertical PMMA at 0 kW/m² imposed flux. The experiment ran for 825 s, and the simulation, 485 s.

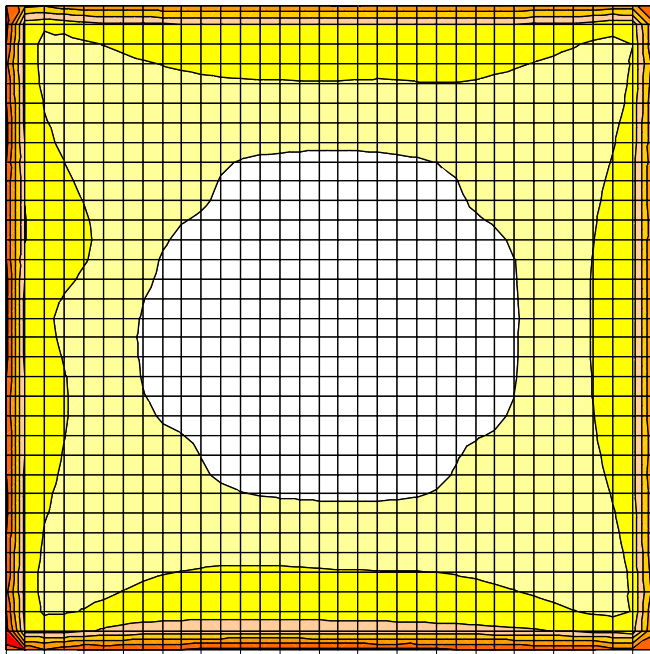
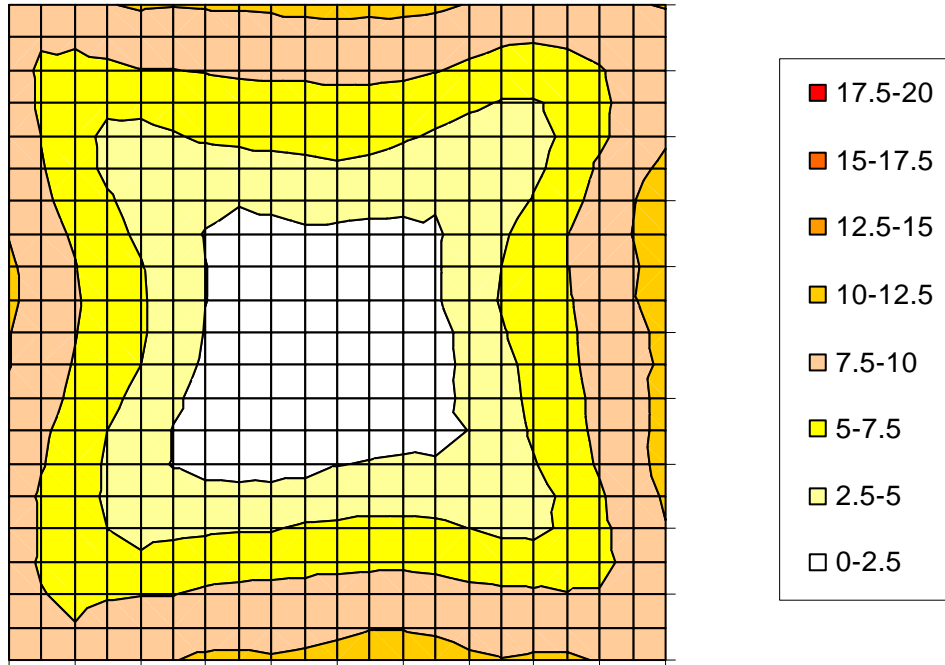


Figure 36 – Experimental (top) and FDS predicted (bottom) surface variation of mass loss rate ($\text{g}/\text{m}^2/\text{s}$) for horizontal burning PMMA with $0 \text{ kW}/\text{m}^2$ imposed flux (top view of $10 \text{ cm} \times 10 \text{ cm}$ sample).

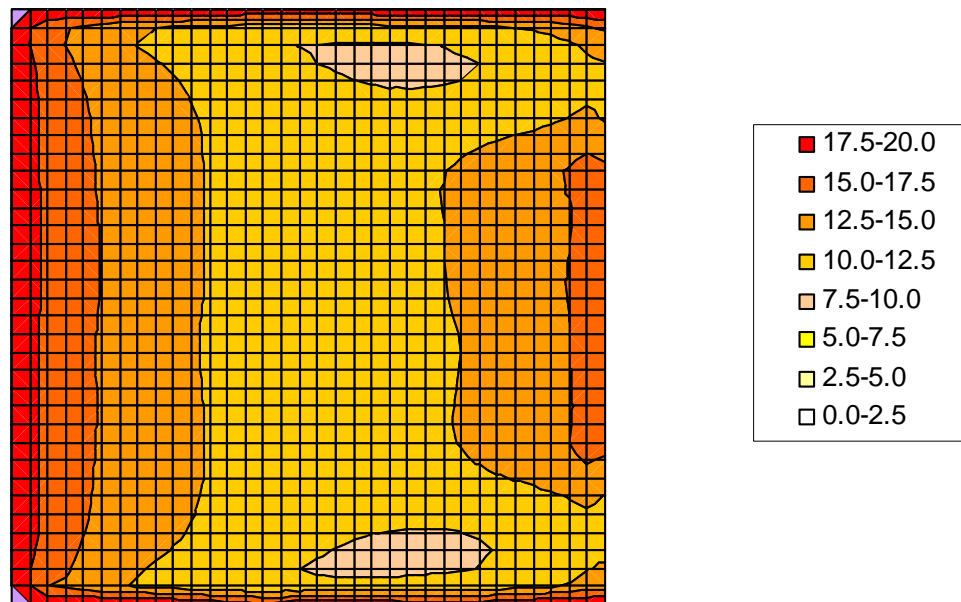
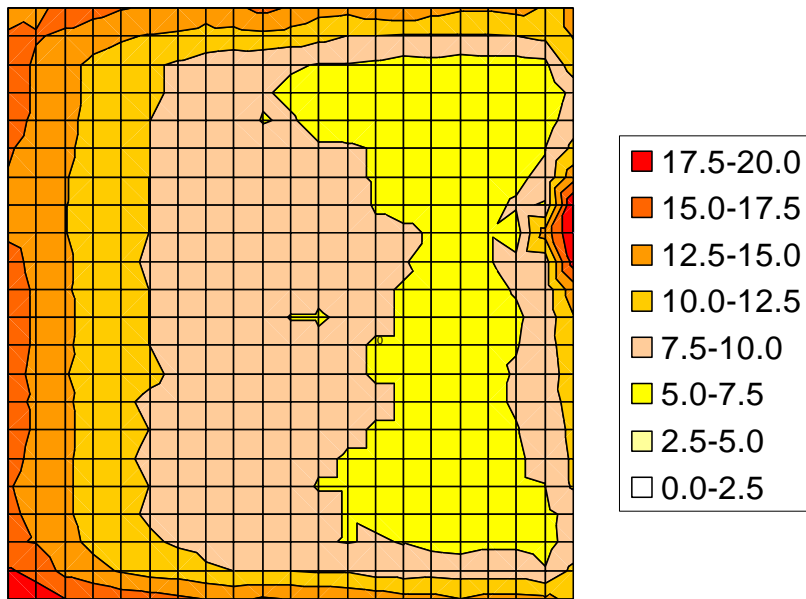


Figure 37 - Experimental (top) and FDS predicted (bottom) surface variation of mass loss rate ($\text{g/m}^2/\text{s}$) for vertical burning PMMA with 0 kW/m^2 imposed flux (top view of $10 \text{ cm} \times 10 \text{ cm}$ sample)..

Conclusions

FDS was used to simulate the burning of black PMMA samples in the cone calorimeter. Various parameters were found to have a large effect on either the experimental or calculated burning rates, and must be carefully controlled in the experiment or modeling. In the calculations, numerical parameters, physical, and experimental parameters were varied.

Numerical Parameters:

1. The domain size and grid resolution were both found to have a large effect, especially on the heat release rate in the gas phase.
2. The selection of DNS or LES mode did not make much difference for the present calculations (with 1 mm grid size).
3. The 2-D simulation (axisymmetric) was within a few percent of the 3-D calculation for horizontal samples, while the 2-D planar simulation for the vertical samples was about 7 % lower than the 3-D simulation.

Physical Parameters:

1. Heat of vaporization, ignition temperature, and activation energy of the decomposition step all had a significant effect (about 10 %) on the burning rate over a range of variation of their values which may be observed in practice.

Experimental Parameters:

1. The presence or absence of the cone (with 0 kW/m² flux) above the horizontal sample was important in the experiment, but not important in the calculations.
2. The presence of the exhaust flow in the hood above the cone was not important in the calculations.
3. The presence of insulation on the back side of the sample was not important in either.
4. The presence of a lip on the sample edge was important in both the experiments and calculations, with a 4 mm lip changing the burning rate by almost a factor of two.
5. The variation in the average sample burning rate with changes to the imposed flux (over the range of 0 kW/m² to 75 kW/m²) was predicted reasonably well by the simulations; however, as the imposed flux went down, the simulation overpredicted the average mass loss rate as compared to the experiment
6. For the 0 kW/m² imposed flux case, most of the heat flux from the flame to the sample occurs at the edges; however, the code over-predicts heat flux both in the center and at the edges.

The reasons for this over-prediction of the burning rate with no imposed flux are related to the fidelity with which the phenomena were set up in the numerical description. In the center, the heat flux is mainly by radiation, and the calculation was greatly simplified. Only gray-body radiation from an assumed soot volume fraction was included, and this may be in error. Gas-phase species were not included, and in particular, absorption of the IR radiation by the pyrolyzed but unburned MMA monomer is known to have an effect. Treatment of the

edge condition may need to be improved, and the changes to the sample geometry during burning (not included in FDS) could affect the result. As the imposed heat flux from the cone increases, it dominates the heat flux to the sample, so these flame radiation and edge heat transfer effects are not so important (although possible absorption of the radiation by the MMA monomer, or its decomposition products, could still be important).

There exist significant problems with the inverted geometry for all values of the imposed flow and imposed radiation. Further work is needed to circumvent the numerical instabilities, and to determine the reasons for the non-burning behavior for the low-flow, low-flux cases.

In future work, it would be useful to look at the time dependence of all of the results generated in the present work, since only the steady-state results were analyzed in the present discussion. Further, it would be of interest to study more complex solid fuels, for which the present capabilities of FDS for treating the solid phase would clearly need to be upgraded. Nonetheless, the present results provide a valuable foundation for understanding how the myriad experimental and numerical parameters which can be manipulated in the tests and the analyses affect the accuracy of the comparisons between calculations and experiment.

Acknowledgements

The authors are indebted to Dr. Richard Lyon of the FAA Technical Center for his initial calculations and experiments which motivated this work. Mr. Randy Shields conducted the experiments and made significant contributions to the experimental approaches. Mr. Ian Rafferty wrote the software and developed the PMMA surface topography analysis system. Helpful conversations with Dr. William (Ruddy) Mell concerning PMMA modeling are gratefully acknowledged.

References

1. McGrattan, K. B. and Forney, G. P., *Fire Dynamics Simulator (Version 4): User's Guide*, NISTSP 1019, 2004.
2. McGrattan, K. B., *Fire Dynamics Simulator (Version 4) Technical Reference Guide.*, NISTSP 1018, 2004.
3. Forney, G. P. and McGrattan, K. B., *User's Guide for Smokeview Version 4 - A Tool for Visualizing Fire Dynamics Simulation Data*, NISTSP 1017, 2004.
4. Kashiwagi, T., *Proc. Combust. Inst.* 25:1423 (1994).
5. Twilley, W. H. and Babrauskas, V., *User's Guide for the Cone Calorimeter*, SP-745, 1988.
6. Olson, S.L., Beeson, H.D., Hass, J.P., and Baas, J.S., *Proc. Combust. Inst.* 30:to appear (2004).
7. Tewarson, A., *Experimental Evaluation of Flammability Parameters of Polymeric Materials*, FMRC J.I. 1A6R1.RC, 1979.
8. Babrauskas, V., Twilley, W.H., and Parker, W.J., *Fire and Materials* 17:51 (1993-1994).

Scale Model Flames for Determining the Heat Release Rate from Burning Polymers¹

Gregory T. Linteris^a, Ian Rafferty^b

^a *Building and Fire Research Laboratory, National Institute of Standards and Technology, Gaithersburg, MD 20899, USA*

^b *Department of Physics, Saint Mary's College of Maryland, Saint Mary's City, MD 20686 USA*

Abstract

The utility of flame size for the assessment of the heat release rate of burning polymers has been studied. Six polymers were tested in the NIST cone calorimeter to determine their heat release rate, and their flame height, area, and volume. A reduced-scale burner was developed for producing non-flickering, laminar flames, and tests were conducted with four gases, three liquids, and three polymers; subsequent automated image analyses again determined the flame size. The scaling for the flame size was shown to be reasonably well described by Froude modeling for turbulent pool fires or by laminar jet diffusion flame theory.

INTRODUCTION

The heat release rate of a burning object is important for quantifying fire growth and spread in a building [1]. To estimate the heat release rate of full-scale objects, small-scale samples of representative materials are subjected to controlled radiant heat fluxes, and the heat release is measured. Various methods have been developed to measure the heat release rate of the reduced scale samples [2][3], and they are accurate and effective, but unfortunately require expensive equipment and are relatively time consuming (0.5 h to 2 h per sample). If a less expensive, faster test method could be developed, heat release rate measurements might be more widely used by the polymer industry in their development of materials with lower flammability; such a method could also be used in high-throughput testing, allowing combinatorial techniques to be applied to the development of fire-safe materials.

The present paper investigates the potential of measurements of flame size as a surrogate for heat release [4]. As a first step, various polymer samples were burned in the NIST cone calorimeter and their heat release rate was determined. Simultaneously, the flame images were captured and then analyzed to determine the flame height, area, and volume. An image analysis procedure was developed which allowed flame size determinations from a large number of frames using an automated image analysis program with various filtering techniques. In the second set of tests, a new burner was designed which would limit the flames to the laminar regime. To achieve non-flickering, laminar flames, this burner used smaller samples, provided a co-flow of oxidizer, and the geometry was controlled. Flames of solid, liquid, and gaseous fuels were produced, and the heat release rate was determined from the measured fuel consumption rate and the calculated heat of combustion. This paper describes the scaling relationships observed for the flame height, surface area, and volume with respect to the heat release, and discusses the utility of these for estimating the heat release.

BACKGROUND

Our search for a correlation between flame size and heat release is motivated in part by the observation by Orloff and de Ris [5] that turbulent pool fires have an approximately constant heat release rate per unit volume of the flame, \dot{Q}_c''' (1200 kW/m³). The scaling laws for pool burners have been investigated by

¹ Linteris G.T., Rafferty I.P. "Scale Model Flames for Determining the Heat Release Rate from Burning Polymers." in Progress in Scale Modeling, Ed. K. Saito. Tokyo, 2008, pp. 235-245.

many researchers, and good reviews exist [6-8]. While these investigations have been most interested in turbulent flames typical of fires, they can also be applied to the present results obtained in the cone calorimeter. For the reduced-scale flames, however, it is more appropriate to use laminar flame theory, for which descriptions appear in the literature [9,10,10]. Although all of these mathematical descriptions employ significant simplifications, they are expected to provide useful scaling relationships for correlating and interpreting the present data.

EXPERIMENT

Two distinct sets of experiments were conducted. In the first, the NIST cone calorimeter [11] was used as the test bed for the burning polymer samples. This apparatus consists of a cone-shaped electric resistive heating element (hence the name), which provides radiant fluxes up to 100 kW/m² on a polymeric sample of dimensions typically 7.5 cm to 10 cm diameter. In addition to other parameters, the exhaust is tested for mass flow, and volume fraction of oxygen (CO volume fraction measurements were not available for the present experiments). From these, the heat release rate of the burning sample is estimated using oxygen consumption calorimetry (which is based on the approximation that the heat release is proportional to the mass of oxygen consumed, times a constant of 13.1 kJ/g [12]). In the present experiments, the cone heater was off, and the sample decomposition was due entirely to the heat provided by the flame radiation and convection to the sample surface.

A second experimental apparatus was specifically developed to reduce the transition to turbulent flow. For solid samples, a smaller sample was used (2.5 cm diameter, 2.5 cm tall), and it was positioned concentrically in a laminar co-flowing oxidizer stream of controlled velocity (16.7 cm/s). The configuration was a variant of the cup burner [13], and has been used previously in tests of halon replacements for suppressing solid-sample flames [14]. The gas and liquid fuels were tested in a separate cup burner, that has been described previously [15]. It consists of a cylindrical glass cup (28 mm diameter) positioned inside a glass chimney (53.3 cm tall, 9.5 cm diameter); glass beads and screens provide flow straightening for the fuel and oxidizer flows. For the liquid and gaseous fuels, the chimney was cut off at a point lower than the burner rim to avoid reflections from the flame image. Gas flows were measured by mass flow controllers (Sierra 860²) which were calibrated so that their uncertainty is 2 % of indicated flow. For liquid fuels, syringe pumps (Yale Apparatus model YA-12) supplied the fuel at a known rate, which was manually adjusted to keep the fuel level flush with the edge of the cup rim. For the solid fuels, the mass consumption rate was determined with a laboratory scale (Mettler, PE-360). The syringe pump or the scale output was recorded with a computer.

The fuels used were methane (Matheson UHP, 99.9%), propane (Matheson CP, 99%), ethylene, propylene (Matheson, CP), methanol (Aldrich, 99.8 %), ethanol (Warner Graham), heptane (Mallinckrodt), trioxane (Aldrich, 99+%), and various commercially available polymers, including poly(methyl methacrylate) PMMA, polypropylene, paraffin, ethylene vinyl acetate (EVA), Nylon-12, and high density polyethylene (HDPE). The air was house compressed air (filtered and dried) which is additionally cleaned by passing it through an 0.01 μm filter, a carbon filter, and a desiccant bed to remove small aerosols, organic vapors, and water vapor.

The flame images for all tests were recorded with a digital color video camera (Sony, TRV-730) having a pixel resolution of 720 x 480 and framing rate of 30 Hz. The flame images were analyzed to determine the flame height, area, and volume using an automated image analysis system based on two software packages. The NASA image processing freeware program Spotlight 1.1 provided the flame outline from the color image (for PMMA and Nylon-12 in the cone, it was necessary to determine the flame outline manually, and a single, representative image was used). A custom-written code subsequently interpreted the outline and calculated the flame surface area and volume. In determining the

² Certain commercial equipment, instruments, or materials are identified in this paper to adequately specify the procedure. Such identification does not imply recommendation or endorsement by NIST, nor does it imply that the materials or equipment are necessarily the best available for the intended use.

flame outline, no attempt was made to distinguish between the yellow soot emission and the blue emission from radicals in the reaction zone; both delineated the presence of a flame. The various filtering options in Spotlight were adjusted for each flame sequence so that the determined flame outline matched the visual luminous flame location.

For the small, non-flickering, laminar flames, estimation of the flame height and area from the flame outline was straightforward, obtained by measuring the flame tip location and cord width, and assuming axial symmetry, summing segments as described below. For the convoluted flames in the cone calorimeter, however, we used the method described by Orloff [16], in which the vertical flame is divided up into slices (determined by the vertical pixel resolution). Across each slice, the software determines the presence or absence of the flame, assumes that any segment of the cord containing the flame is a cylindrical disk, and sums the volume or area for each segment of the vertical slice. The total surface area or volume of the flame is the sum for all vertical slices. Using this approach for complicated turbulent flame shapes, Orloff was able to produce flame *locations* within about 5 % of those obtained from integration of the flame presence probability density function. Hence, we estimate that at the 95 % confidence level, the luminous flame area or volume for the cone flames are within about 10 %. For the small laminar flames which have very regular shapes, this uncertainty is less than 1 %. Note that in many of the figures which follow, if the uncertainty is shown on the data points, the error bars represent the standard deviation (66 % confidence level) for the variation in the flame area for the 30 frames of data. This uncertainty is much larger than that due to the flame area determination techniques described above.

An uncertainty analysis was performed, consisting of calculation of individual uncertainty components and root mean square summation of components. All uncertainties are reported as *expanded uncertainties*: $X \pm ku_c$, from a combined standard uncertainty (estimated standard deviation) u_c , and a coverage factor $k = 2$. Likewise, when reported, the relative uncertainty is ku_c/X . The expanded relative uncertainties for the theoretical heat release for the gaseous and liquid fuel flames are 4 % and 2 %. For the solid fuels, the theoretical heat release, determined from the mass loss rate and heat of combustion, varies according to how constant the heat of combustion is for that polymer. For PMMA, paraffin, and trioxane, the uncertainty is estimated to be 4%; for polypropylene, it is 10 %.

RESULTS

Fig. 1(a-c) show the measured flame height (a.), area (b.), and volume (c.) for the six polymers tested in the cone calorimeter; the dotted lines are linear least-squares fits to the data. The closed symbols are used for the samples for which automated image analysis could be performed (EVA, HDPE, PP, and trioxane), while the open symbols are used for Nylon-12 and PMMA, for which image analysis was performed manually. For data points determined automatically, each point shown is the average from 30 flame images, and the error bar is +/- one standard deviation. As indicated, the standard deviation is around 18 %, 29 %, and 15 % for the height, area, and volume, respectively, for the flames in the cone. While there is significant scatter in the points representing the averaged data, the height, area, and volume of the flame are clearly correlated with the measured heat release.

Although the cone calorimeter would appear to be a good test apparatus for comparing the flame size with the heat release, several features make it less than optimum. Geometrical factors influence the flame shape; for example, the sample holder support is not optimized for smooth flow, causing the exhaust-induced air flow to be highly irregular and disturbing the flame. Also, the edge of the typical sample holder can trip the flow to turbulent flow [16,17], changing the flame size-heat release rate relationship. The typical sample size creates flames which are in-between laminar and turbulent flow, making them hard to describe analytically, and causing the oxygen transport rate to the flame to vary. If the conical heater element is being used, it can obstruct the view for tall flames. Finally, the flame images are highly irregular, making the determination of the flame area difficult. As a result, we conducted tests in the reduced-scale burner described above as the cup burner.

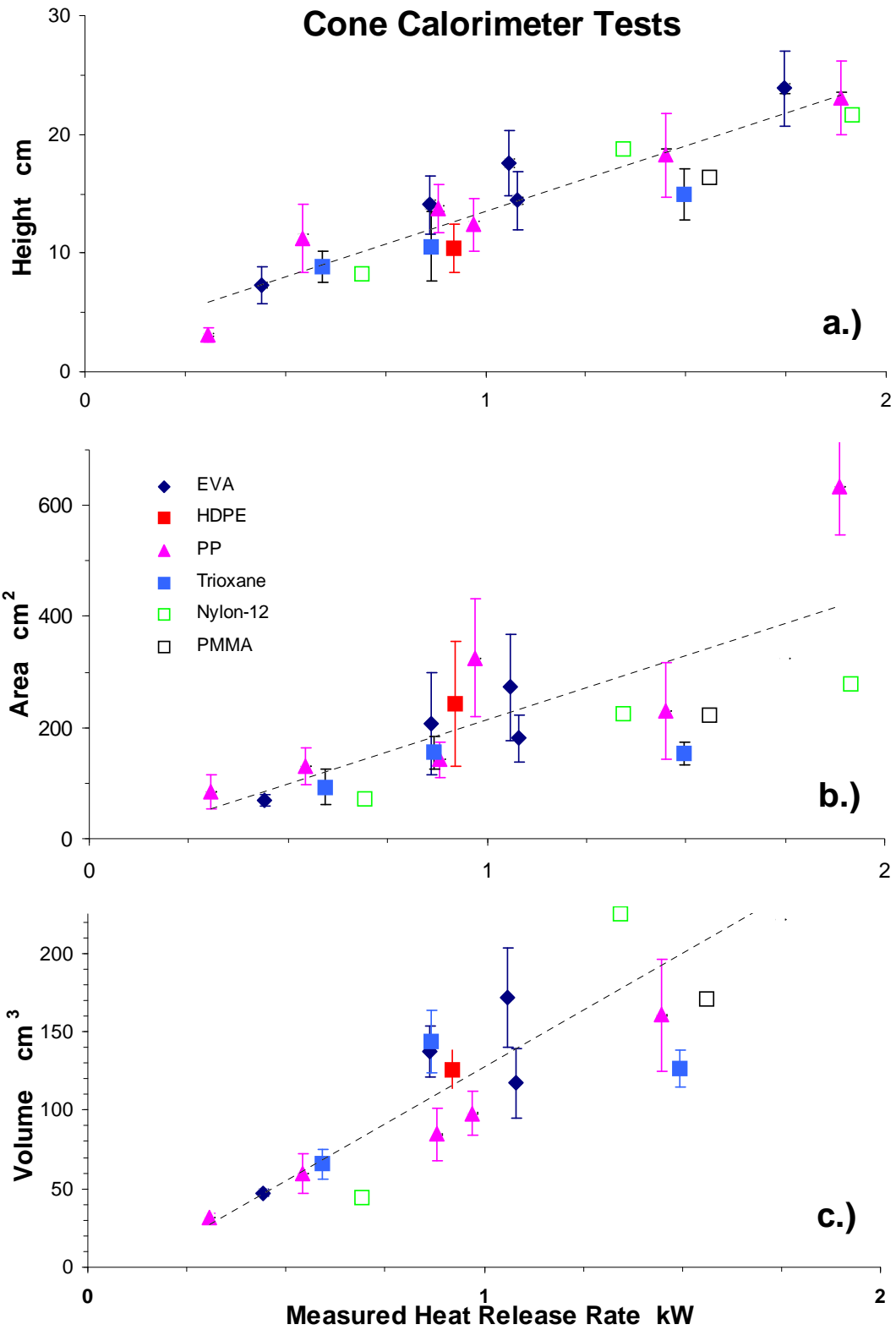


Fig. 1. Measured flame height (a.), area (b.), and volume (c.), as a function of heat release rate for polymers tested in the cone calorimeter. Open symbols denote manual image analysis; closed, automated; dotted lines are linear curve fits to the data.

For the cup-burner flames, the theoretical heat release of the flames was calculated from the measured fuel input rate and the heat of combustion of the gaseous reactants. An implicit assumption in the present work is that the combustion efficiency is high (>97 %). The polymers selected for the tests were those with relatively constant and known heats of combustion. Since we are interested in the oxygen demand of the gas-phase reactants, the heat of combustion used was for gas-phase reactants to gas-phase products. Fig. 2(a-c) shows the flame height, area, and volume as functions of the theoretical heat release. (Note that the heptane point is scaled by 1/2 for both variables to put it on the same plot without expanding the scales.) It is clear from the figure that the gaseous flames (square symbols) have the least variation between images, and their flame height, area, and volume are very well correlated with the predicted heat release. The reduced-scale, cup burner produces flames which have little variation between images, typically 3 %, 6 %, and 10 %, for the gaseous, liquid, and solid fuels, respectively, regardless of whether height, area, or volume.

For turbulent diffusion flames above pool fires, Zukoski [6] outlines various theoretical scaling relationships which have been developed based on Froude modeling. These typically are power-law functions of the form $Z_f/D \sim Q^{*n}$, in which Z_f is the flame height (normalized by the burner diameter D), and Q^* is the non-dimensional square root of the Froude number expressed in terms of the heat release $Q^* = \dot{Q}_c / (\rho_\infty C_p T_\infty (gD)^{1/2} D^2)$, in which \dot{Q}_c is the heat release in the flame, ρ_∞ , C_p , T_∞ , are the density, specific heat, and temperature of the oxidizer, and g is the acceleration due to gravity. Fig. 3 shows the normalized flame height Z_f/D as a function of Q^* for the gaseous, liquid, and solid fuels in the reduced-scale cup burner (solid symbols) as well as for the solid fuels in the cone calorimeter (open symbols). Also shown are the power law relations for Z_f/D suggested by Zukoski [6], each applicable in a range of Q^* , with a $Q^{*2/5}$ dependence for $Q^* > 1$, $Q^{*2/3}$ for $0.15 < Q^* < 1$, and Q^{*2} for $Q^* < 0.15$. The dotted black line is a linear curve fit to the data in the reduced-scale cup burner. The present data, from either burner, are clearly in the transition regime.

The laminar flame theory of Roper [10] for co-flow jet diffusion flames can also be used to predict the flame height in the reduced-scale cup burner flames. The calculated flame height from Roper's correlation is shown in Fig. 3. as the dotted red line, which indicates a Z_f/D variation with Q^{*1} , which is consistent with the curve fit through the reduced-scale cup burner data which also gives a Q^{*1} dependence. (The offset of the Roper prediction with the curve fit through the data is likely due to the wide burner used in the present flame, which gives a non-zero flame area at zero height).

Our ultimate goal in the present work is to relate the measured heat release to the measured flame size (height, area, or volume). Simple scale arguments of the type suggested by de Ris and Orloff [5] can be used to determine the predicted and actual scaling relationship between the heat release and the height, area, or volume. To do this, it is useful to plot the heat release normalized by the flame height, area, or volume, as a function of the heat release, as done in Fig. 4. From the power-law fits to the data, it is possible to extract the relationship between the heat release rate normalized by the height \dot{Q}'_c , area \dot{Q}''_c , or volume \dot{Q}'''_c , and the heat release rate. From these, we can then estimate the power-law relationship correlating the heat release with the height, area, or volume; e.g. $\dot{Q}_c \sim Z_f^{n_f}$, $\dot{Q}_c \sim A_f^{n_a}$, or $\dot{Q}_c \sim V_f^{n_v}$. Table 1 lists the power-law scaling coefficients n_f , n_a , n_v , for the heat release based on the measured flame height, area, or volume as observed in either the cone or the reduced-scale cup-burner flames; values are also given for the laminar flame theory prediction of Roper [10], as well as the turbulent flame theory predictions from Froude modeling as outlined by Zukoski [6]. As shown, the experimental results for the cone calorimeter flames are midway between the theoretical results for turbulent flames in the $0.15 < Q^* < 1$ and $Q^* > 1$ regimes. For the flames in the reduced-scale cup burner, the results are midway between the theoretical prediction of Roper for laminar jet flames, and the Froude modeling turbulent flames in the $0.15 < Q^* < 1$ regime.

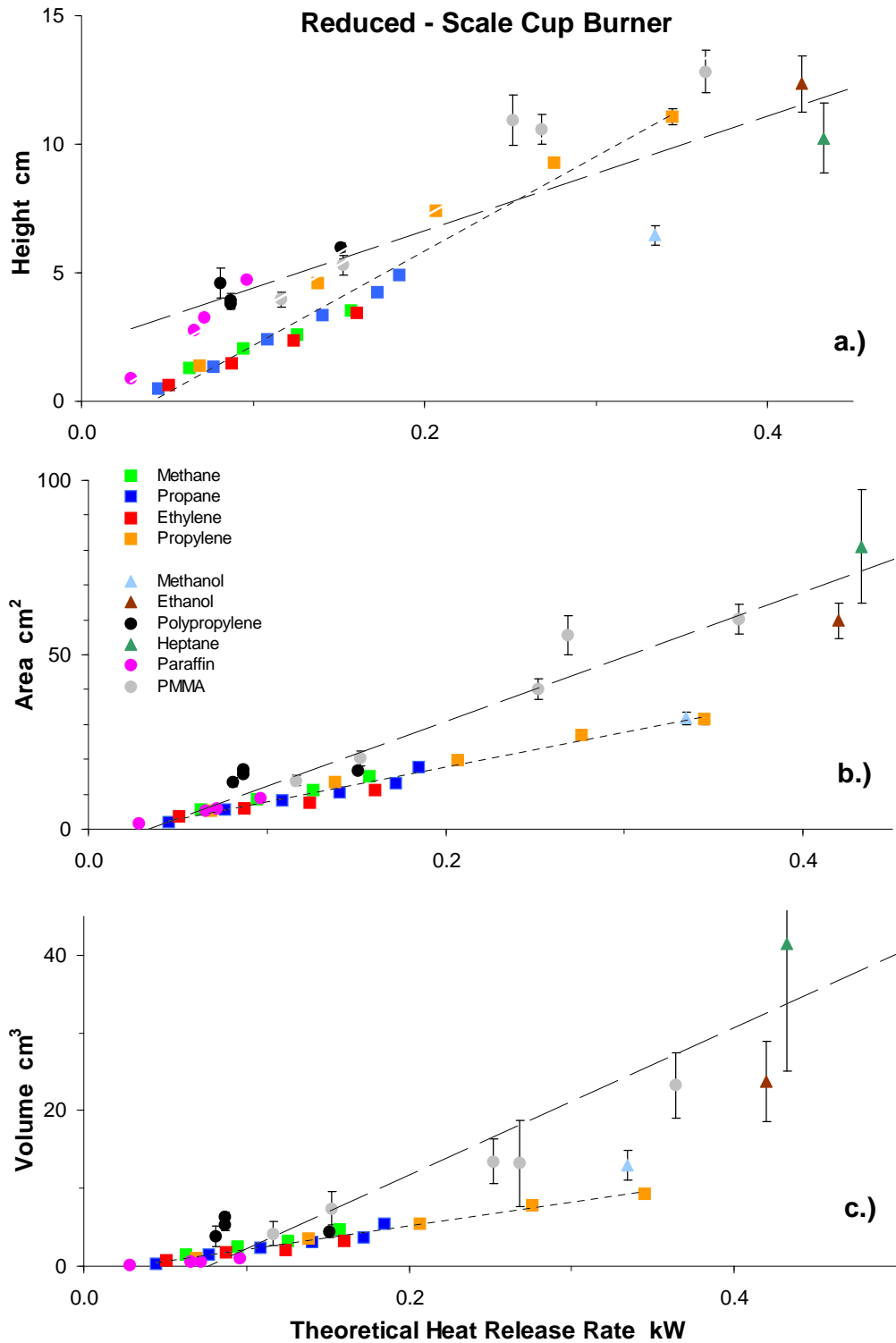


Fig. 2. Measured flame height (a.), area (b.), and volume (c.), as a function of heat release rate for solid, liquid, and gaseous fuels tested in the reduced-scale cup burner (both heptane parameters on all plots scaled by 2). Dotted lines are linear curve fits to the gaseous fuel data; dashed, to the solid and liquid fuels data.

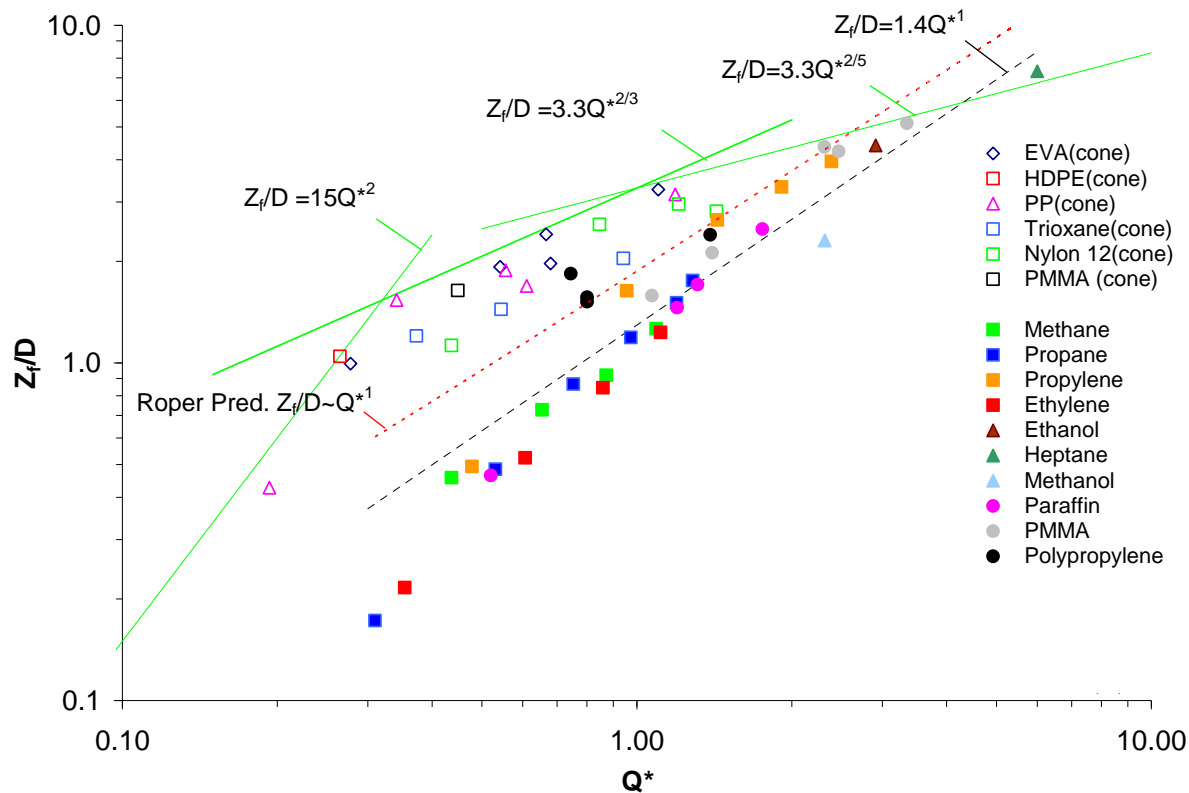


Fig. 3. Normalized flame height Z_f/D as a function of Q^* (cone calorimeter data, open symbols; reduced-scale cup burner, filled symbols).

Two additional features of the flames were observed to be important for the data analysis. First, the image recording and analysis used the visible image, which includes both the blue emission from flame radicals in the reaction zone, as well as the much stronger black body emission from soot particles. We observed the luminous flame shapes to be larger than the blue reaction zone flame shapes; other researchers have found the luminous shapes to be 10 % to 60 % larger [18,19]. Second, as the sample size gets smaller, the physical effects which may contribute to flame retardancy, for example, barrier layers on the burning polymer, can be affected by the small size.

CONCLUSIONS

Experiments have been performed to measure the heat release rate as well as the flame height, area, and volume of burning gaseous, liquid, and solid fuels. Flames from samples in the NIST cone calorimeter had relatively high variability in these measured parameters from image to image, and were reasonably well described by Froude modeling predictions for turbulent pool flames, but in a regime where viscous effects are starting to be important. A reduced-scale burner similar to the cup burner produced flames with much lower scatter and image to image variation. The variation of the height of these flames with heat release was well-predicted by the theoretical model of Roper. The small laminar flames showed scaling behavior of the heat release with respect to the height, area, and volume, midway between that of laminar co-flow jet diffusion flames and turbulent pool flames in the transition regime. Further research is necessary to determine if these measured parameters (flame height, area, and volume) can be determined accurately enough to be useful for predicting the heat release rate, especially for a wider range of test materials with actual heat release data based on oxygen consumption calorimetry.

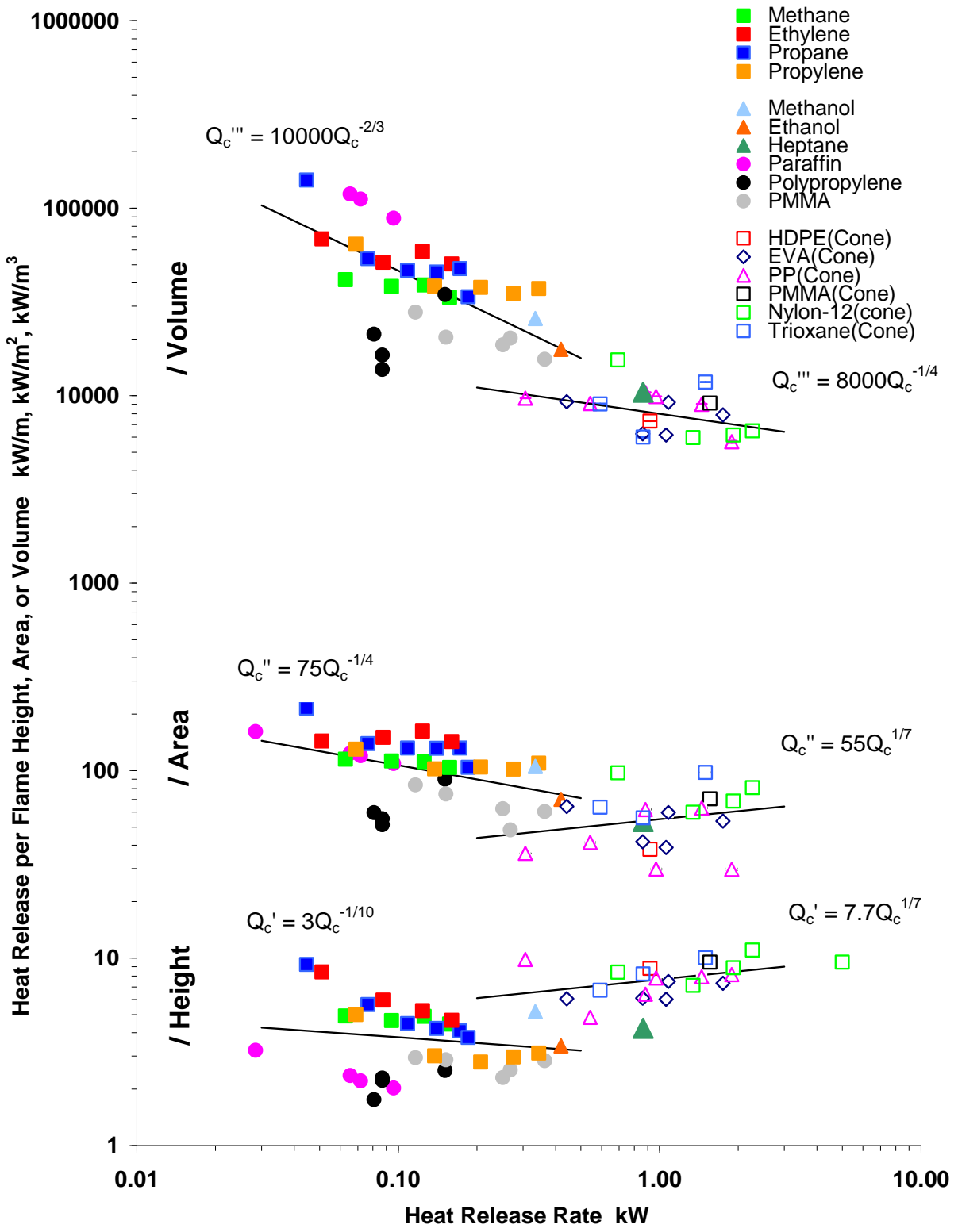


Fig. 4. Heat release normalized by the measured flame height, area, or volume as a function of the heat release rate for flames in the reduced scale cup burner (solid symbols) and the cone calorimeter (open symbols); the lines are the results of a power-law curve fit to the data, together with the equation.

TABLE 1

Power-law scaling coefficient for the heat release from the measured flame height, area, or volume, as observed in either the cone or the reduced-scale cup-burner flames, as well as that predicted by theory.

Scaling Relationship	Power Law Scaling Coefficient, n_i				
	Observed		Theory		
	Cup Burner	Cone	Laminar Flame, Roper [10]	Froude Modeling [6] $0.15 < Q^* < 1$	$1 < Q^*$
$\dot{Q}_c \sim Z_f^{n_z}; n_z =$	0.91	1.2	1.0	1.5	2.5
$\dot{Q}_c \sim A_f^{n_a}; n_a =$	0.8	1.2	0.5	0.75	1.25
$\dot{Q}_c \sim V_f^{n_v}; n_v =$	0.4	0.8	0.25	0.5	0.83

ACKNOWLEDGEMENTS

Helpful conversations with David Urban, Peter Sunderland, and Jiann Yang added greatly to this work. This research was supported by NIST and NASA's Office of Biological and Physical Research.

References

- [1] V. Babrauskas, R.D. Peacock, *Fire Safety J.* 18 (3) (1992) 255-272.
- [2] B.A.L. Ostman, I.G. Svensson, J. Blomqvist, *Fire Mater.* 9 (4) (1985) 176-184.
- [3] A. Tewarson, *Flammability of polymers and organic liquids, Part I, Burning intensity*, FMRC Serial 22429, Factory Mutual Research Corp., Norwood, MA, 1975.
- [4] Lyon, R., FAA, Personal Communication, 2003.
- [5] L. Orloff, J. de Ris, *Proc. Combust. Inst.* 19 (1982) 885-895.
- [6] E. Zukoski, Fluid dynamic aspects of room fires, In: *Fire Safety Science: Proc. of the First International Symp.*, Hemisphere, New York, 1984, pp. 1-30.
- [7] B.J. McCaffrey, Flame height, In: *SFPE handbook of fire protection engineering*, SFPE, Ed.), National Fire Protection Assoc., Quincy, MA, 1988, pp. 298-305.
- [8] J.G. Quintiere, *Fire Safety J.* 15 (1) (1989) 3-29.
- [9] S.P. Burke, T.E.W. Schumann, *Ind. Eng. Chem.* 20 (10) (1928) 998-1004.
- [10] F.G. Roper, *Combust. Flame* 29 (3) (1977) 219-226.
- [11] W.H. Twilley, V. Babrauskas, *User's guide for the cone calorimeter*, SP-745, National Institute of Standards and Technology, Gaithersburg, MD, 1988.
- [12] C. Huggett, *Fire Mater.* 4 (2) (1980) 61-65.
- [13] B. Hirst, K. Booth, *Fire Technol.* 13 (4) (1977) 296-315.
- [14] M.K. Donnelly, W.L. Grosshandler, *Suppression of fires exposed to an external radiant flux*, NIST IR 6827, National Institute of Standards and Technology, Gaithersburg MD, 2001.
- [15] G.T. Linteris, G.W. Gmurczyk, Prediction of HF formation during suppression, In: *Fire suppression system performance of alternative agents in aircraft engine and dry bay laboratory simulations*, R.G. Gann, Ed.), National Institute of Standards and Technology, Gaithersburg, MD, 1995, pp. 201-318.
- [16] L. Orloff, *Proc. Combust. Inst.* 18 (1981) 549-583.
- [17] V. Babrauskas, W.H. Twilley, W.J. Parker, *Fire Mater.* 17 (2) (1993) 51-63.
- [18] R.E. Mitchell, A.F. Sarofim, L.A. Clomburg, *Combust. Flame* 37 (3) (1980) 227-244.
- [19] A. Gomez, G. Sidebotham, I. Glassman, *Combust. Flame* 58 (1) (1984) 45-57.

Flame Size, Heat Release, and Smoke Points in Materials Flammability¹

Gregory Linteris and Ian Rafferty
Fire Science Division
National Institute of Standards and Technology
100 Bureau Dr. Stop 8665
Gaithersburg, MD 20899-8665

ABSTRACT

The concept of using the flame size as a surrogate for heat release rate has been explored. A technique for simultaneously obtaining the heat release rate, flame size (height and area), and the smoke point of the flame solely from visual images has been developed. The technique has been demonstrated on gaseous flames (methane, propane, ethylene, and propylene) and explored for five burning solid polymers. Estimations of the flame *area* from images of the stoichiometric contour based on the CH chemiluminescent region of the flames yielded a good linear correlation with measured heat release rate, valid for all of the gaseous and solid compounds tested, for burning rates above or below the smoke point. In contrast, flame *heights* and luminous images (i.e., from soot emission) were confounded by differing behavior above and below the smoke point.

KEYWORDS: Material flammability, heat release rate, flame size, cone calorimeter

INTRODUCTION

The heat release rate (HRR) of a burning material is important for quantifying the growth and spread of a fire in a building [1], and effective methods for its measurement have been used extensively [2-4]. Nonetheless, if a faster screening method could be developed which allowed rapid, parallel, high-throughput testing, combinatorial methods might be applied to the problem of fire retardant development [5]. The height of co-flow laminar jet flames is known to be correlated with heat release rate [6-9], and work has recently appeared in which the reduction in flame size is used as a metric for fire retardant effectiveness [10]. Hence, it is useful to investigate the conditions under which flame size itself could be

¹ Linteris, G.T. and Rafferty, I.P., "Flame Size, Heat Release, and Smoke Points in Materials Flammability," Fire Safety Journal, 43: 442 – 450, 2008.

used as a more-easily measured metric for heat release [11], as has been done for large fires [12]. Further, there is interest in using the method for situations for which heat release rate is desired, but capability for oxygen consumption calorimetry is not available (for example, in experiments to be flown aboard the International Space Station [13]). The purpose of the present work is to investigate the utility of flame size as a surrogate for heat release rate measurements on burning polymers, and to understand the limitations of the technique (since it is already being discussed by others for possible application).

BACKGROUND

Flame size has been related to heat release rate indirectly in the past through work predicting the flame size as a function of fuel flow rate. Various researchers have analytically solved the conservation equations for mass, momentum, species, and energy with some approximations. The flames are modeled as 2-D, axisymmetric, laminar and steady, with infinitely fast chemistry, binary diffusion, and unity Lewis number, while neglecting buoyancy, radiation heat transfer, and axial transport (radial is included) [6-9,14]. Burke and Schumann [6] published the first analytical solution for the size of a jet diffusion flame. In their formulation the conservation equations for mass, species, momentum, and energy were essentially recast as a species conservation equation for a mixture fraction. Their assumptions included: no buoyancy, equal and constant velocity for the fuel jet and co-flowing air, no radial velocity, infinitely fast kinetics, constant gas density and diffusivity throughout the flame. Fay [7] extended the analysis to include variable density, and found that the predicted flame lengths were about 2.4 times those of the constant density solution. Roper [8] again extended the analysis assuming: constant temperature and diffusivity, unity Schmidt and Lewis numbers (i.e., equal rates for the diffusion of heat, mass, and momentum), and axial velocities which were constant for all radii. Chung and Law [14] included streamwise and preferential diffusion, and showed that these effects can be important for low Peclet number (Pe), i.e., low velocity, flows. Roper et al. [15] assembled experimental data from previous researchers and collected new data to verify their model [15]. In their experiment, the height of the flame

tip was determined from measurements of CO or soot disappearance, and they noted that the visible flame appearance is typically not a good marker for the stoichiometric flame contour.

Although the linear correlation between fuel addition rate and flame height is expected to hold for solid fuels, less work has been done to demonstrate this relationship, and there is reason to believe that the simplifying assumptions in the analytical descriptions could be less accurate for the flames over solid materials. For example, the analyses described above for flame size vs. fuel flow have typically concerned relatively high velocity, narrow, gaseous fuel jets, producing long, narrow flames (i.e., large aspect ratio). For solid material flammability, however, the flames will be wider and the fuel velocity at the surface will be lower. This increases the importance of axial diffusion (usually neglected in analytical descriptions). The lower fuel velocities reduce the Froude number, increasing the role of buoyancy, which has been shown to decrease flame widths due to radial convection (i.e., increased oxygen transport rates over molecular diffusion) [16]. Buoyancy-induced vortices also cause flame flicker, violating the assumption of a steady flame. Several properties of the burning materials will affect the assumption of infinitely fast gas-phase kinetics at the reaction sheet: 1.) The materials will have a wide range of molecular structure, producing flames with varying sooting properties, and when added fire retardants are present, they too will produce incomplete combustion; and 2.) Heat losses to the fuel surface and from flame radiation (especially with sooting flames) will lower the flame temperature, again lowering the overall reaction rate. Hence, it is not clear a priori if all of the assumptions which have been necessary for the analytical solutions for flame height as a function of fuel flow rate for gas jets will be justified for flames over condensed phase materials. There have been no publications in which the measured heat release rate of a flame is compared with the flame size for burning condensed-phase materials, and the assumption of complete combustion of the fuel may need further consideration.

One useful measure of the completeness of combustion for fuels has been the laminar flame smoke point [17-20]. Measured in various ways, the smoke point is essentially the fuel flow rate for which the flame just begins to emit smoke, and it has been correlated with both the flame radiation heat

losses and the incompleteness of combustion [21-23]. Hence, with regard to material flammability testing, the smoke point is a particularly important parameter, as has been described previously [24], since radiation heat losses, smoke formation, and combustion efficiency are all crucial parameters for fire modeling. The accuracy of the present correlations of flame size with heat release rate may depend upon the fuel generation rate with regard to the smoke point. Hence, it is necessary to consider the smoke point and if possible, measure it simultaneously.

The present work reports the flame height and flame area, together with the measured heat release rate for four gaseous and five polymeric fuels. The correlation between the flame size and the heat release is discussed, as is the smoke point and its relationship to the correlations developed. The utility of the present experimental technique for providing simultaneous measurement of the flame heat release and the smoke point for polymers is described.

EXPERIMENT

In order to produce flames which could be used in a combinatorial screening method, small laminar flames were employed. An experiment was designed for obtaining flame size and heat release rates for steady flames of solid or gaseous fuels with measured mass consumption rates. The burner is shown schematically in Fig. 1. For gaseous fuels, (Fig. 2) the burner is a variation of the cup burner [25,26], with a fuel “jet” consisting of a cylindrical glass cup (28 mm diameter) centered in a glass chimney (9.5 cm diameter). The fuel jet is made of pyrex (1.5 mm thick) and contains glass beads (3 mm diameter) with two screens (15.8 mesh/cm) on top to provide flow straightening. The co-flowing region contains a 10 cm thick bed of glass beads (6 mm diameter) to provide straightening for the oxidizer stream. For the polymer fuels, the burner is a variation of one used previously to study suppression of fires over solid materials [27]. The fuel is a solid sample (2.5 cm diameter and 2.5 cm tall), centered in a 8.5 cm dia. glass chimney; a scale (Mettler PE360²) measures the sample mass as a function of time. A

² Certain commercial equipment, instruments, or materials are identified in this paper to adequately specify the procedure. Such identification does not imply recommendation or endorsement by NIST, nor does it imply that the materials or equipment are necessarily the best available for the intended use.

radiant coil heats the solid samples to provide varying fuel supply rates. The heater is the same as that used in the cone calorimeter [4] but it is situated further from the sample (10 cm to 21 cm) so the flame image is not occluded by the cone heater. In both burners the chimney is cut off at a point just below the burner rim to avoid reflections during flame imaging. A co-flowing oxidizer stream (16.7 cm/s) helps to suppresses flame flicker. Nonetheless, for the flame height measurements of the gaseous fuels, flame flicker was additionally suppressed using stabilizing screens [28]. There were six screens, 8 mesh/cm, 10 cm in diameter, with the first starting at the burner height, and each of the next located 2.54 cm above the previous. Each of the screens, in order, had a hole in the center of (40, 36, 32, 28, 24, and 20) cm diameter, with the largest hole in the lowest screen. For measurement of heat release, the exhaust products from either burner are directed to the hood of the NIST cone calorimeter, which uses oxygen consumption calorimetry [29]. To insure accurate results in the lower range of heat release characteristic of the cup burner, the exhaust fan speed of the cone was reduced by a factor of two from the ordinary setting (30 g/s), and the system was calibrated with controlled methane flows in the approximate heat release range of the reduced-scale samples (0.12 kW to 0.35 kW). For this heat release range, the measured heat release rate from the cone calorimeter is within 5 % of that based on the heat release from the flame of a measured methane calibration flow (and within 10 % at 0.05 kW). This agreement is considered good since the cone calorimeter itself, even at higher flows, has an uncertainty on the order of at least 5 % [30]. Gas flows are measured by mass flow controllers (Sierra 860) which were calibrated so that their uncertainty is 2 % of indicated flow. The fuels used were methane (Matheson UHP, 99.9%), propane (Matheson CP, 99%), ethylene, propylene (Matheson, CP), and various commercially available polymers, including Acrylonitrile Butadiene Styrene (ABS), poly(methyl methacrylate) (PMMA), polypropylene (PP), high density polyethylene (HDPE), and polystyrene (PS). The air was house compressed air (filtered and dried) which is additionally cleaned by passing it through an 0.01 μm filter, a carbon filter, and a desiccant bed to remove small aerosols, organic vapors, and water vapor.

The flame size was determined with digital photography, using automated software to locate the flame contour and calculate the flame height or area. The flame images were recorded with a black and white Charge Coupled Device CCD video camera (Sony, XC-ST50), coupled to a video frame-grabber board (with a resolution of 640 x 480 and a framing rate of 2 Hz) in a Pentium II-based personal computer. One or two interference filters, each with a bandpass of 10 nm centered at 430 nm (Oriol No. 59295) were used in series to isolate the emission line from excited CH radicals. This was done to facilitate imaging of the main reaction zone of the flame (which closely aligns with the stoichiometric contour) [31] rather than the luminosity from flame soot (which may not coincide with the stoichiometric contour). For comparison purposes, images were collected and analyzed with zero, one, or two filters. The flame images (obtained using two filters) were analyzed to determine the flame height, area, and volume using an automated image analysis system based on two software packages. The NASA image processing freeware program Spotlight 1.1 [32] provided the flame outline from the color image. A custom-written program subsequently interpreted the outline and calculated the flame surface area and volume. This process was repeated for each of the thirty frames of data and the results averaged.

For the small, non-flickering, nearly-conical laminar flames, estimation of the flame height and area from the flame outline was straightforward, obtained by measuring the flame cord width at each height, and assuming axial symmetry, summing segments as described below. For convoluted flames typical of more turbulent conditions, the program was also capable of analyzing the flames using the method described by Orloff [33]. The total surface area or volume of the flame is the sum of all horizontal segments. Using this approach for complicated turbulent flame shapes, Orloff was able to produce flame areas within about 5 % of those obtained from integration of the flame presence probability density function. Hence, we estimate that at the 95 % confidence level, the luminous flame area for the small laminar flames (which have very regular shapes), have an uncertainty of less than 1 %. Note that in many of the figures which follow, if the uncertainty is shown on the data points, the error bars represent the standard deviation (66 % confidence level) for the variation in the flame area for the 30 frames of data

(due to residual flame flicker). This uncertainty is much larger than that due to the flame area determination techniques described above.

For other measured parameters, an uncertainty analysis was performed, consisting of calculation of individual uncertainty components and root mean square summation of components. All uncertainties are reported as *expanded uncertainties*: $X \pm ku_c$, from a combined standard uncertainty (estimated standard deviation) u_c , and a coverage factor $k = 2$. Likewise, when reported, the relative uncertainty is ku_c / X . The expanded relative uncertainties for the theoretical heat release for the gaseous fuel flames (based on gas flow rates) are 4%. For the solid fuels, the heat release is measured by the cone calorimeter. Although the accuracy of that device is usually stated to be around 5%, at the low heat release rates of the present measurements, our calibration runs with methane indicate that the combined relative uncertainty is about 10%.

RESULTS AND DISCUSSION

Using the reduced-scale laminar burner described above, flame images (with and without CH-line filters) at varying fuel flow (or generation) rates were collected for four gases and five polymers. The heat release rate using oxygen consumption calorimetry was obtained simultaneously, as was the fuel mass addition rate to the flame.

Gases

To understand and interpret the relationship between the measured visual flame size, heat release, and smoke point in the present laminar flames, we first conducted experiments using gaseous fuels. Experiments with methane, propane, ethylene, and propylene fuels provided a range of sooting tendency, and increasing fuel flow rates provided a range of flame size. For the soot-emitting flames (propane, ethylene, and propylene), the smoke point was determined (with stabilizing screens present) as the measured heat release at which the flame tip began to emit visible smoke. Visual images obtained using 0, 1, and 2 CH line filters in series with the CCD camera allowed discrimination between the region of

soot particle blackbody emission (here called the luminous flame) and the main reaction zone of the flame (i.e., region of CH chemiluminescence), here referred to as the stoichiometric contour.

Results for four fuels are shown in the four plots in Fig. 3. In each plot for a given fuel, the flame area (open symbols) is given by the left scale, while the flame height (solid symbols) is given by the right scale; data for 0, 1, and 2 CH line filters are given by the circles, triangles, and squares. The uncertainty on the flame area or height grows with increasing heat release rate because the larger flames flicker more, yielding more frame-to-frame variation in the flame size (the stabilizing screens were used only for the manually-determined smoke points). For methane, the smoke point heat release rate was beyond the range of the present tests (about 0.3 kW), whereas for propane, ethylene and propylene, the smoke point heat release rates were 0.31, 0.21, and 0.073 kW, and are indicated on the figures (dotted vertical line).

As all plots in Fig. 3 show, the inferred flame sizes with one or two filters are essentially the same. With 0 filters, however, the luminous flame image (from soot luminosity) is sometimes different from that with 1 or 2 filters, indicating that the soot-containing region does not always overlap with the stoichiometric contour of the flame. In the present work, the soot emission region is coincident with or larger than the image from the main reaction zone of the flame (i.e., the stoichiometric contour), in agreement with the results of Sunderland et al. [16], Mitchell et al. [34], and Gomez et al. [18], but in contrast to those of Roper et al. [15]. Further, the flame size determined from the luminous image compared to that from the stoichiometric contour depends upon the flame size relative to that at the smoke point. Below the smoke point, the flame sizes from the luminous flame and from the CH emission are essentially the same. For example, for methane (top left plot in Fig. 3), which is always below its smoke point in the present measurements (i.e, non-soot emitting) the flame height and area based on the luminous flame are slightly larger than the stoichiometric contour, but are quite close overall. For propane (top right in Fig. 3), the luminous and stoichiometric flame sizes are very close for all but the last few data points (which are near the smoke point). For the highly sooting flames of ethylene and propylene, however, behavior above and below the smoke point is clearly different. In both cases, below

the smoke point flame size, the flame height or area with 0, 1, or 2 filters are essentially identical. Whereas above the smoke point fuel flow, the height and area are 23 % to 47 % larger when based on the luminous flame. These results are consistent with those of deRis and Cheng [24] for ethylene and propylene, which also show roughly linear variation of flame height with fuel flow rate below the smoke point (note that they use both a different burner configuration and smoke point determination method). Interestingly, both the present data as well as those of de Ris and Chang show that the flame height starts to change dramatically slightly below the fuel flow rate at which large amounts of soot are released. (Note also that the two experimental measurements, the smoke point determination and the flame size determination, are necessarily slightly different : the smoke point determination used stabilizing screens, but the flame size measurements could not (because the light scattered from the screens interfered with the flame determination in the image processing). These differences may contribute to the discrepancy between the smoke points determined by the two techniques.)

The results in Fig. 3 indicate that use of the *two* visual images (i.e., the luminous image and CH emission region) can determine the smoke point. Further, below the smoke point fuel flow rate, either flame *height* or flame *area* provides a linear relationship with the heat release rate, while above the smoke point, there is an apparent change in slope for the *height* versus the heat release, which is not as severe for the flame *area*. In general, flame area appears to be correlated with measured heat release rate better than does flame height.

As an example, the data in Fig. 3 from the present optical measurements can be used to determine the smoke point flame height (or heat release rate) for ethylene and propylene. In the lower two images of Fig. 3 for ethylene and propylene, the point at which the flame height determined with zero (closed red circles) or two (closed blue squares) filters diverges is marked with the arrow and labeled SP_0 . These values for ethylene and propylene, 7.8 cm and 3.9 cm, are slightly lower than the smoke points determined based on manual, visual observations of the flame (with stabilizing screens) as described above.

For the four gaseous flames, the results of measurements of the stoichiometric flame size (height and area, using two filters) and the heat release are presented together in Fig. 4. Examining the upper assembly of data points (for flame height), the gaseous flames of propane, ethylene, and propylene all fall on the same linear curve, while those for methane (open circles) are noticeably smaller. For the flame area, the methane flames are again slightly smaller than the other gases, likely due to the higher mass diffusivity of methane compared to the other fuels, consistent with laminar flame theory [8]. Considering all of the gases together, the flame area is well correlated with the heat release rate ($r^2=0.95$), while the flame height is a little less well correlated ($r^2=0.85$).

The data used to generate Fig. 3 for the gaseous fuels can also provide data on the combustion efficiency as a function of flame size. For the four gaseous fuels, methane, propane, ethylene, and propylene in the current laminar flame burner, the measured combustion efficiencies (based on the lower heating value) are shown in Fig. 5. These are calculated from the ratio of the measured heat release rate from oxygen consumption calorimetry and that based on the measured mass flow rate times the theoretical heat of combustion (lower heating value) of the fuel. For methane, the raw data of the HRR from O_2 consumption was about 4 % higher than that based on the mass flow rate. In our data reduction, the combustion efficiency for methane was assumed to be unity, and that curve was used as a calibration curve for the system; that is, all values of HRR based on O_2 consumption for all fuels in Fig. 5 were lowered by 4 %.

As Fig. 5 shows, the combustion efficiency for propane, ethylene, and propylene are about 0.96, 0.79, and 0.74. For these fuels, the combustion efficiency drops off for the lowest flow rate (perhaps due to increased heat loss and subsequent lower temperature in these smaller flames), while ethylene and propylene also show decreases in the combustion efficiency as the flames grow significantly above their smoke point. These values of combustion efficiency compare to 0.95, 0.87 and 0.87, respectively, as reported by Tewarson [35] for flames in the FMRC Fire Propagation Apparatus (ASTM E2058: 10 cm x 10 cm burner size and turbulent conditions). Hence, the combustion efficiency in the present apparatus is

lower than in the E2058 test, (perhaps due to lower temperatures in the present apparatus from higher gas-phase conductive heat losses from the burning region). The lower measured combustion efficiency highlights the importance of both the heat losses from the flame, as well as the necessity of measuring the heat release rate from the flame rather than basing the heat release on the measured fuel consumption.

Polymers:

Data for the flame height and area (using two filters) as a function of the measured heat release rate for the polymers is also shown in Fig. 6. Data are presented for burning with an imposed heat flux from the radiant heater of 0 or 4.7 kW/m²; the relatively low incident flux resulted from the need to position the cone heater relatively far above the sample (10 cm to 21 cm) so the flame was still visible. A varying net heat flux to the vaporizing polymer was obtained during the burn as the sample heated. As indicated, both the flame height and area are linearly related to the heat release rate, with the area ($r^2=0.96$) again better correlated than the height ($r^2=0.88$). Nonetheless, it is important to consider the smoke point of the burning polymers, since, as shown above and in ref. [24], the flame shape relative to the heat release rate can change drastically above and below the smoke point.

Of the polymers tested here (PMMA, ABS, PE, PP, PS), there are data in the literature on the smoke point for all but ABS [35]. Table 1 shows the smoke point data from ref. [35], together with those from [24] and the current results for ethylene and propylene from both the manual and automated optical techniques. As noted in ref. [35], the values of smoke point are apparatus dependent. Hence, we have linearly scaled the values in ref. [35] to our apparatus using the common results for ethylene and propylene, as shown in Table 1. The implied smoke point flame heights for PMMA, PE, PP, and PS are 11 cm, 4.7 cm, 5.3 cm, and 1.6 cm. (Note that in our experiments, all of the ABS runs emitted visible smoke.) Comparing these values with the range of flame heights in the present tests (as shown in Fig. 6 for each compound), all data for PMMA and PE are below their smoke point, while the larger flow conditions for PP and all the data for PS and ABS are above their smoke point. Although sufficient data were not always available (described below) to determine the smoke point for the polymers using the

optical method described above for ethylene and propylene, where data were available they were consistent with the smoke point flame heights just described. The important point is that the actual burning conditions of polymers will likely involve flame heights which are sometimes above and sometimes below the smoke points. Hence, it is important to have a flame size – heat release rate correlation method which allows one to extract data for the whole range of fuel generation rates to be encountered in practice. As shown above for ethylene and propylene, the linear relationship for flame area vs. heat release rate is accurate both above and below the smoke point, while that for flame height is somewhat less accurate.

General Considerations

An average value of the heat release per unit area of the flame can be extracted from the present results. From the data of Fig. 4 and Fig. 6 together, the inverse of the slope of the flame area versus the heat release rate gives a value of 80 kW/m^2 . Based on an energy release per mass of O_2 or 13100 kJ/kg [29], this value corresponds to mass flux of oxygen into the flames of 6.1 g/s/m^2 or 6.5 g/s/m^2 , respectively. For our flames, the average value of the ratio of flame volume to flame area was 0.25 cm for propane, ethylene, and propylene, 0.32 cm for methane, and ranged from 0.25 cm to 0.45 cm for the polymers.

While the present work focused on the relationship between flame area and heat release, future work could help with several practical considerations related to the use of the technique as a screening method. These include: 1.) unsteady and multi-dimensional heat losses in the sample, and 2.) properties of the experimental flame imaging system. The unsteady heating of the polymer sample in the present tests was used as a means to obtain varying heat release rates at a given incident radiant flux (that is, the time varying conductive losses to the thick sample changed the *net* heat input available for gasifying the sample). In actual practice, however, one typically wants to know the heat release rate at a given known *net* heat input. Hence, some means to insure a steady state condition (or estimate the conductive losses) would be necessary (for example using thin samples of limited burning domain, as in [24]). Similarly,

two-dimensional heat losses from the edges of the sample will also change the net heat flux delivered from the radiant heating system. Some means would be necessary either to estimate these heat losses from the different samples or control them so they are the same for the different samples being screened. Finally, the imaging system in the present work could be improved by using a heater configuration which does not occlude the flame at high fluxes. A more sensitive camera with a larger dynamic range would allow better resolution of the weak, blue regions of the flame simultaneously with the bright (even after filtering), sooting regions.

CONCLUSIONS

A method has been developed for simultaneously obtaining the flame size, heat release and smoke point for flames over condensed-phase materials. From these, a correlation can be determined so that the heat release rate can be obtained solely from the optically measured flame area. Recorded images of the luminous flame (from soot emission) and that from CH emission (approximating the stoichiometric contour) diverge above the smoke point fuel addition rate so that the smoke point is readily determined. The flame area and the stoichiometric contour are found to be superior to the flame height and the luminous flame for correlating heat release rate. In addition, there exist several important considerations with regard to the actual implementation of the technique in a screening apparatus. For the small sample size here, account must be made of the unsteady and the multi-dimensional heat loss terms in the energy balance equation, since these can greatly reduce the effective heat input to the sample from the radiant source.

ACKNOWLEDGEMENTS

The authors thank Dr. Richard Lyon for his initial suggestion of using flame size as a measure of heat release rate for burning polymers. This research was supported by NIST and NASA's Office of Biological and Physical Research. One author (IPR) was supported by a NIST Summer Undergraduate Research Fellowship funded by the NSF.

REFERENCES

- [1]. Babrauskas, V, Peacock, RD. Heat release rate - the single most important variable in fire hazard. *Fire Safety J.* 1992; 18:255-72.
- [2]. Tewarson, A. Flammability of polymers and organic liquids, Part I, Burning intensity. Factory Mutual Research Corp. FMRC Serial 22429, Norwood, MA, 1975.
- [3]. Ostman, BAL, Svensson, IG, Blomqvist, J. Comparison of 3 test methods for measuring rate of heat release. *Fire Mater.* 1985; 9 :176-84.
- [4]. Twilley, WH and Babrauskas, V. User's guide for the cone calorimeter. National Institute of Standards and Technology SP-745, Gaithersburg, MD, 1988.
- [5]. Gilman, JW, Bourbigot, S, Shields, JR, Nyden, M, Kashiwagi, T, Davis, RD, Vanderhart, DL, Demory, W, Wilkie, CA, Morgan, AB, Harris, J, Lyon, RE. High throughput methods for polymer nanocomposites research: extrusion, NMR characterization and flammability property screening. *J. Mater. Sci.* 2003; 38:4451-60.
- [6]. Burke, SP, Schumann, TEW. Diffusion flames. *Ind. Eng. Chem.* 1928; 20:998-1004.
- [7]. Fay, JA. The distributions of concentration and temperature in a laminar jet diffusion flame. *Journal of Aeronautical Sciences* 1954; 21:681-89.
- [8]. Roper, FG. Prediction of laminar jet diffusion flame sizes. 1. Theoretical model. *Combust. Flame* 1977; 29:219-26.
- [9]. Spalding, D. B., Editors. *Combustion and mass transfer.* New York:Pergamon Press; 1979 185-195.
- [10]. Endtner, JM. Development of new halogen-free flame retardant engineering plastics by application of automated optical investigation methods. 10th European Meeting on Fire Retardancy and Protection of Materials, Berlin, Germany, 2005.,
- [11]. Lyon, R., FAA, Personal Communication, 2003.
- [12]. Orloff, L, de Ris, J. Froude modeling of pool fires. *Proc. Combust. Inst.* 1982; 19:885-95.
- [13]. Olson, S., NASA, Personal Communication, 2003.
- [14]. Chung, SH, Law, CK. Burke-Schumann flame with streamwise and preferential diffusion. *Combust. Sci. Technol.* 1984; 37:21-46.
- [15]. Roper, FG, Smith, C, Cunningham, AC. Prediction of laminar jet diffusion flame sizes. 2. Experimental verification. *Combust. Flame* 1977; 29:227-34.
- [16]. Sunderland, PB, Mendelson, BJ, Yuan, ZG, Urban, DL. Shapes of buoyant and nonbuoyant laminar jet diffusion flames. *Combust. Flame* 1999; 116:376-86.

- [17]. Schalla, RL and Hubbard, RR. Smoke and coke formation in the combustion of hydrocarbon-air mixtures. NASA NACA Report 1300, 1959.
- [18]. Gomez, A, Sidebotham, G, Glassman, I. Sooting behavior in temperature-controlled laminar diffusion flames. *Combust. Flame* 1984; 58:45-57.
- [19]. Kent, JH. A quantitative relationship between soot yield and smoke point measurements. *Combust. Flame* 1986; 63:349-58.
- [20]. Delichatsios, MA. Smoke yields from turbulent buoyant jet flames. *Fire Safety J.* 1993; 20:299-311.
- [21]. Markstein, GH. Relationship between smoke point and radiant emission from buoyant turbulent and laminar diffusion flames. *Proc. Combust. Inst.* 1985; 20:1055-61.
- [22]. Tewarson, A. Smoke-point flame height and fire properties of materials. Factory Mutual Research Corp. FMRC Technical Report J.I. OK3R3.RC, NIST-GCR-88-555, Norwood, MA, 1988.
- [23]. Orloff, L, de Ris, J, Delichatsios, MA. Radiation from buoyant turbulent-diffusion flames. *Combust. Sci. Technol.* 1992; 84:177-86.
- [24]. de Ris, J, Cheng, XF. Role of smoke-point in material flammability testing. International Association for Fire Safety Science. Proceedings. 4th International Symposium. Ottawa, Ontario, 301.
- [25]. Hirst, B, Booth, K. Measurement of flame extinguishing concentrations. *Fire Technol.* 1977; 13:296-315.
- [26]. Linteris, GT, Gmurczyk, GW. Prediction of HF formation during suppression. In: R.G. Gann, Editors. Fire suppression system performance of alternative agents in aircraft engine and dry bay laboratory simulations. Gaithersburg, MD:National Institute of Standards and Technology; 1995 201-318.
- [27]. Donnelly, MK and Grosshandler, WL. Suppression of fires exposed to an external radiant flux. National Institute of Standards and Technology NIST IR 6827, Gaithersburg MD, 2001.
- [28]. Kent, JH, Wagner, HGg. Why do diffusion flames emit smoke? *Combust. Sci. Technol.* 1984; 41:245-69.
- [29]. Huggett, C. Estimation of rate of heat release by means of oxygen-consumption measurements. *Fire Mater.* 1980; 4:61-65.
- [30]. Babrauskas, V. Development of the cone calorimeter -- a bench-scale heat release rate apparatus based on oxygen-consumption. National Bureau of Standards NBSIR 82-2611, Gaithersburg, MD, 1982.
- [31]. Walsh, KT, Long, MB, Tanoff, MA, Smooke, MD. Experimental and computational study of CH, CH*, and OH* in an axisymmetric laminar diffusion flame. *Proc. Combust. Inst.* 1998; 27:615-23.

- [32]. Klimek, R. Wright, T. Spotlight 1.1. Cleveland, OH:NASA Glenn Research Center, 2002.
- [33]. Orloff, L. Simplified radiation modeling of pool fires. Proc. Combust. Inst. 1981; 18:549-83.
- [34]. Mitchell, RE, Sarofim, AF, Clomburg, LA. Experimental and numerical investigation of confined laminar diffusion flames. Combust. Flame 1980; 37:227-44.
- [35]. Tewarson, A. Generation of heat and chemical compounds in fires. In: Beyler, C. L., Custer, R. L. P., Walton, W. D., Watts, J. M. Jr., Drysdale, D., Hall, J. R. Jr., and Dinunno, P. J., Editors. SFPE Handbook of Fire Protection Engineering. Quincy, MA:National Fire Protection Association; 1995 3-53 to 3-124.

Figure Captions

- Fig. 1 – Schematic of the laminar flow burner for testing polymer samples with radiant heating.
- Fig. 2 – Schematic diagram of the top of the burner used for gaseous fuels.
- Fig. 3 – Measured flame area (left scales) and height (right scales) with 0 (●), 1 (▲), or 2 (■) bandpass filters for a.) methane, b.) propane, c.) ethylene, and d.) propylene fuels. Dotted lines and small arrows marked SP_0 are the smoke point heat release rate, determined manually and with the optical imaging system.
- Fig. 4. Measured flame area (left scale) and height (right scale) with two filters vs. measured heat release rate for gases.
- Fig. 5 – Gaseous fuel heat release rate (HRR) from oxygen consumption calorimetry vs. that based on the fuel mass flow rate (open symbols, left scale) and the combustion efficiency (solid symbols, right scale).
- Fig. 6. Measured flame area (left scale) and height (right scale) with two filters vs. measured heat release rate for polymers.

Table 1 – Smoke point flame heights.

Compound	Smoke Point Flame Height (cm)				
	SFPE*	Present Work		SFPE (converted [‡])	Cheng and deRis [†]
		Manual Visual	Automated Optical		
Ethylene	9.7	12.0	7.8	10.2	13.7
Propylene	3.0	4.3	3.9	3.2	6.2
PMMA	10.5			11.0	6.8
PE	4.5			4.7	
PP	5.0			5.3	
PS	1.5			1.6	

* from ref. [35]

† from ref. [24]

‡ SFPE(converted) = SFPE x (7.8/9.7+3.9/3.0)/2

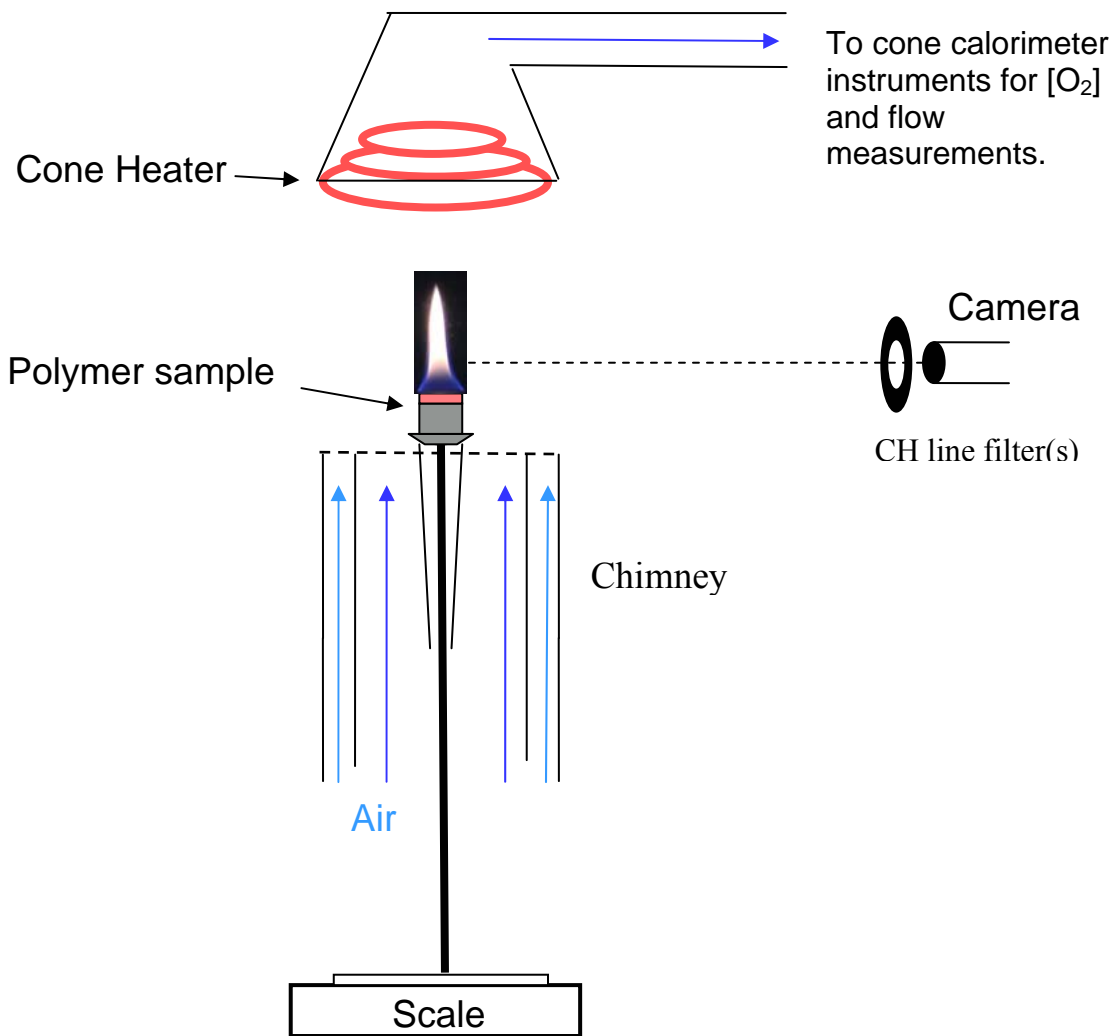


Fig. 1 – Schematic of the laminar flow burner for testing polymer samples with radiant heating.

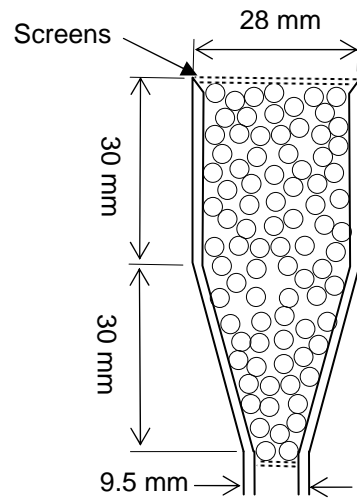


Fig. 2 – Schematic diagram of the top of the burner used for gaseous fuels.

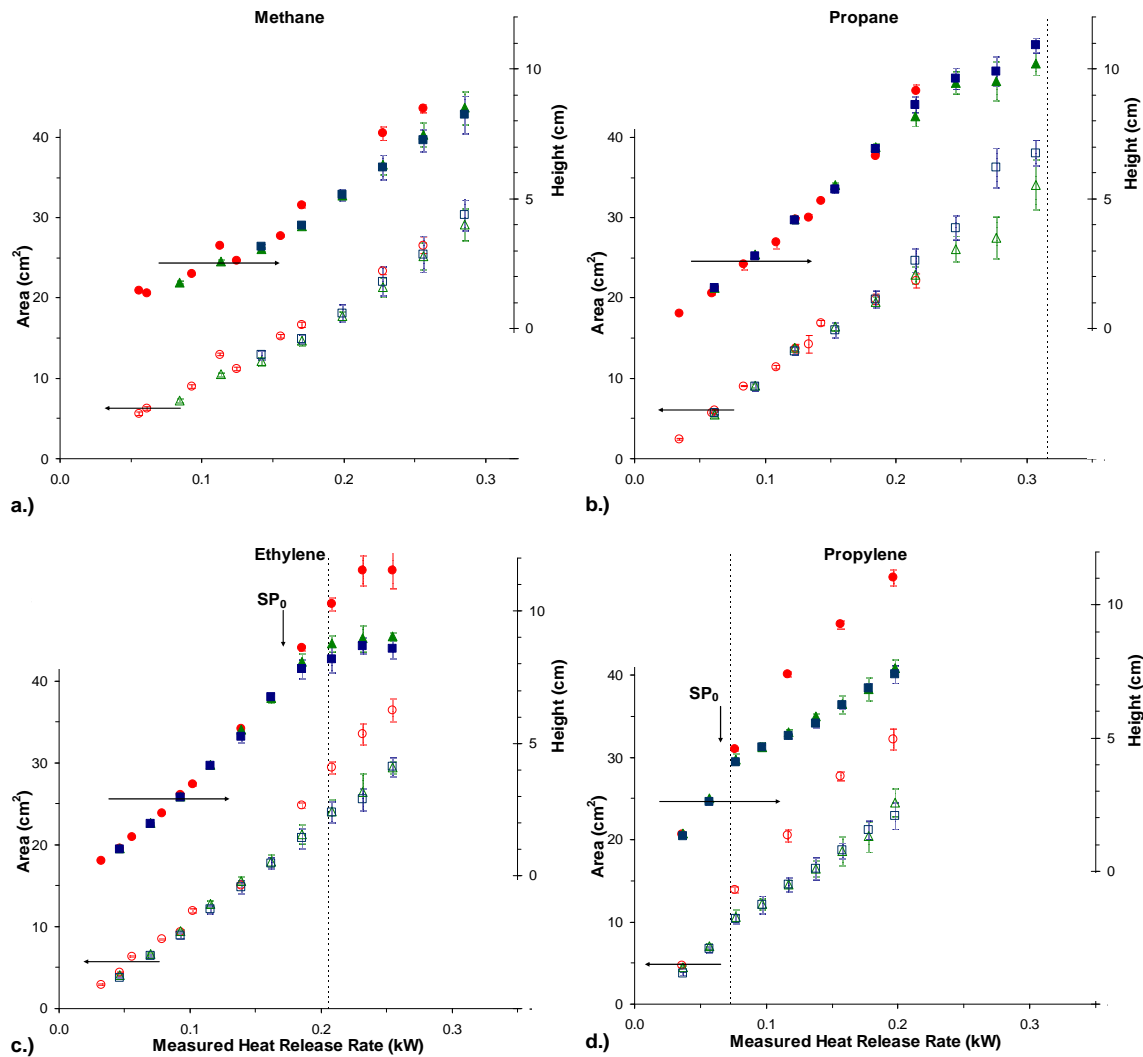


Fig. 3 – Measured flame area (left scales) and height (right scales) with 0 (●), 1 (▲), or 2 (■) bandpass filters for a.) methane, b.) propane, c.) ethylene, and d.) propylene fuels. Dotted lines and small arrows marked SP₀ are the smoke point heat release rate, determined manually and with the optical imaging system.

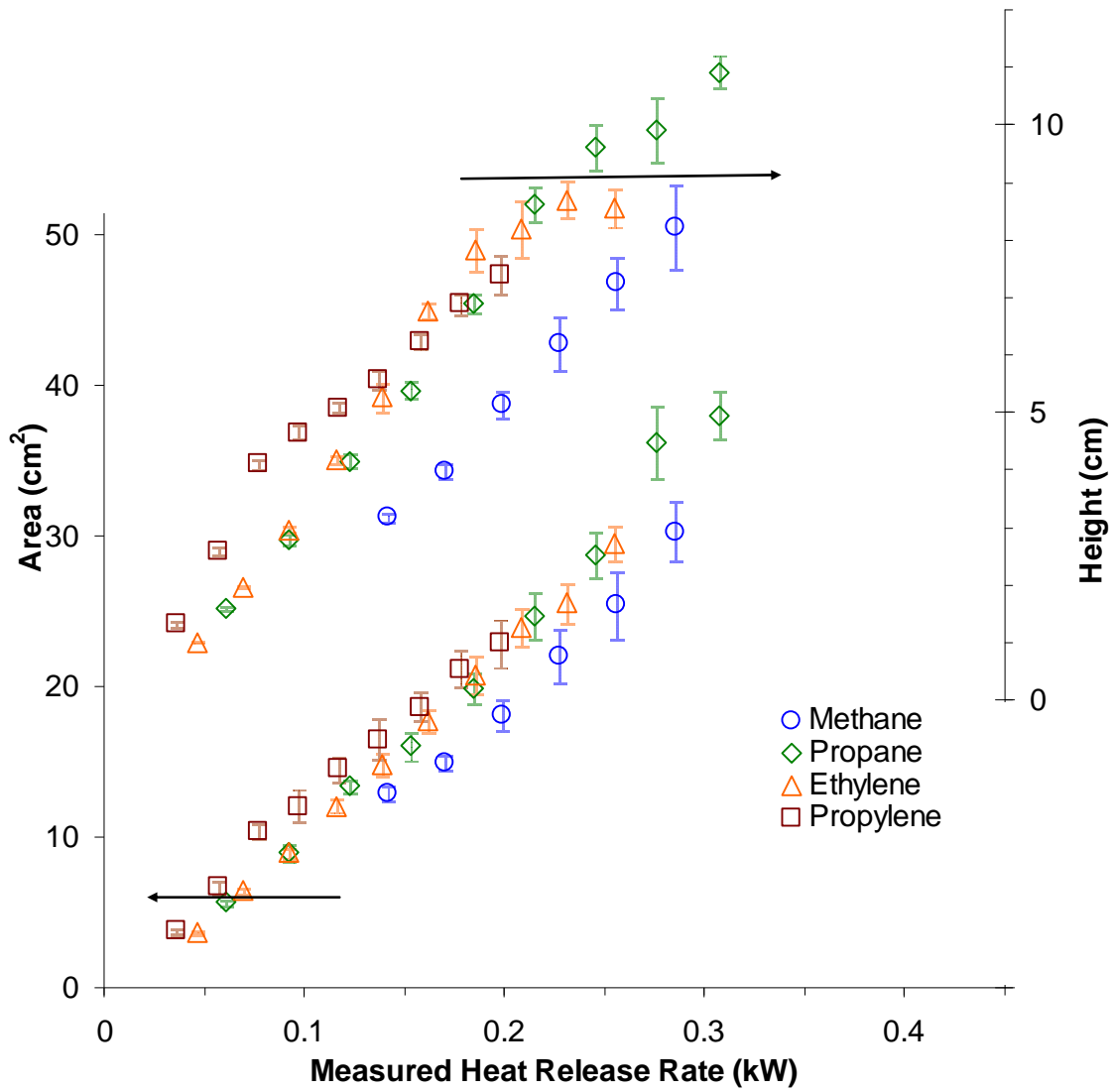


Fig. 4. Measured flame area (left scale) and height (right scale) with two filters vs. measured heat release rate for gases.

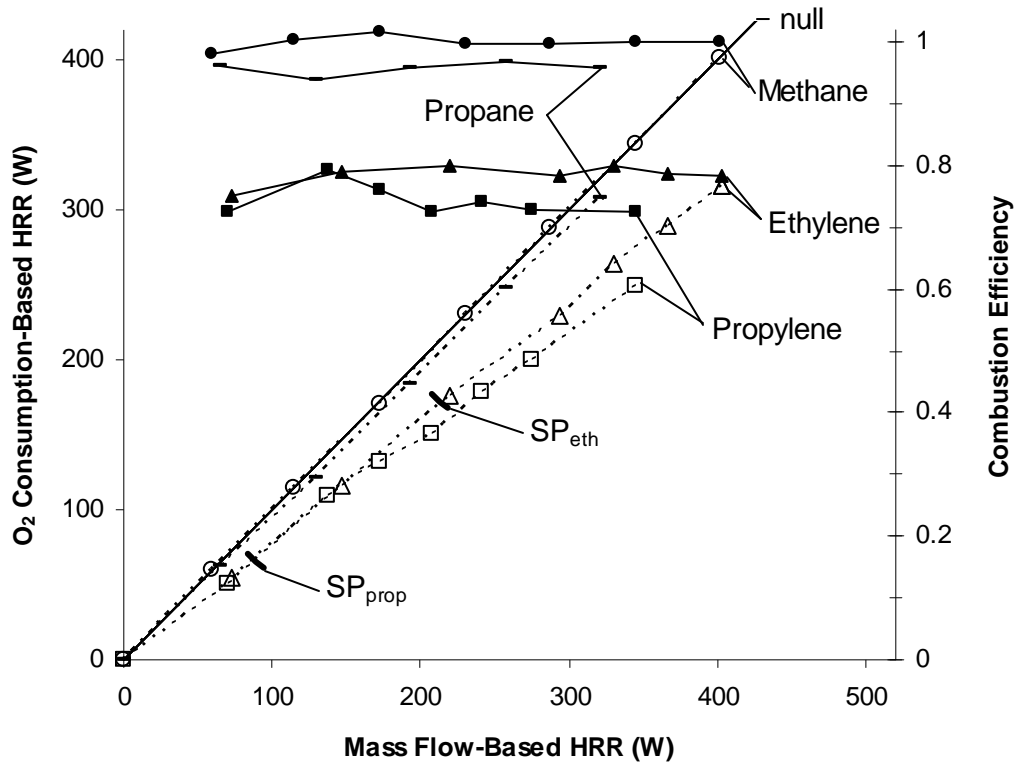


Fig. 5 – Gaseous fuel heat release rate (HRR) from oxygen consumption calorimetry vs. that based on the fuel mass flow rate (open symbols, left scale) and the combustion efficiency (solid symbols, right scale).

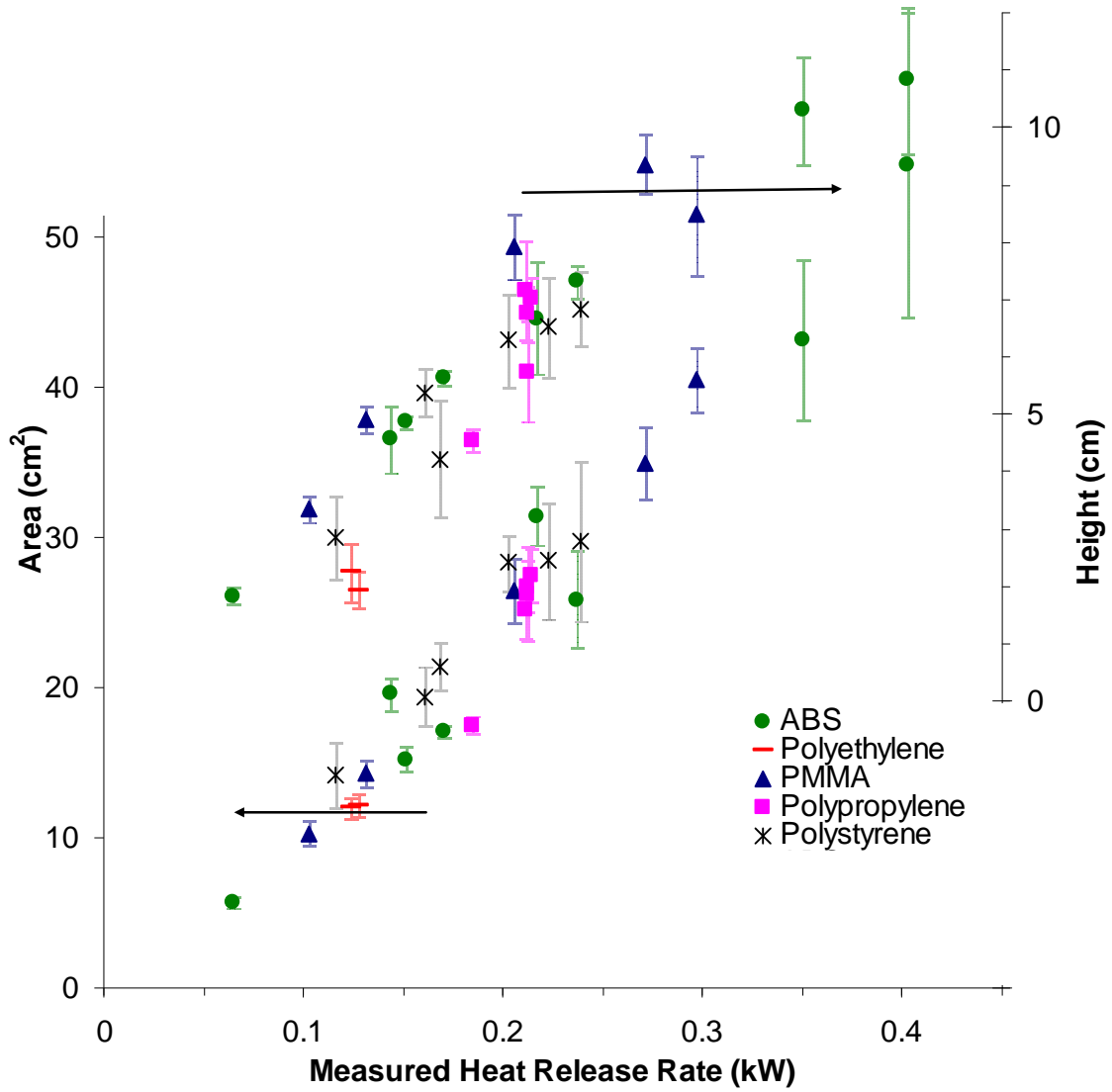


Fig. 6. Measured flame area (left scale) and height (right scale) with two filters vs. measured heat release rate for polymers.

Numerical Simulations of Thermoplastic Pyrolysis Rate: Effects of Property Variations*

G.T. Linteris

National Institute of Standards and Technology
Fire Science Division
100 Bureau Dr. Stop 8665
Gaithersburg, MD 20899;

To appear in *Fire and Materials*

Running title: Simulated Thermoplastic Pyrolysis

Key words: polymer flammability, fire retardant additives, fire modeling, material flammability.

Corresponding author:

Gregory T. Linteris
National Institute of Standards and Technology
Building and Fire Research Laboratory
100 Bureau Dr.; Stop 8665
Gaithersburg MD 20899-8665, USA

linteris@nist.gov
ph: 301-975-2283
fax: 301-975-4052

* Official contribution of NIST, not subject to copyright in the United States.

NOMENCLATURE

ΔH_g – heat of gasification, kJ kg^{-1}

ΔH_{reac} – heat of reaction, kJ kg^{-1}

ΔH_v – heat of vaporization, kJ kg^{-1}

T – temperature, K

\dot{m}'' – mass loss rate, $\text{g m}^{-2} \text{s}^{-1}$

\dot{q}_{net}'' – net heat flux, kW m^{-2}

\dot{q}_{ft}'' – heat flux from flame to surface, kW m^{-2}

\dot{q}_{loss}'' – heat flux from surface to ambient, kW m^{-2}

\dot{q}_{ext}'' – externally applied heat flux, kW m^{-2}

k – thermal conductivity, W m K^{-1}

c – specific heat, $\text{kJ kg}^{-1} \text{K}^{-1}$

E_a – Arrhenius activation energy of one-step material decomposition, kJ mol^{-1}

A – Arrhenius pre-exponential term for one-step material decomposition, s^{-1}

R – Universal gas constant, $\text{kJ mol}^{-1} \text{K}^{-1}$

S – sample thickness, m

Greek Symbols

α – absorption coefficient, m^{-1}

δ – thermal thickness (with respect to mass loss), m

δ_t – thermal conduction length, m

τ_{ign} – ignition time, s

Abbreviations

MLR – mass loss rate

MLR_{av} – average mass loss rate

EHF – external heat flux

Numerical Simulations of Polymer Burning Rate: Effect of Property Variations

Gregory Linteris
Fire Science Division
National Institute of Standards and Technology
100 Bureau Dr. Stop 8665
Gaithersburg, MD 20899-8665

ABSTRACT

The mass loss rate of poly(methyl methacrylate) (PMMA) exposed to known radiant fluxes is simulated with two recently-developed numerical codes, the National Institute of Standards and Technology (NIST) Fire Dynamics Simulator (FDS) and the Federal Aviation Administration (FAA) ThermaKin. The influence of various material properties (thickness, thermal conductivity, specific heat, absorption of infrared radiation, heat of reaction) on mass loss history is assessed, via their effect on the ignition time, average mass loss rate, peak mass loss rate, and time to peak. The two codes predict the influence of material parameters on the MLR in the order of decreasing importance: heat of reaction, thickness, specific heat, absorption coefficient, thermal conductivity, and activation energy of the polymer decomposition. Changes in the material properties also influence the MLR curves by switching the sample from thermally thick to thermally thin. The two numerical codes are generally in very good agreement for their predictions of the MLR versus time curves, except when in-depth absorption of radiation was important.

KEYWORDS:

Material flammability; heat release rate; polymer burning rate; fire simulation

1. INTRODUCTION

The prediction of fuel generation rates from burning solid materials is an important component of models for fire growth in buildings. Validation of these sub-grid models is often done via predictions of the mass loss rate for small samples subjected to a known radiant heat flux, in standard devices such as the cone calorimeter [1], the FM Global Fire Propagation Apparatus (FPA)[2], and other devices [3]. The mass loss rate of thermoplastics in these devices has been predicted analytically and numerically by various groups [4-12], subject to various simplifications.

Accurate prediction of the mass loss rate (MLR) requires the input data for the physical parameters of the polymer used in the model. In general, two approaches are being taken to supply these parameters: estimating them from the mass loss rate (or temperature) data obtained in the experiments to be modeled themselves [4, 7, 8] (sometimes with parameter optimization algorithms [13]), or measuring the individual parameters with separate experimental devices [5, 6, 9-12]. In either case, it is of value to understand the sensitivity of the mass loss rate to the individual parameters in the model. In the former case, such knowledge can allow one to design specific experimental runs for the most accurate extraction of certain parameters. In the latter case, knowing the sensitivity to each of the parameters can allow one to spend the limited resources on measuring the most relevant parameters, and to use simpler methods or estimations for parameters less important. Finally, mass loss rate curves and ignition times provided here can be used as an aid in interpreting cone calorimeter data. The present results are in the spirit of previous work in which the variation of mass loss rate with thickness [14], and with heat flux [15] have been

illustrated, and extend the phenomenological illustration to additional parameters as suggested by Schartel [16, 17].

Recently, Stoliarov et al. [18] have performed sensitivity calculations and reported the results of input parameter variation in terms of their effects on global parameters (such as the peak heat release, average heat release, etc.). The present investigation seeks to provide additional information beyond that in ref. [18], by presenting the data as the time-dependent mass loss rate. The influence of the parameters on the ignition time is also assessed here. In some cases, there are differences in the relative importance of the parameters between the present work and those in ref. [18], and as appropriate, the present work highlights how the external flux influences these conclusions. Finally, the collection of simulated mass loss curves can serve as a database illustrating the effects of changes in the parameters on the burning behavior, providing physical insight to developers of less flammable materials. Such calculations are easier and faster than the comparable experiments would be, and can be performed with individual parameters changed in isolation (in ways not always possible in experiments).

While much of the mass loss and ignition behavior of poly(methyl methacrylate) (PMMA) under constant heat flux is already known, often, not all of the physical effects are included in the analysis, and when many are, it is usually not possible to obtain closed-form solutions to the equations. Hence, it seemed of value to provide a compendium of the effects of multiple parameters on the thermal decomposition of PMMA. In the discussion, emphasis is placed on those conditions for which the behavior deviates from that expected based on simple models.

2. APPROACH

The time-dependent mass loss rate of a thermoplastic material subjected to a known radiant flux is simulated. Two numerical simulation codes describing the solid phase are used: the NIST Fire Dynamics Simulator (FDS 5.3.0. SVN 3193) [19] and the FAA Thermo-kinetic Model of Burning (ThermaKin) [20, 21]. Poly(methyl methacrylate) (PMMA) is selected as the base polymer for simulation, since it is a typical thermoplastic, is nearly a standard material in flammability studies, and its properties are relatively well studied. The simulations of the MLR are used in the present work to examine how variations in the input parameters affect the time-dependent MLR and the ignition time.

The input parameters in the models are shown in Table 1. The present study uses the nominal parameter values of Rhodes and Quintiere [8] as a base-case (column three), and these parameters are varied over the range of values as indicated in column four. Typically, the parameters in Table 1 are varied over a factor of five, about a factor of 2 to 2.5 above and below the nominal value. This is a somewhat larger range than experienced by typical polymers [18] and was selected to provide guidance in the event that new, composite polymers are produced with a wider range of properties than in the pure polymers. The Arrhenius parameters for the one-step decomposition reaction, E_a and A , were chosen to be 209 kJ/mol and $1.29 \times 10^{15} \text{ s}^{-1}$. These represent the mid-range of values reported in the literature [22], are close to some recent measurements [10, 23], and give an overall rate of 0.013 at 370 °C (approximately the decomposition temperature).

It should be noted that a range of values for PMMA properties have been reported in the literature. For example, the heat of reaction which can be inferred from the data in ref. [8] is 2000 kJ kg^{-1} , while other work gives values closer to 800 kJ kg^{-1} . [23, 24]. As described below, the heat of reaction has the largest effect on the mass loss rate of all the parameters. Hence, it is safer to consider the calculations in the present work to be for some arbitrary polymer which happens to have the properties in Table 1, rather than for PMMA. The material used for the present calculations is thus referred to below as the nominal *base-case polymer*.

The calculated curves of MLR versus time are characterized by the ignition time, average MLR, peak MLR, and time to peak MLR. In the present analyses, the ignition time τ_{ign} is defined as the time at which the mass loss rate has first achieved a value of $3 \text{ g s}^{-1} \text{ m}^{-2}$, as suggested in ref. [25]. While different critical mass loss rates have been observed for ignition and sustained burning [26], likely corresponding to the ignition and extinguishment, respectively, only a single value is used here. Since the MLR curves are steep at ignition and extinguishment, use of a single value has little effect on the overall trends. The average mass loss rate (MLR_{av}) is defined as the integral of the MLR versus time curve, between the time at which the flux is applied, and the time at which the MLR has decreased back to the mass loss at ignition ($3 \text{ g s}^{-1} \text{ m}^{-2}$). The parameters varied are the material properties: thermal conductivity (k), specific heat (c), extinction coefficient (α), heat of reaction (ΔH_{reac}), and the Arrhenius pre-exponential term (A) and activation energy (E_a) for the one-step material decomposition reaction. The experimental parameters varied are the external heat flux (EHF) and material thickness (S).

The magnitude of the EHF has a large effect on the burning behavior. While a range of values $0 \leq \text{EHF} \leq 50 \text{ kW/m}^2$ is typical for fire studies, we employ a range extending up to 200 kW/m^2 . These higher fluxes have recently been shown to lead to non-linear increases in the burning rate with applied flux, as well as increased importance of in-depth absorption of radiation during ignition [27, 28].

The most important material property affecting the burning rate of a polymer is its heat of gasification ΔH_g [29]. For a simple vaporizing material the heat of gasification can be described by

$\Delta H_g = \int_{T_a}^{T_v} c(T) dT + \Delta H_v$, in which the first part is the sensible heat in raising the material from the ambient temperature T_a up to the temperature at which it vaporizes T_v , and the second part is the heat of vaporization ΔH_v . This simple model is often used to describe more complicated solid materials which undergo endothermic pyrolysis reactions to form gas-phase products, by substituting a pyrolysis temperature T_p , and a heat of reaction ΔH_{reac} (i.e., a heat of decomposition in going from the solid directly to the gas-phase species at T_p).

$$\Delta H_g = \int_{T_a}^{T_p} c(T) dT + \Delta H_{\text{reac}}$$

Eq. 1

The assumption is often made that the material undergoes one-step decomposition to gaseous products, with either an infinite rate or a finite rate given by an Arrhenius rate expression. Methods have been developed to estimate the heat of gasification, either from measurements of the steady burning rate of the polymer exposed to different external fluxes (and called the “effective” heat of gasification, $\Delta H_g^{(\text{eff})}$ [4]), or by differential scanning calorimetry [30].

3. NUMERICAL CALCULATIONS

In the calculations with FDS or ThermaKin, the time-dependent 1-D heat transfer equation is solved for the solid phase, subject to mass (and energy) changes from reaction at any depth. There was only one solid-phase component, corresponding to the base-case polymer itself, with thermal conductivity and specific heat either given by a linear correlation [12], or by the average value between the initial temperature and the pyrolysis temperature. Thermal decomposition was via a one-step Arrhenius-type reaction (rate =

$A \exp(-E_a/RT)$) to a single gas-phase component, and there was no resistance to transport of the reacted polymer to the surface. Surface reflection and re-radiation are included. The initial temperature of the polymer was set to 293 K, the surface emissivity was set to 0.95 (following the value suggested by

Rhodes and Quintiere [8]), and the sample backside was insulated (adiabatic) with a reflectivity of 1 (i.e., a foil-wrapped sample). Currently, the back-side boundary condition in ThermaKin does not allow for reflected radiation, so the radiation which is not absorbed by the polymer passes through the backside and is lost.

In the ThermaKin calculations, the calculation was 1-D, the finite element objects were 5×10^{-5} m thick, and the time step was 0.025 s. Reducing these by a factor of four had no significant effect on the MLR, and only about a 3 % effect on the ignition time (which was more sensitive). In-depth absorption of radiation was treated using a random-sampling technique in which the energy is deposited at random locations in the 1-D sample, following a Beer's law attenuation, with energy emission then following from the same location. Because of the discrete (and random) treatment of radiation, the calculated mass loss (sampled every 2 seconds) had fluctuations, so the data were smoothed (running average) for 8 s.

In the FDS calculations, all gas-phase reaction was turned off by setting the mass fraction of O₂ in the air to 0.01 and a minimum gas-phase mesh was used. The time step was set to 0.1 s, except for ignition time calculations, for which it was set to 0.005; this value yielded ignition times within 1 % of those with a time step of 0.01 s. The parameters used for the solid-phase calculation (which has adaptive gridding) are: STRETCH_FACTOR = 2.0, CELL_SIZE_FACTOR = 0.06, and REGRID_FACTOR=1.0, which provide the most grid cells, of the most non-uniform size, and which are re-gridded the most often. The initial gridding gave a smallest grid size of 1.67×10^{-5} m to 3.33×10^{-5} m (depending upon the case).

The performance of ThermaKin has recently been validated in predictions of the gasification rate of poly(methylmethacrylate), high-impact polystyrene (HIPS), and high density polyethylene (HDPE) [12], and it is used predominantly in the present work. Calculations with FDS are provided for comparison purposes. As further validation of both the numerical calculations and the parameters used in this study, the calculated steady mass loss rate for non-flaming pyrolysis at an applied external heat flux of 21 kW/m² can be compared with the experimental values of Rhodes [31] ($5 \text{ g s}^{-1} \text{ m}^{-2}$). The calculated steady mass loss rate (for the base-case conditions of Table 1) is $5.9 \text{ g s}^{-1} \text{ m}^{-2}$, which is easily within the experimental uncertainties reported in ref. [31].

4. RESULTS

4.1. Mass Loss Rate vs. Time

External Heat Flux (EHF)

The external heat flux (though not a material property), is one of the most important parameters affecting a materials' fire behavior; hence, we first illustrate the effect of this parameter on the mass loss rate.

Figure 1 shows mass loss rate for the base-case polymer with the nominal properties of Table 1 exposed to an EHF of (21, 50, 100, 150, or 200) kW/m². Simple analytical models of the thermoplastic burning rate [4] show that the steady mass loss rate \dot{m}'' is given by

$$MLR = \frac{dm''}{dt} = \dot{m}'' = \frac{\dot{q}_{net}''}{\Delta H_g} \quad \text{Eq. 2}$$

where \dot{q}_{net}'' is the net external heat flux, and $\dot{q}_{net}'' = \dot{q}_{fl}'' + \dot{q}_{ext}'' - \dot{q}_{loss}''$, in which \dot{q}_{fl}'' is the heat feedback from the flame to the surface, \dot{q}_{ext}'' is the external heat flux, and \dot{q}_{loss}'' is the heat lost from the surface by convection and radiation, as well as by conduction into the unburned material. The burning time t_{burn} is

given by $\rho S \Delta H_g / \dot{q}_{net}''$, where ρ and S are the density and thickness of the 1-D sample. Since the heat losses and flame heat feedback are relatively constant as compared to the changes in the external flux \dot{q}_{ext}'' , the mass loss rate is approximately proportional to both the net and incident heat flux (as indicated in Figure 1), and the burning time is inversely proportional to \dot{q}_{ext}'' .

The thermal thickness (δ) of a material (with regard to mass loss) under steady surface regression (without in-depth absorption of radiation) can be given [32] by

$$\delta = \frac{2k\Delta H_g}{c\dot{q}_{net}''} . \quad \text{Eq. 3}$$

A sample is thermally thin if $S/\delta \ll 1$ and thermally thick if $S/\delta > 1$. For values of S/δ less than, but close to, unity the sample is often described as thermally “intermediate” thick, and displays a continuous variation in the properties between those of the limits. For the nominal the base-case polymer properties, the thermal penetration depth is about (45, 13.7, 6.3, 4.1, and 3.0) mm for incident fluxes of (21, 50, 100, 150, and 200) kW/m² (assuming a surface temperature (T_s) of 352 °C and no convective losses). Including the surface convective heat losses, about 3 kW/m² for the base-case polymer, would increase the thermal penetration depth by about (35, 9, 4, 2, and 2) % for these incident fluxes. The low flux case (21 kW/m²) in Figure 1 is thermally thin, while the others are thermally thick. Another way to show the thin vs. thick behavior is to normalize the MLR curves by the steady-burning value (Eq. 2) for the mass loss rate ($\dot{q}_{net}'' / \Delta H_g$), and for the burning time $\rho S \Delta H_g / \dot{q}_{net}''$. This is shown in the inset of Figure 1; the curves are reasonably coincident for the thermally thick cases, but deviate for the thinner cases. (Note that in general, the heat loss term \dot{q}_{loss}'' above includes the conductive heat loss term into the unburned sample. Using the ThermaKin simulations below, these are estimated, for the steady burning region of the mass loss curve, to be (2.0, 5.9, 10.3, 13.3., and 15.5) kW/m² for incident fluxes of (21, 50, 100, 150, and 200) kW/m², respectively. While these losses can be included in the value of \dot{q}_{net}'' used for the normalization of MLR and burning time, they were not included in normalized plot inset in Figure 1, since usually they are not known a priori. Calculations which included these losses indicated a secondary effect on the qualitative features shown in the inset.)

The results in Figure 2 illustrate that for a 25.4 mm-thick sample of the base-case polymer, the sample response for fluxes in the EHF range of 21 kW/m² to 75 kW/m² will readily shift from thermally thick to thermally thin as the various parameters are changed. This will become apparent as the mass loss rate curves are discussed below. (Note that the absorption coefficient would enter in the denominator of Eq. 3 above, since a low value of α acts like high thermal conductivity, sending heat more readily in-depth in the sample.) For all values of the flux, the peak MLR is 38 % to 45 % higher than the average MLR, and the time to peak MLR scales with the burning time.

Sample Thickness

Sample thickness (a specimen property) greatly affects the burning behavior.

Figure 2 shows the mass loss rate of the base-case polymer at EHF values of 21 kW/m² (left frame) and 100 kW/m² (right frame) for sample thickness of (2, 4, 8, 15, and 32) mm. At the low flux, the sample is always thermally thin; at the higher flux, the behavior becomes thermally thin as the sample thickness decreases to about 8 mm, which is consistent with the numbers given above, as well as with the recent

experimental data of Schartel and Weiß [33]. Both the average and peak MLR are nearly unchanged as S decreases, except for the thinnest samples for which both the peak and the average MLR drop off, the average somewhat faster, about (30, 40, 48, and 56) % lower at (21, 50, 100, and 200) kW/m^2 , for the 2 mm sample as compared to the 32 mm sample. This is due to insufficient thickness for complete absorption of the thermal radiation. For example, the dotted lines in Figure 2 illustrate the results for $S = 2$ mm and $\alpha = 50000 \text{ m}^{-1}$ (surface absorption), for which the peak and average MLR are restored closer to the values at larger S , only (-5, 2, 7, and 16) % lower for the 2 mm sample as compared to the 32 mm sample at (21, 50, 100, and 200) kW/m^2 , respectively.

Heat of Reaction, ΔH_{reac}

The heat of reaction has the largest effect on the mass loss rate of any material property. Figure 3 shows the mass loss rate as a function of time for the base-case polymer with an EHF of a.) 21 kW/m^2 and b.) 100 kW/m^2 . The different curves in the figures show the results for $\Delta H_{\text{reac}} = (1000, 2000, 3000, 4000, \text{ and } 5000) \text{ kJ kg}^{-1}$. For higher flux, the behavior is always thermally thick, while for low flux, the behavior is thermally thin for all values of ΔH_{reac} except 1000 kJ kg^{-1} , for which it's thermally intermediate thick. At either 21 kW/m^2 or 100 kW/m^2 , and the lowest value of ΔH_{reac} , (upper most curves), the peak heat release is much higher than the average heat release as compared to the other cases of ΔH_{reac} . This is because for low ΔH_{reac} , the sensible part becomes a larger fraction of ΔH_g , and the transient effect from the pre-heating of the in-depth layers of the polymer due to thermal diffusion becomes larger relative to the enthalpy change due to decomposition. For the nominal polymer properties, the algebraic relationship in Eq. 2 shows $\text{MLR}_{\text{av}} \sim \Delta H_{\text{reac}}^n$, where $n = -0.72$ (instead of -1, because ΔH_{reac} is only part of ΔH_g). This value of n is close to the behavior shown in Figure 3, where the value of n ranges from -0.64 to -0.80, depending upon EHF.

Table 2 (discussed in more detail in section 4.4 below) provides the power-law exponent for the relation $y \sim x^n$ (where $y = \text{MLR}_{\text{av}}$ or τ_{ign} , and $x = \Delta H_{\text{reac}}, c, \alpha,$ or k). To obtain the values of n given in Table 2, either τ_{ign} or MLR_{av} is calculated for a range of values of the dependent variable (using ThermaKin for the given conditions), and then the power-law exponent n is determined with a least-squares curve fit.

Activation Energy, E_a

Variations in the activation energy of the the base-case polymer decomposition reaction can increase or decrease the MLR, with both the magnitude and direction depending upon the value of the external heat flux. (All of the above results are for $E_a = 209 \text{ kJ mol}^{-1}$.) In the present simulations, the pre-exponential factor A was increased as E_a was increased, to maintain a constant value of the rate (0.013 s^{-1} at $370 \text{ }^\circ\text{C}$), (so that the effect of the activation energy can be determined independent of the overall rate). Figure 4 shows the mass loss rate with time for the base-case polymer; each frame a.), b.), c.) and d.) shows the result for (21, 50, 100, and 200) kW/m^2 , respectively, while the different curves on each frame show the mass loss for a different value of the activation energy[†]. As illustrated, there exists an external heat flux (e.g., 50 kW/m^2 for which the value of activation energy does not affect the mass loss rate curves (and this heat flux value changes somewhat as the polymer properties, such as the thermal conductivity, and specific heat are varied). At external heat fluxes lower than 50 kW/m^2 , lower values of E_a give higher mass loss rates, while at higher heat fluxes, the opposite is true. This is also the case for the average values of MLR: with the highest value of E_a , the average MLR are about 0.8, 1.01, 1.08 and 1.08 those with the lowest E_a , for EHF, for (21, 50, 100, and 200) kW/m^2 , respectively. Examination of the

[†] Note: the random absorption algorithm in ThermaKin was turned off for these calculations to remove the noise in the output and more clearly show the effects of E_a . The results with the random algorithm turned on are qualitatively the same.

calculation output indicates that this effect of E_a on the MLR is due to changes in the temperature profile in the the base-case polymer with mass loss rate: at low mass loss rate (i.e., low EHF), the temperature gradient is mild, leading to lower surface temperatures and higher sub-surface mass loss, which give larger mass losses at low values of E_a . Conversely, at high mass loss rates (or external heat flux), the high external heat flux leads to high surface temperatures which produce comparatively higher reaction rates at high activation energies.

Thermal Conductivity, k

The effect of changes in the thermal conductivity of the polymer on the mass loss rate as a function of time is shown in Figure 5 for an external heat flux of 21 kW/m² (frame a.) and 100 kW/m² (frame b.). The results in Figure 5 were calculated using the nominal property values Table 1, and the five curves in each frame correspond to the five values of the thermal conductivity (0.1 to 0.5) W m⁻¹ K⁻¹. The MLR_{av} is nearly identical regardless of k (at all values of EHF from 21 kW/m² to 200 kW/m²), as expected from Eq. 2, in which k does not appear (since conductive “losses” do not apply when the burning is averaged over the entire time of flux exposure, with an adiabatic back surface, as done here). The time varying behavior, however, is different. At low EHF, the low conductivity case is thermally thick, while the high conductivity case is thermally thin. At low flux, the time to peak MLR is about half for the high-conductivity case as compared to the low (reflecting the thin behavior); while at high flux, the time to peak MLR is only slightly lower (10 %) for the high value of k . (Of course, for the low-flux condition, the time to peak MLR is highly dependent upon the threshold for defining the peak. In the discussion here, reaching a value within a few percent of the maximum is considered to be reaching the “peak” value.) For either low or higher flux, the peak heat release is only a few percent lower for $k=0.1$ compared to $k=0.5$.

Absorption Coefficient, α

Higher transmission of IR through the polymer (lower values of the absorption coefficient α) creates behavior similar to higher thermal conductivity, namely increased thermally thin behavior. Figure 6 a.) 21 kW/m² and b.) 100 kW/m² show the effect for ($\alpha = 200, 400, 800, 1200, 50,000$) m⁻¹ as different lines in each frame. For all values of α , the behavior is thermally thin at low EHF, and thick at higher EHF, and for both values of EHF, the behavior becomes more thermally thin as α decreases. At low flux, the peak MLR is about 13 % *lower* for surface absorption than for $\alpha=200$ m⁻¹, whereas for higher flux, the peak MLR is about 2 % *higher* for the surface absorption. The average MLR is significantly lower for the low α cases: generally about 20 % lower for $\alpha=200$ m⁻¹ (and 10 % for $\alpha=400$ m⁻¹) as compared to 50000 m⁻¹ for any flux. As with the thermal conductivity, the time to peak MLR is shorter for cases where energy penetrates better into the sample (higher k or lower α). The very gradual decrease in the MLR at the end of the burning period when $\alpha=200$ m⁻¹ is a result of the remaining sample being thinner than the characteristic thermal radiation penetration depth ($1/\alpha$, or 5 mm), so that not all of the radiant energy is absorbed, decreasing MLR. It should be noted that this behavior is significantly affected by the model’s treatment of the backside boundary condition (absorbing or reflecting), which is different in FDS and ThermaKin, as discussed above.

Specific Heat, c

The effects of variations in the specific heat on the time history of the mass loss rate are shown in Figure 7 a.) for 21 kW/m² and b.) 100 kW/m². The different curves in each frame correspond to $c = (1, 2, 3, 4,$ and 5) kJ kg⁻¹ K⁻¹. The peak MLR is not much affected by c at low EHF (only about 4 % lower at $c = 5$ kJ kg⁻¹ K⁻¹ as compared to $c = 1$ kJ kg⁻¹ K⁻¹); while at high EHF, it’s about 10 % lower. On the other hand, the average MLR is about 35 % lower (at all values of EHF except 21 kW/m², where it’s 41 % lower) at c

= 5 kJ kg⁻¹ K⁻¹ as compared to $c = 1 \text{ kJ kg}^{-1} \text{ K}^{-1}$. This effect is due to the contribution of c to ΔH_g , and the effect of ΔH_g on the MLR, as described Eq. 2. (Note that in the present calculations, the variation in c from 1 kJ kg⁻¹ K⁻¹ to 5 kJ kg⁻¹ K⁻¹ raises the heat of gasification ΔH_g by about a factor of two.) From the average values of MLR calculated from Figure 7, the sensitivity of MLR_{av} to c is determined. As was done above for ΔH_{reac} , the sensitivity of the MLR to c is determined; MLR_{av} $\sim c^n$ with n varying from -0.26 to -0.32, depending upon EHF; the algebraic relation in Eq. 2 predicts that $n=-0.30$, in good agreement with the detailed numerical results predicted here. As for the time-dependent behavior, higher specific heat affects the MLR in the same way as lower conductivity or higher absorptivity (see Eq. 3), leading to thermally-thick behavior. Results for other heat fluxes (50, 150, and 200) kW/m² show the same trends, and the thermally-thick behavior is accentuated as the flux goes up.

Constant Values of k or c

Both the specific heat and the thermal conductivity of polymers vary with the temperature—which increases significantly as the polymer heats, melts, and decomposes. In the calculations above, the temperature-dependent values were used in the simulations (except when c or k themselves were varied). It is of interest, however, to determine how the results would differ when using a single value of k or c , evaluated at the average polymer temperature (between ambient and the decomposition temperature). The MLR as a function of time was calculated using the average value of either k or c , and these were normalized by the results of MLR calculations obtained using the temperature-dependent values of c and k . The error imposed by using the average value is not large. For example, for constant c and external heat fluxes of up to 100 kW/m², the mass loss rate is at most, 2 % to 5 % higher at some times, than with the temperature dependent value (for all values of E_a), while for high external heat flux (150 kW/m² or 200 kW/m²) using a constant c gives less than 2 % error. For a constant value of k , the transient behavior (for example at low flux, or at higher flux and towards the end of the mass-loss period) of the mass loss rate can about 5 % higher than the mass loss rate calculated with a temperature dependent k . The steady mass loss rates are generally within 1 %, except at high flux, where it can be 1 % high or 2 % low, depending upon E_a . The average mass loss rate is also not greatly affected by the use of constant k or c . For example, for all values of EHF and E_a , using constant k gives average MLRs within 1 % of those using variable k , (except the cases of EHF = 200 kW/m², and $E_a = 97 \text{ kJ kmol}^{-1}$, and EHF = 150 kW/m² and $E_a = 418 \text{ kJ kmol}^{-1}$, which yields about a 5 % difference. Using constant c gives average MLRs within 3 % of the results with variable c , for all values of E_a , except at EHF = 200 kW/m², for which the results using average c can be 1 % to 10 % low (depending upon E_a). These results are consistent with those of Steckler et al.[6] who found close agreement between the time-varying mass loss rate using constant values of k or c (evaluated at a mean temperature) as compared to using temperature-dependent values. The significance of the present results are that the conclusion of Steckler et al., for a single case of 40 kW/m², surface absorption, and infinite reaction rate, have been verified for a wider range of E_a and incident flux.

4.2. Ignition Time

Simple one-dimensional heat transfer models predict the ignition time for thermally thick or thin materials [34]. The characteristic thermal conduction length δ_t for thick materials is given by $\delta_t = \sqrt{kt/\rho c}$, in which in which t is the exposure time. In the absence of convective and radiative heat losses, thin materials, $S/\delta \leq 1$, have an ignition time given by:

$$\tau_{\text{ign}} = \rho c S \frac{(T_{\text{ig}} - T_0)}{\dot{q}_{\text{ext}}^n} \quad \text{Eq. 4}$$

and thick materials:

$$\tau_{ign} = \frac{\pi}{4} k \rho c \frac{(T_{ig} - T_0)^2}{\dot{q}_{ext}''^2}. \quad \text{Eq. 5}$$

Below, these analytic predictions are compared to the numerical results.

As noted above, the ignition time is calculated from the numerical MLR predictions as the time at which the mass loss rate reaches a critical value ($3 \text{ g s}^{-1} \text{ m}^{-2}$). The effect of parameter variations on these numerically-determined ignition times are summarized in Figure 8 (a.), b.), c.), and d.) and Figure 9, which show the ignition time as a function of k , c , α , ΔH_{reac} , and S , respectively. In each figure there is a grouping of results for each value of the external heat flux, and the different color lines show the variation with E_a . As indicated, the ignition time is strongly dependent upon the external heat flux, and mildly dependent upon E_a , except for cases of low EHF (21 kW/m^2), for which E_a can make a difference of a factor of three to seven. The variations in magnitude of the parameters k , c , α , and ΔH_g in the figures is about a factor two above and two below the nominal value for the base-case polymer. Hence, the slopes of the lines give a qualitative estimate of the sensitivity of the ignition time to those parameters. Based on the simple thermal conduction analysis above, for the nominal conditions of Table 1, the 25.4 mm thick sample is thermally thick with respect to ignition for τ_{ign} less than 7100 s. Hence, for all conditions shown in Figure 8 the sample is thermally thick with respect to ignition, except the lowest flux, at which the behavior can be thin depending upon the parameter value and the activation energy assumed.

Effect of \dot{q}_{ext}''

In Figure 8(a.) and b.) for k and c , τ_{ign} is proportional to $1/\dot{q}_{ext}''^2$, following Eq. 5 above for thick materials (which is the case for these conditions). For varying α (Figure 8c), the results at $\alpha=960 \text{ m}^{-1}$ (the nominal value) also give $\tau_{ign} \sim 1/\dot{q}_{ext}''^2$, while optically thin material ($\alpha=200 \text{ m}^{-1}$) has $\tau_{ign} \sim 1/\dot{q}_{ext}''^{1.5}$ and surface absorption shows $\tau_{ign} \sim 1/\dot{q}_{ext}''^{2.66}$.

k

As shown in Figure 8a, a five-fold increase in thermal conductivity generally causes about a two-fold increase in the ignition time, with a larger effect (3x) at EHF= 21 kW/m^2 as compared to (1.5x) at EHF= 200 kW/m^2 . That is, $\tau_{ign} \sim k^{0.25}$ to $\tau_{ign} \sim k^{0.67}$, a weaker dependence than the linear behavior expected from Eq. 5, likely resulting from energy penetration dominated by thermal radiation transport for these short times, diluting the effect of thermal conduction.

c

In Figure 8b, a five-fold increase in the specific heat is shown to result in a five-fold increase in the ignition time for all values of EHF except the lowest (relatively independent of E_a), essentially following the thermally thick prediction ($\tau_{ign} \sim c^1$) in Eq. 5 above. For the low flux conditions EHF= 21 kW/m^2 , the material is still thermally thick and $\tau_{ign} \sim c^{1.3}$ (and there is a strong dependence on E_a).

α

The absorption coefficient has very little effect on τ_{ign} at EHF= 21 kW/m^2 . At high EHF (100 to 200) kW/m^2 , however, $\tau_{ign} \sim \alpha^{-0.72}$, so that the $\alpha=200 \text{ m}^{-1}$ case has an ignition time about ten times longer than with $\alpha=50000 \text{ m}^{-1}$, as recently discussed by Jiang et al [28].

ΔH_{reac}

The heat of reaction ΔH_{reac} has almost no effect on the ignition time at a given flux, except at very low incident heat fluxes; i.e., very near to the critical heat flux for ignition, where the ignition times are so long that the reaction rates (albeit slow) have an effect on the critical mass flux for ignition.

Thickness

The sample thickness affects the ignition time primarily for thinner samples. As shown in Figure 9 a.) for $\alpha=960 \text{ m}^{-1}$, and b.) $\alpha=50000 \text{ m}^{-1}$, for either value of α , and higher values of EHF (100 to 200) kW/m^2 , the thickness has generally less than a 10 % effect on τ_{ign} , as long as the sample is 4 mm thick or greater. At 2 mm thickness, the sample is thermally thin, and the dependence of τ_{ign} on \dot{q}_{ext}'' follows Eq. 4 above for thin materials, for $\text{EHF} \geq 50 \text{ kW/m}^2$. For very low EHF (21 kW/m^2), the effects of slow reaction and of surface re-radiation losses affect the ignition time [35], so Eq. 4 and Eq. 5 are not accurate.

Effects of Constant c or k

The ignition time is only moderately affected by using constant values of the thermal conductivity or specific heat of the polymer. A constant value of c yields an ignition time about 10 % shorter than using the temperature-dependent value, for all values of the external heat flux, and this ratio is only affected slightly by variations in E_a . For constant k , the ignition time is again lower, by about 5 %, for all external heat fluxes independent of E_a , except at 21 kW/m^2 , at which it can be either 6 % higher or lower, depending E_a .

4.3. Comparison of ThermaKin and FDS Results

All calculations in the present work were performed with both ThermaKin and FDS; however, due to space limitations, only the former are presented. For the nominal values of k , c , S , and ΔH_{reac} , and surface absorption of thermal radiation, the entire time-dependent MLR curves obtained with the two codes are in within 3 % of each other for the range of EHF and E_a in Table 1, except the case of $E_a=837 \text{ kJ/mol}$ and $\text{EHF}=200 \text{ kW/m}^2$, for which the difference was 6 %. Using the nominal value of the absorption coefficient (960 m^{-1}), the general behavior is the same, as evidenced by very close values of average and peak MLR, but the shape of the curves differ slightly. Examination of other solutions with lower values of α indicates that the disagreement becomes worse as α decreases. For the ignition time, when surface absorption is assumed, and over the range of conditions of Table 1, τ_{ign} using FDS is always within 10 % of that from ThermaKin. However, when $\alpha=960 \text{ m}^{-1}$, the FDS prediction is about 46 % higher than the ThermaKin at $\text{EHF}=21 \text{ kW/m}^2$, and 22 % lower at $\text{EHF}=200 \text{ kW/m}^2$. The different treatment of the in-depth absorption of radiation by the two codes is likely responsible for the differences observed, and work is continuing to understand the reasons.

4.4. Summary of Dependence of MLR and Ignition time on Material Properties

The effect of the parameters ΔH_{reac} , k , α , and c on τ_{ign} and MLR_{av} are provided in

Table 2, which gives the power-law dependence of τ_{ign} or MLR_{av} on each of the parameters. For example, $\tau_{\text{ign}} \sim \Delta H_{\text{reac}}^n$, with $n=0.02$ at $\text{EHF}=200 \text{ kW/m}^2$, and increasing to $n=0.14$ at $\text{EHF}=50 \text{ kW/m}^2$; at very low EHF (21 kW/m^2), $n=1.70$. That is, the ignition time is typically not dependent upon ΔH_{reac} , except at low flux. Also given in Table 2 are the expected values of n based on the simple algebraic model in Eq. 2. (Note that the expected dependence of τ_{ign} and MLR_{av} on α are not given in Table 2. The effect of in-depth absorption of radiation shows up as changes to the surface temperature, and hence the radiative heat loss term. While analytic solutions are available [28], they do not have a simple form.) The ignition time is somewhat dependent upon k , increasingly so at lower flux, with $n=0.28$ or 0.71 at $\text{EHF}=(200 \text{ and } 21) \text{ kW/m}^2$, respectively. The ignition time is approximately proportional to c , with n close to unity, except at $\text{EHF}=21 \text{ kW/m}^2$, for which $n=1.3$. The effect of α on τ_{ign} has the opposite trend, with little dependence at low flux ($n=-0.03$), but increasing importance at higher flux ($n=-0.54$ and -0.77 , at $\text{EHF}=50 \text{ kW/m}^2$ and 200 kW/m^2). For comparison, the simple thermal conduction model predicts $n=1$ for variation of τ_{ign} with k and c , and $n=0$ for ΔH_{reac} . That is, the dependence calculated here is greater for ΔH_{reac} , especially at low flux, about as expected for c (and somewhat greater at low flux), and significantly less for k , increasingly so at lower flux. Variation in α can have substantial effect on τ_{ign} at high flux.

As described above, MLR_{av} is roughly inversely related to ΔH_{reac} , with $n=-0.64$ to -0.80 , mildly related to c or α , with $n=-0.27$ to -0.32 , or $n=0.016$ to -0.14 , respectively, and nearly unrelated to k with $n=-0.004$ to -0.010 . Expected values of n for MLR_{av} based on a simple heat balance model (Eq. 2) are -0.72 , -0.30 , and 0 for ΔH_{reac} , c , or k . Hence, for these three parameters, the simple relationship gives a good estimate of their relative influence on MLR_{av} . The effects of in-depth absorption on MLR_{av} can be significant.

Numerical values of the peak MLR and the time to peak MLR were not calculated since these values are highly dependent upon both the threshold for defining the peak (e.g., region of 95 % of peak, etc.), as well as the thermally thick or thin behavior, which switches readily as the physical properties are changed. Instead, the qualitative behavior with respect to these metrics are provided.

Table 3 summarizes the results of the variation in each of the material properties on the mass loss. The influence is characterized by the shape of the mass loss rate (MLR) curve, average MLR, peak MLR, time to peak MLR, and ignition time. In the table, double check marks indicate a large effect on that metric, while single check marks indicate a moderate effect; and a gray single check, even less effect. A blank means no significant effect. Subscripts indicate the conditions (e.g., LF: low flux, HF, high flux) to which the importance is limited. (Note that these qualitative rankings supplement the quantitative results in Table 2.) As shown, the heat of reaction ΔH_{reac} is the most important parameter, followed by the thickness S and specific heat c . The absorption coefficient and the conductivity behave similarly, showing an effect on the shape of the MLR, as well as the time to peak at low flux, and on the ignition time for moderate and high fluxes (α also affects the average MLR at high flux).

For the conditions assumed here, the activation energy of the decomposition step is the least important parameter, mildly affecting the shape of the MLR curve at high or low flux, and the average MLR and ignition time at low flux. This result is in contrast to the finding of Stoliarov et al. [18], in which the kinetic parameters were found to be, by far, the most important of those examined. This difference is likely a result of the range over which E_a and A were varied in the two works. In ref. [18], the bounds of E_a and A considered were taken to represent all polymers. This produced a variation in the overall decomposition rate ($A \exp(-E_a/RT)$, described in Table VI of [18], of about 4×10^8 (assuming $T=673 \text{ K}$); conversely, for a decomposition rate of 0.1 s^{-1} , the variation in the A and E_a in Stoliarov et al. [18] requires a decomposition temperature ranging from 416 K to 786 K . In the present work, the kinetic parameters were intended to represent only the range of those measured for PMMA (and one very high

value for comparison), and the effect of *only* E_a was examined. Hence, the overall rate of decomposition was held constant (0.013 s^{-1} at $370 \text{ }^\circ\text{C}$), while E_a was varied from 97 kJ/mol to 837 kJ/mol which yielded a much smaller influence of E_a/A on MLR.

For the polymer modeled here, the behavior is often thermally intermediate thick, as described above. As a result, varying the material properties often leads to changes in the time-varying MLR curve which are due to switching of the behavior from thick to thin (or visa versa). This has been discussed by Delichatsios et al. [36] in the context of ignition. It is also of value to keep this in mind when interpreting the *mass loss rate data* for materials for which some property change has been made, for example in determining the mode of action of polymer fire retardant additives.

5. CONCLUSIONS

The time varying mass loss rate for the base-case polymer with a range of physical properties has been predicted numerically. The variations in the average mass loss rate due to changes in the heat of reaction, specific heat, and thermal conductivity are well predicted by the simple algebraic relations based on energy balance at the surface. The ignition time is influenced by heat of reaction and the specific heat as expected based on simple thermal conduction models, although their effect is somewhat greater than expected at low flux. The variation in the ignition time caused by changes to the thermal conductivity is about one third the expected value based simple theory, most likely due to the competing effect of in-depth absorption as a mechanism for heat transfer into the sample. The material's absorption coefficient for IR can influence the shape of the MLR curve significantly, and the ignition time substantially.

While most of the properties studied here (\dot{q}_{ext}'' , k , c , α , ΔH_{reac} , and S ,) have varying effect on the mass loss rate and ignition time, they all affect the thermal thickness of the material and hence, have the potential to switch the behavior from thermally thick to thermally thin, and consequently change the MLR curves both qualitatively and quantitatively. When making changes to a polymer to promote fire-safe behavior, care should be taken in interpreting experimental data to insure that the material property being changed is not just changing the thermal thickness of the material. That is, role of the material thickness should be understood both with regard to inferring the mode of action of a fire retardant additive, as well as understanding the effect of the material thickness on the fire behavior of the material. Finally, the heat of reaction is the most important parameter of those examined, and needs to be determined most accurately.

6. ACKNOWLEDGEMENTS

The author is grateful to Kevin McGrattan and Simo Hostikka for aid in using FDS, and Stanislav Stoliarov and Richard Lyon for aid in using ThermaKin. Takashi Kashiwagi at NIST originally suggested this line of research, and helpful conversations with him contributed throughout. This research was supported by NIST and NASA's Office of Biological and Physical Research.

7. REFERENCES

1. Standard test method for heat and visible smoke release rates for materials and products using an oxygen consumption calorimeter. (*ASTM E 1354-08a*), American Society for the Testing of Materials, Philadelphia, PA, 2008.
2. Standard test methods for measurement of synthetic polymer material flammability using a fire propagation apparatus. (*ASTM E2058-06*), American Society for the Testing of Materials, Philadelphia, 2006.
3. Austin PJ, Buch RR, Kashiwagi T. Gasification of silicone fluids under external thermal radiation part I. Gasification rate and global heat of gasification. *Fire and Materials* 1998; **22**(6):221-237.
4. Tewarson A, Pion RF. Flammability of Plastics .1. Burning Intensity. *Combustion and Flame* 1976; **26**(1):85-103.
5. Vovelle C, Delfau JL, Reuillon M, Bransier J, Laraqui N. Experimental and numerical study of the thermal degradation of PMMA. *Combustion Science and Technology* 1987; **53**(2-3):187-201.
6. Steckler, K. D., Kashiwagi, T., Baum, H. R., and Kanemaru, K. Analytic model for transient gasification of non-charring thermoplastic materials. Elsevier Applied Science, London, 1991; 895-904.
7. Hopkins D, Quintiere JG. Material fire properties and predictions for thermoplastics. *Fire Safety Journal* 1996; **26**(3):241-268.
8. Rhodes BT, Quintiere JG. Burning rate and flame heat flux for PMMA in a cone calorimeter. *Fire Safety Journal* 1996; **26**(3):221-240.
9. Staggs JEJ, Whiteley RH. Modelling the combustion of solid-phase fuels in cone calorimeter experiments. *Fire and Materials* 1999; **23**(2):63-69.
10. Nicolette, V. V., Erickson, K. L., and Vembe, B. E. Numerical simulation of decomposition and combustion of organic materials. Proceedings of Interflam 2004, 10th International Conference on Fire Science and Engineering, Interscience Communications Ltd. London, 2004;
11. Lautenberger, C. and Fernandez-Pello, A. C. Approximate analytical solutions for the transient mass loss rate and piloted ignition time of a radiatively heated solid in the high heat flux limit. Fire Safety Science-Proceedings of the Eighth International Symposium, International Association for Fire Safety Science, 2005; 445-456.
12. Stoliarov SI, Crowley S, Lyon RE, Linteris GT. Prediction of the burning rates of non-charring polymers. *Combustion and Flame* 2009; **156**:1068-1083.
13. Kim, E., Lautenberger, C., and Dembsey, N. A. Property estimation for pyrolysis modeling applied to polyester FRP composites with different glass contents. 11th International Conference and Exhibition, Interscience, London, 2009; 87-102.
14. Paul K. unpublished data, RAPA Technology, Shawbury, England, as cited in: SFPE Handbook, Babrauskus, Chapter 3-1. 2002.

15. Babrauskas V, Grayson SJ. (eds). *Heat release in fires*. Elsevier: Amsterdam, 1992; 375-422.
16. ScharTEL B, Bartholmai M, Knoll U. Some comments on the use of cone calorimeter data. *Polymer Degradation and Stability* 2005; **88**(3):540-547.
17. ScharTEL B, Hull TR. Development of fire-retarded materials - Interpretation of cone calorimeter data. *Fire and Materials* 2007; **31**(5):327-354.
18. Stoliarov SI, Safronava N, Lyon RE. The effect of variation in polymer properties on the rate of burning. *Fire and Materials* 2009; **33**:257-271.
19. McGrattan KB, Klein B, Hostikka S, Floyd J. Fire dynamics simulator (version 5) user's guide. *NIST Special Publication 1019-5*, National Institute of Standards and Technology, Gaithersburg, MD, 2007.
20. Stoliarov SI, Lyon RE. Thermo-kinetic model of burning. *Federal Aviation Administration Technical Note DOT/FAA/AR-TN08/17*, Federal Aviation Administration, Atlantic City, NJ, 2008.
21. Stoliarov, S. I. and Lyon, R. E. Thermo-Kinetic model of burning for pyrolyzing materials. Proceedings of the Ninth International Symposium on Fire Safety Science, Interscience Communications, Ltd., London, 2008; 1141-1152.
22. Arisawa H, Brill TB. Kinetics and mechanisms of flash pyrolysis of poly(methyl methacrylate) (PMMA). *Combustion and Flame* 1997; **109**(3):415-426.
23. Stoliarov SI, Crowley S, Lyon RE, Linteris GT. Prediction of the burning rates of non-charring polymers. *Combustion and Flame* 2009; **156**(5):1068-1083.
24. Staggs JEJ. The heat of gasification of polymers. *Fire Safety Journal* 2004; **39**(8):711-720.
25. Panagiotou, T. and Quintiere, J. G. Generalizing Flammability of Materials. Interflam 2004, Interscience Communications Ltd., London, 2004; 895-905.
26. Lyon RE, Quintiere JG. Criteria for piloted ignition of combustible solids. *Combustion and Flame* 2007; **151**(4):551-559.
27. Beaulieu PA, Dernbsey NA. Flammability characteristics at applied heat flux levels up to 200 kW/m². *Fire and Materials* 2008; **32**(2):61-86.
28. Jiang FH, de Ris JL, Khan MM. Absorption of thermal energy in PMMA by in-depth radiation. *Fire Safety Journal* 2009; **44**(1):106-112.
29. Linteris GT, Gewuerz L, McGrattan KB, Forney GP. Modeling Solid Sample Burning with FDS. *NISTIR 7178*, National Institute of Standards and Technology, Gaithersburg MD, 2004.
30. Stoliarov SI, Walters RN. Determination of the heats of gasification of polymers using differential scanning calorimetry. *Polymer Degradation and Stability* 2008; **93**(2):422-427.
31. Rhodes BT. Burning rate and flame heat flux for PMMA in the cone calorimeter. *NIST-GCR-95-664*, National Institute of Standards and Technology, Gaithersburg, MD, 2009.

32. Quintiere JG, Iqbal N. An approximate integral model for the burning rate of a thermoplastic-like material. *Fire and Materials* 1994; **18**:89-98.
33. Schartel B, Weiss. Temperature inside burning polymer specimens: Pyrolysis zone and shielding. *Fire and Materials* 2009;
34. Drysdale D. *An Introduction to Fire Dynamics*. John Wiley and Sons: Chichester, England, 1998.
35. Mikkola E, Wichman IS. On the Thermal Ignition of Combustible Materials. *Fire and Materials* 1989; **14**(3):87-96.
36. Delichatsios MA, Panagiotou T, Kiley F. The Use of Time to Ignition Data for Characterizing the Thermal Inertia and the Minimum (Critical) Heat-Flux for Ignition Or Pyrolysis. *Combustion and Flame* 1991; **84**(3-4):323-332.

Table Captions

Table 1 – Base-case polymer model input parameters.

Table 2 – Power-law ($y=Ax^n$) fit parameter n for y =ignition time τ_{ign} or average mass loss rate MLR_{av} , with $x=k, c, \alpha,$ or ΔH_{reac} .

Table 3 – Influence of model input parameters on mass loss rate and ignition time.

Figure Captions

- Figure 1 – Calculated mass loss rate of 25.4 mm thick base-case polymer subjected to incident radiant fluxes of (21, 50, 100, 150, and 200) kW/m². (Inset shows same data with MLR normalized by the steady mass loss rate of Eq. 2, and t normalized by the burning time based on the steady mass loss rate .)
- Figure 2 - Mass loss rate versus time for the base-case polymer at external heat fluxes of a.) 21kW/m² and b.) 100 kW/m² . Different curves on each frame show the effect of thickness of (2, 4, 8, 16, and 32) mm. Dotted line shows the result for 2 mm case with surface absorption.
- Figure 3 – Mass loss rate versus time for the base-case polymer at external heat fluxes of (21and 100) kW/m², frames a.) and b.), respectively, with a value of $E_a=209$ kJ/mol. Different curves on each frame show the effect of $\Delta H_{\text{reac}}=$ (1000, 2000, 3000, 4000, and 5000) kJ kg⁻¹.
- Figure 4 – Mass loss rate versus time for the base-case polymer at external heat fluxes of (21, 50, 100, and 200) kW/m², frames a.) through d.), respectively. Different curves on each frame show the effect of $E_a =$ (97, 209, 418, and 1050) kJ/mol.
- Figure 5 - Mass loss rate versus time for the base-case polymer at external heat fluxes of (21and 100) kW/m², frames a.) and b.), respectively, with a value of $E_a=209$ kJ/mol. Different curves on each frame show the effect of $k =$ (0.1, 0.2, 0.3, 0.4, and 0.5) W m⁻¹ K⁻¹.
- Figure 6 - Mass loss rate versus time for the base-case polymer at external heat fluxes of (21and 100) kW/m², frames a.) and b.), respectively, with a value of $E_a=209$ kJ/mol. Different curves on each frame show the effect of $\alpha =$ (200, 400, 800, 1200, and 50000) m⁻¹.
- Figure 7 - Mass loss rate versus time for the base-case polymer at external heat fluxes of a.) 21kW/m² and b.) 100 kW/m², with $E_a=209$ kJ/mol. Different curves on each frame show the effect of $c =$ (1, 2, 3, 4, and 5) kJ kg⁻¹ K⁻¹ .
- Figure 8 – Ignition time variation for values of the external heat flux of (21, 50, 100, 150, and 200) kW/m², and values of the base-case polymer decomposition activation energy of (97, 209, 518, and 1050) kJ/mol: a.) thermal conductivity, k ; b.) specific heat, c ; c.) absorption coefficient, α ; and d.) heat of reaction, ΔH_{reac} .
- Figure 9 - Ignition time variation for values of the external heat flux of (21, 50, 100, 150, and 200) kW/m², and values of the base-case polymer decomposition activation energy of (97, 209, 518, and 1050) kJ/mol and $\alpha=960$ m⁻¹ a.) and b.) $\alpha=50000$ m⁻¹ .

Table 1– Base-case polymer model input parameters.

Parameter	<u>Units</u>	<u>Nominal Value</u>	<u>Range</u>
<i>Material Bulk Properties:</i>			
Thermal Conductivity	W m ⁻¹ K ⁻¹	0.235	0.1 to 0.5
Specific Heat	kJ kg ⁻¹ K ⁻¹	2.22	1 to 5
Absorption Coefficient	m ⁻¹	960	200 to 50000
<i>Material Decomposition Properties:</i>			
Heat of Reaction	kJ kg ⁻¹	2000	1000 to 5000
Activation Energy	kJ mol ⁻¹	209	97 to 837
Pre-exponential	s ⁻¹	1.29 x 10 ¹⁵	1.02 x 10 ⁶ to 1.25 x 10 ⁶⁶
<i>Experiment Properties:</i>			
Incident Heat Flux	kW m ⁻²	50	21 to 200
Thickness	mm	25.4	2 to 32
<i>Not varied:</i>			
Density	kg m ⁻³	1190	
Ambient Temperature	K	293	
Surface Emissivity		0.95	

Table 2 – Power-law ($y=Ax^n$) fit parameter n for y =ignition time τ_{ign} or average mass loss rate MLR_{av} , with $x=k, c, \alpha$, or ΔH_{reac} .

Parameter:	Power-Law Parameter n							
	ΔH_{reac}		c		α^*		k	
Flux	τ_{ign}	MLR_{av}	τ_{ign}	MLR_{av}	τ_{ign}	MLR_{av}	τ_{ign}	MLR_{av}
21	1.70	-0.72	1.30	-0.32	-0.03	0.016	0.71	-0.005
50	0.140	-0.745	1.00	-0.26	-0.54	-0.079	0.54	-0.004
100	0.046	-0.69	0.91	-0.26	-0.67	-0.12	0.33	-0.010
150	0.044	-0.64	1.00	-0.26	-0.75	-0.14	0.29	-0.009
200	0.020	-0.80	0.97	-0.27	-0.77	-0.12	0.28	-0.010
Expected value								
	0.0	-0.72	1.0	-0.30	n.a.	n.a.	1.0	0.0

* the data range for α was limited to 200 m^{-1} to 1200 m^{-1} to give a good fit.
n.a. not available.

Table 3 – Influence of model input parameters on mass loss rate and ignition time.

<u>Parameter</u>	<u>Mass Loss Rate (MLR)</u>				<u>Ignition Time</u>
	<i>Shape</i>	<i>Average</i>	<i>peak</i>	<i>t_{peak}</i>	
ΔH_{reac}	✓✓	✓✓	✓✓	✓✓	✓ _{LF}
S	✓✓	✓ ^{HF} _{Lα}		✓✓	✓ _{LF}
c	✓	✓	✓ ^{HF}	✓ _{LF}	✓✓
α	✓	✓ ^{HF}		✓ _{LF}	✓ _{not LF}
k	✓			✓ _{LF}	✓
E_a	✓ ^{HF} _{LF}	✓ _{LF}			✓ _{LF}

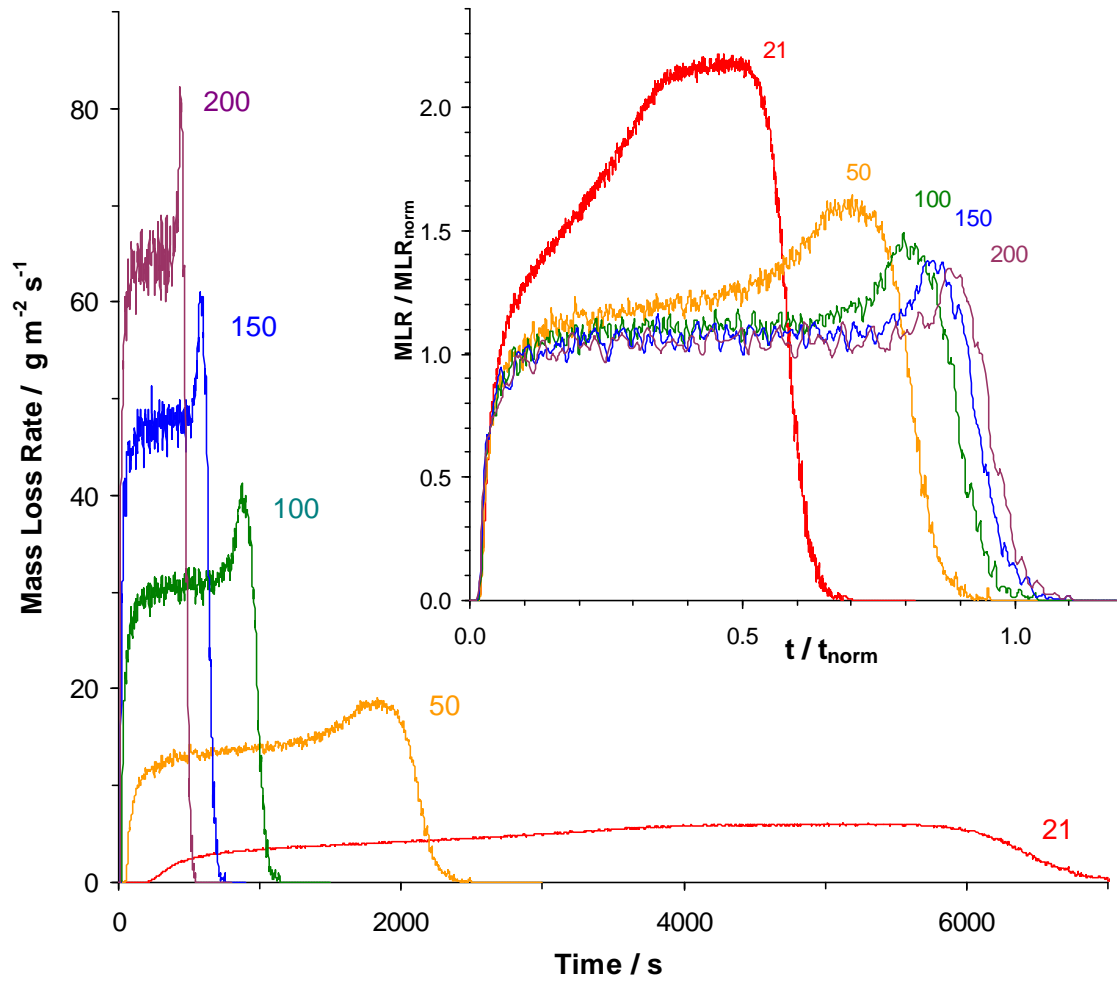


Figure 1 – Calculated mass loss rate of 25.4 mm thick base-case polymer subjected to incident radiant fluxes of (21, 50, 100, 150, and 200) kW/m^2 . (Inset shows same data with MLR normalized by the steady mass loss rate of Eq. 2, and t normalized by the burning time based on the steady mass loss rate .)

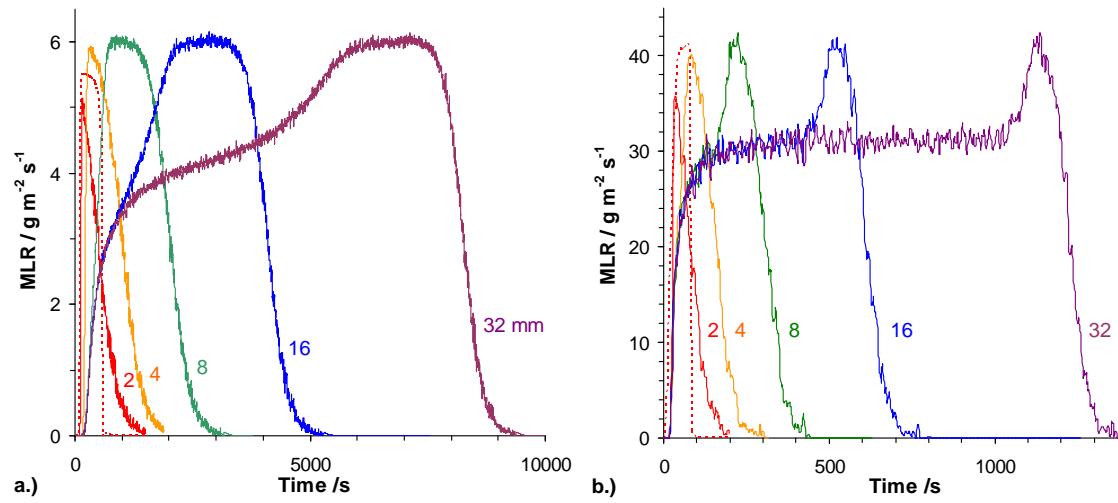


Figure 2 - Mass loss rate versus time for the base-case polymer at external heat fluxes of a.) 21kW/m^2 and b.) 100 kW/m^2 . Different curves on each frame show the effect of thickness of (2, 4, 8, 16, and 32) mm. Dotted line shows the result for 2 mm case with surface absorption.

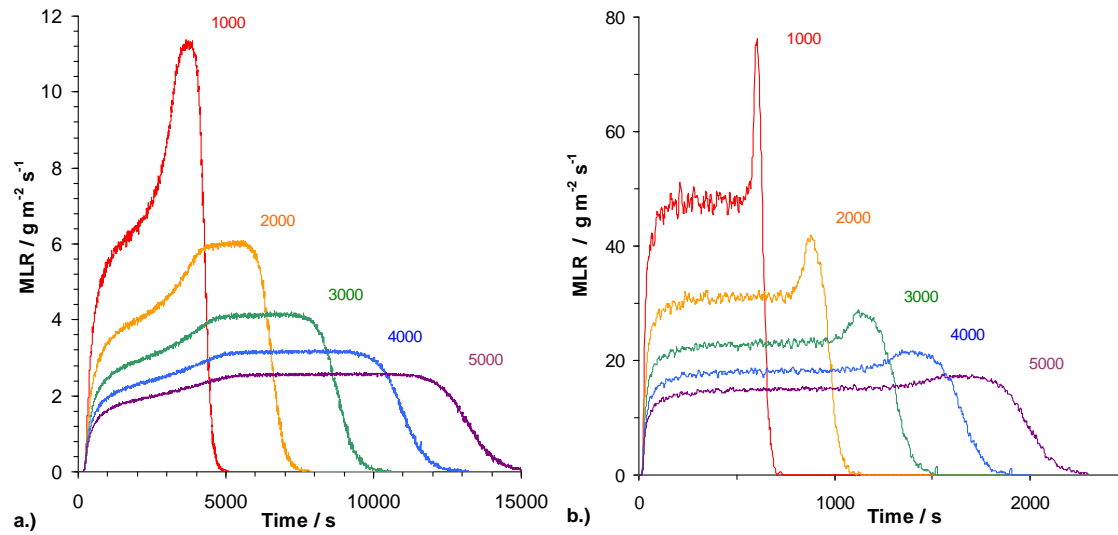


Figure 3 – Mass loss rate versus time for the base-case polymer at external heat fluxes of (21 and 100) kW/m^2 , frames a.) and b.), respectively, with a value of $E_a=209 \text{ kJ/mol}$. Different curves on each frame show the effect of $\Delta H_{\text{reac}}= (1000, 2000, 3000, 4000, \text{ and } 5000) \text{ kJ kg}^{-1}$.

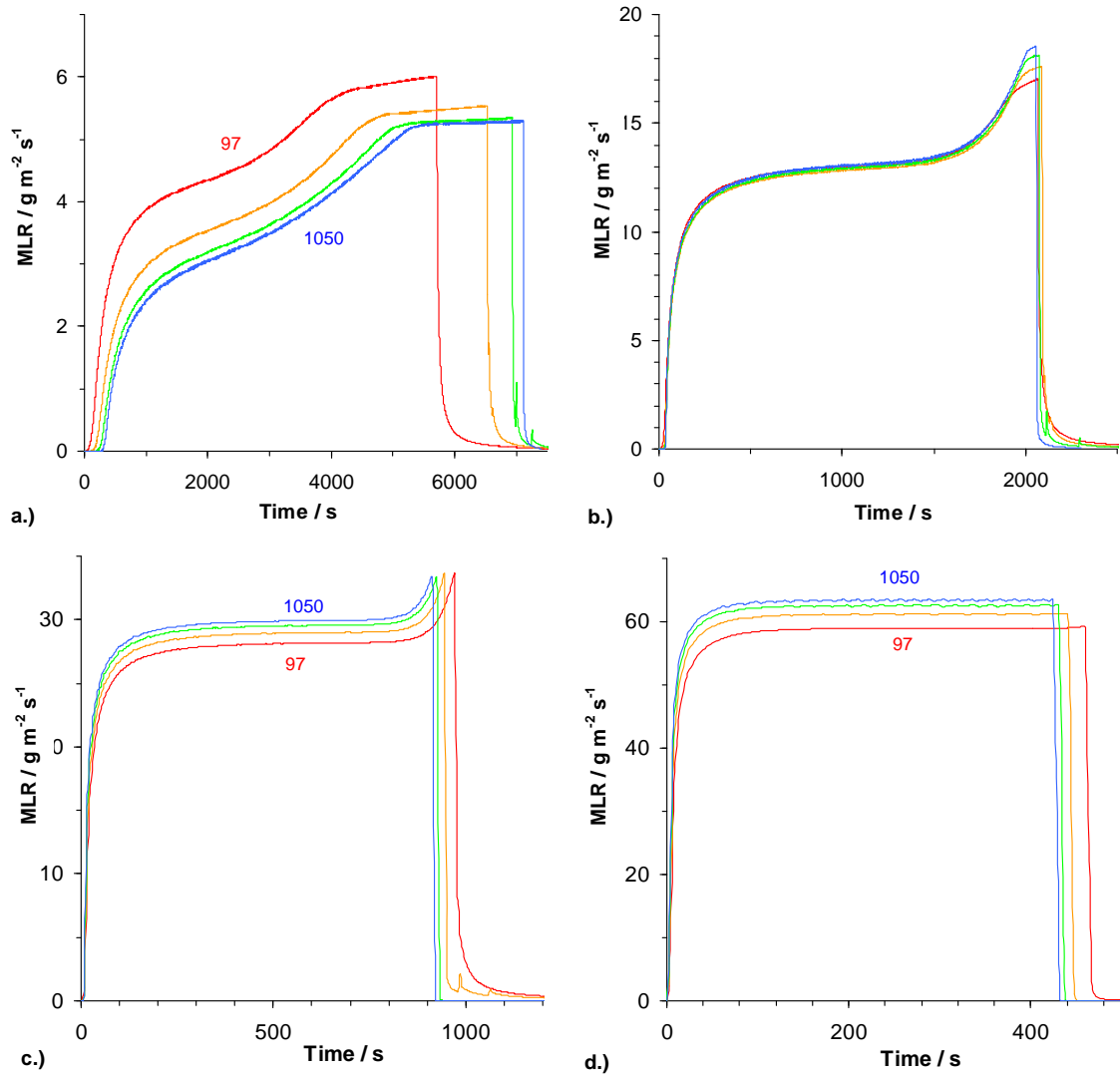


Figure 4 – Mass loss rate versus time for the base-case polymer at external heat fluxes of (21, 50, 100, and 200) kW/m^2 , frames a.) through d.), respectively. Different curves on each frame show the effect of $E_a = (97, 209, 418, \text{ and } 1050) \text{ kJ/mol}$.

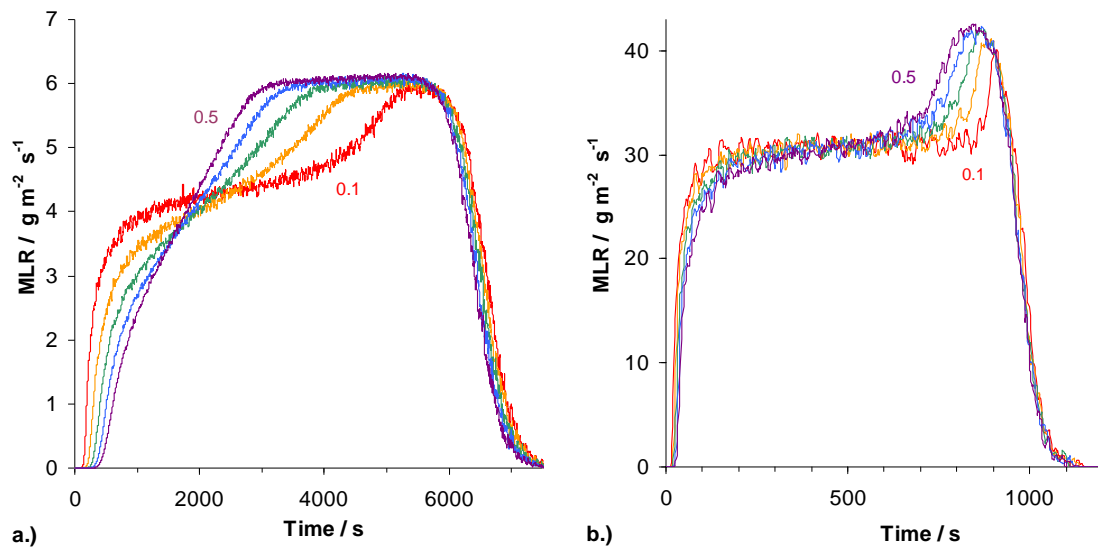


Figure 5 - Mass loss rate versus time for the base-case polymer at external heat fluxes of (21 and 100) kW/m^2 , frames a.) and b.), respectively, with a value of $E_a=209 \text{ kJ/mol}$. Different curves on each frame show the effect of $k = (0.1, 0.2, 0.3, 0.4, \text{ and } 0.5) \text{ W m}^{-1} \text{ K}^{-1}$.

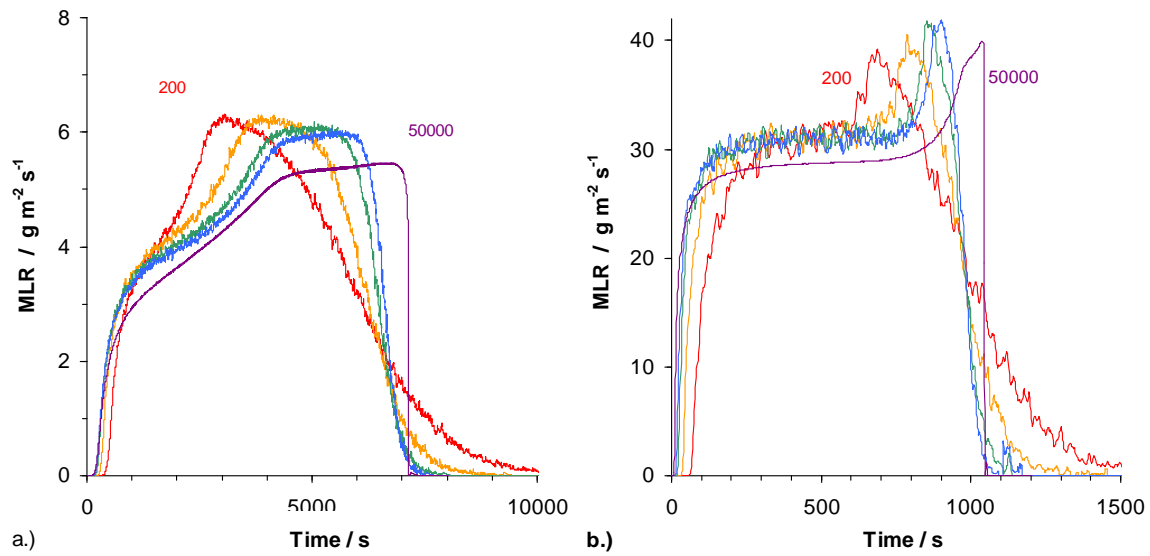


Figure 6 - Mass loss rate versus time for the base-case polymer at external heat fluxes of (21 and 100) kW/m^2 , frames a.) and b.), respectively, with a value of $E_a=209 \text{ kJ/mol}$. Different curves on each frame show the effect of $\alpha = (200, 400, 800, 1200, \text{ and } 50000) \text{ m}^{-1}$.

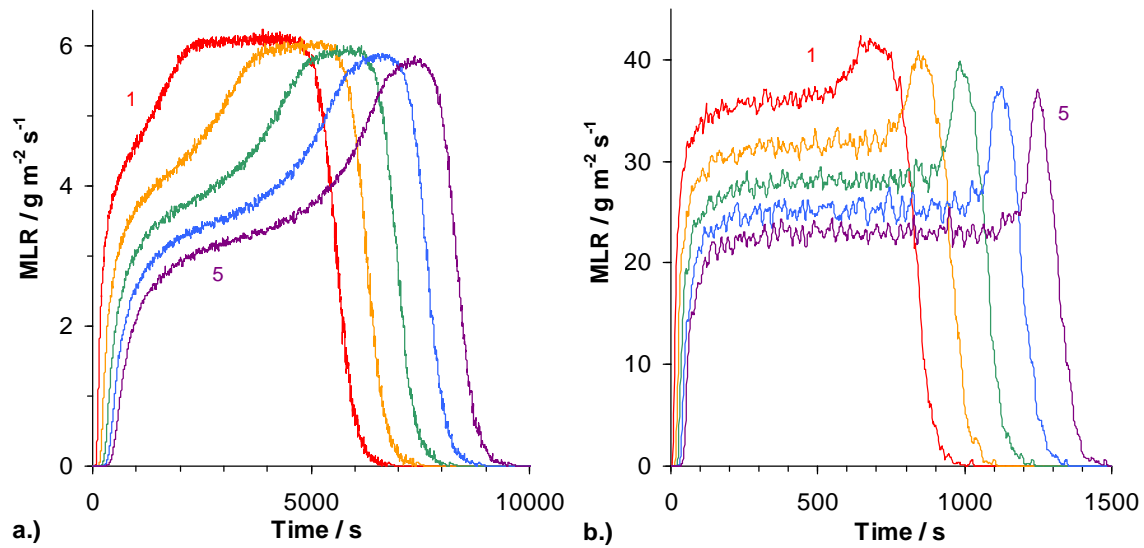


Figure 7 - Mass loss rate versus time for the base-case polymer at external heat fluxes of a.) 21kW/m^2 and b.) 100 kW/m^2 , with $E_a=209\text{ kJ/mol}$. Different curves on each frame show the effect of $c = (1, 2, 3, 4, \text{ and } 5)\text{ kJ kg}^{-1}\text{ K}^{-1}$.

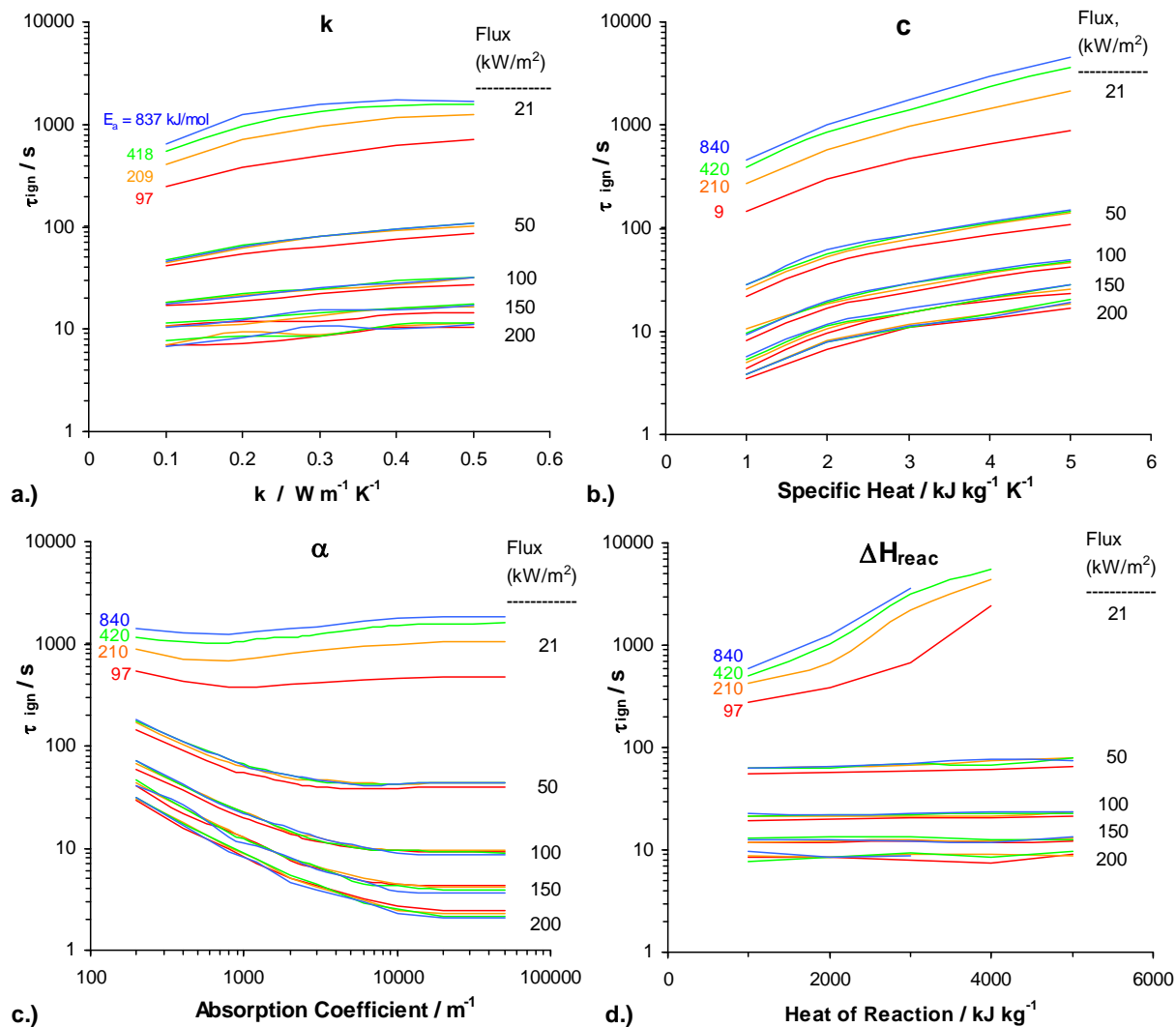


Figure 8 – Ignition time variation for values of the external heat flux of (21, 50, 100, 150, and 200) kW/m^2 , and values of the base-case polymer decomposition activation energy of (97, 209, 518, and 1050) kJ/mol : a.) thermal conductivity, k ; b.) specific heat, c ; c.) absorption coefficient, α ; and d.) heat of reaction, ΔH_{reac} .

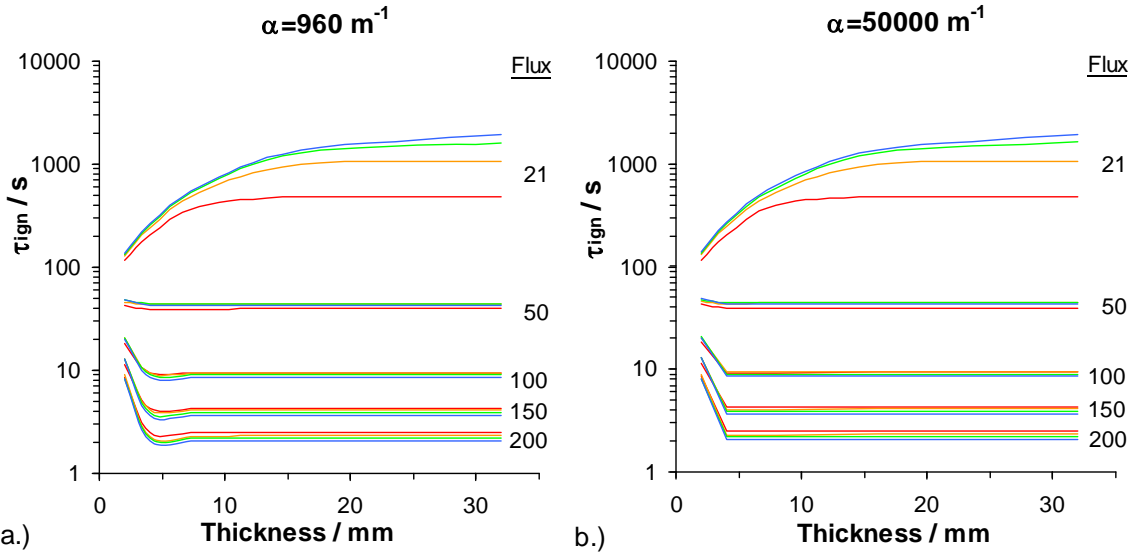


Figure 9 - Ignition time variation for values of the external heat flux of (21, 50, 100, 150, and 200) kW/m², and values of the base-case polymer decomposition activation energy of (97, 209, 518, and 1050) kJ/mol and $\alpha=960$ m⁻¹ a.) and b.) $\alpha=50000$ m⁻¹.